AN ENHANCED AUGMENTED ELECTRIC FIELD INTEGRAL EQUATION AND THE CALCULATION OF CASIMIR FORCE USING COMPUTATIONAL ELECTROMAGNETICS

BY

TIAN XIA

DISSERTATION

Submitted in partial fulfillment of the requirements
for the degree of Doctor of Philosophy in Electrical and Computer Engineering
in the Graduate College of the
University of Illinois at Urbana-Champaign, 2018

Urbana, Illinois

Doctoral Committee:

Professor Weng Cho Chew, Chair
Professor Jianming Jin
Professor Gabriel Popescu
Professor Jose Schutt-Aine

Abstract

In this dissertation, a surface integral equation formulation is developed for low-frequency problems by generalizing the existing augmented electric field integral equation from the perfect electric conductors to the dielectrics and general conductors. Detailed discussions of the basis functions and the preconditioner are provided for the dielectric problems, and a novel integration scheme for the evaluations of the matrix elements in the conductor problem is proposed.

Then a broadband multilevel fast multipole algorithm (FMA) using a hybridization of the multipole and plane wave expansions is introduced. This high-accuracy algorithm is error controllable and stable at low frequencies. It reduces to the conventional diagonal FMA at higher frequencies. Therefore it can be regarded as a generalization of the dense FMA at low frequencies and the diagonal FMA at higher frequencies.

Finally, the computational electromagnetic techniques are applied to the calculations of the Casimir force. The application of the integral equation method in Casimir force calculation is briefly reviewed and we proposed an efficient computing scheme using the randomized singular value decomposition and the hybrid FMA. As a result, the efficiency can be greatly enhanced for large problems.

To my parents and Haini.

Acknowledgments

When I took off the bus at the campus of the University of Illinois Urbana-Champaign in the winter of 2011, it snowed. I still remembered the last time I saw such snows was when I was ten with my parents in my hometown. My parents have given all their love to me and provided me the best they had. As the only child in the family, I feel deeply indebted to them. My beloved fiancée Haini has always been my best mate, sharing my happiness, encouraging and helping me whenever and whereever. Without their love and support, I would not be able to finish this thesis.

When I first started graduate study, I felt ignorant when attending the group literature review seminars and struggled to prepare my own seminars. Persistently encouraged by Professor Chew to learn broadly and think deeply, I started to build up more solid electromagnetic knowledge, learn quantum mechanics, construct physical intuitions and continue mathematical practices and numerical algorithm study. Thanks to Professor Chew's patient guidance and the teamwork of the colleagues, we delivered a new algorithm in the Intel-Semiconductor Research Corporation (SRC) project. This experience offered the best training to develop numerical algorithms and revealed the unimagined fun in learning engineering. "Do not dabble in the math, read the physics from it," said Professor Chew. I learned the beauty of the connections between mathematics and physics by further studying them in my research problems. For the guidance in my research work, encouragement to keep searching for the truth, sharing deep insights in physics, and educating me to be a self-motivated researcher, as he always demonstrated, I will always be grateful to Professor Weng Cho Chew.

I am very grateful to the professors in the department for their excellent courses and guidance. I would like to thank Professor Jianming Jin for the fruitful electromagnetic courses. I would like to thank Professor Jose Schutt-Aine for his excellent microwave engineering lab and the signal integrity

course. I would like to thank Professor Gabriel Popescu and Professor Scott Carney for their interesting optics courses. I would like to thank Professor Pramod Viswanath for teaching me the beautiful mathematics in his information theory course. I would like to thank Professor Erhan Kudeki for teaching me remote sensing in the most passionate way. I would like to thank Professor John Stack and Professor Michael Stone in the department of Physics for the excellent courses in quantum mechanics and mathematical physics. I would like to express my special appreciation to Professor Jianming Jin, Professor Gabriel Popescu and Professor Jose Schutt-Aine for serving as my doctoral committee and offering valuable suggestions.

My colleagues and friends have been very helpful in many aspects. I would like to thank Dr. Phillip Atkins, Shu Chen, Dr. Qi Dai, Hui Gan, Aiyin Liu, Dr. Qin Liu, Dr. Zuhui Ma, Lingling Meng, Thomas Roth, Dr. Joe Rutherford, Dr. Carlos Salazar-Lazaro, Palash Sarker, Aditya Sarathy, Mike Wei, Dr. Yumao Wu and Dr. Xiaoyan Xiong for sharing their brilliant ideas and for their friendship.

I also would like to thank Dr. Alaeddin Aydiner, Dr. Kemal Aygün, Dr. Henning Braunisch and Dr. Zhiguo Qian for mentoring us in the Intel-SRC project. I would like to thank Dr. Rickard Petersson and Dr. Kezhong Zhao for offering me the internship at ANSYS, Inc. I would like to thank Dr. Lijun Jiang for offering me the summer research opportunities at the University of Hong Kong.

Table of Contents

Chapter 1

Introduction

1.1 Computational Electromagnetics

Solving Maxwell's equations with computer programs has rapidly developed, due to boosted developments of computer hardware. This subject is termed "computational electromagnetics" (CEM) and CEM tools have found a large number of applications in engineering designs and academic research. These applications include studies of the electromagnetic (EM) wave propagation in large environments, such as in the earth's atmosphere or even toward the universe. The EM phenomena in tiny structures, such as EM waves in photonic crystals and integrated circuits, is also in the scope of CEM. The wide range of applications of CEM is largely due to the rich physics of the Maxwell equations at different scales. At large length scales, when the wavelength is much smaller than the objects of interest, Maxwell's equations reveal the ray physics. At medium length scales, when the wavelength is comparable to the objects, wave physics dominates. At small length scales, when the wavelength is much larger, circuit physics becomes important. The physics of Maxwell's equations is so rich and the applications of the electromagnetics are so wide that solving Maxwell's equations has become an important topic of research.

Maxwell's equations can be approximated by Kirchhoff's laws at small length scales and it can be reduced to the lens maker's formula at large length scales. Some problems can be solved analytically with approximations. At medium length scales, when wave physics becomes rich, Maxwell's equations can only be solved for limited special boundary conditions. Solving them using numerical methods will be a good alternative.

In CEM, many methods are developed to solve Maxwell's equations numerically. They can be categorized into two classes: the time domain meth-

ods and the frequency domain methods. In the time domain methods, the most popular and earliest developed method is the finite difference time domain (FDTD) method [1]. Recently the time domain finite element (TDFE) and time domain integral equation (TDIE) methods have become interesting research areas. These methods have their counterparts in the frequency domain: the finite difference frequency domain (FDFD) method, the finite element method (FEM) [2] and the method of moments (MoM) [3] or the integral equation (IE) method. These methods have their own advantages and disadvantages. A good understanding and the applications of these methods will be beneficial in efficiently solving EM problems.

1.2 Surface Integral Equation and Fast Multipole Algorithm

There are two popular kinds of integral equations: the volume integral equation (VIE) and the surface integral equation (SIE). The volume of the structure is discretized into small volumetric simplexes in VIE and the simplexes are mutually coupled through the Green's function. Therefore, this method can be easily adopted to treat inhomogeneous media. In the SIE, only the surface is discretized and the coupling is through the same Green's function as the VIE. Since the unknowns only reside on the surface of the structure in this method, the computational cost is greatly reduced. The limitation of this method is that it is only capable of simulating homogeneous objects.

Due to the fast algorithm used in the VIE and SIE, integral equation methods have become very popular in solving EM problems, such as scattering problems, circuit interconnect and packaging problems, etc. The radar cross section (RCS) or the scattering cross section (SCS), and the near field can be efficiently simulated in the scattering problems. The linear circuit equivalent parameters, such as the S parameters, can also be efficiently found. In this method, the EM problem is converted into a matrix equation:

$$\overline{\mathbf{A}} \cdot \mathbf{I} = \mathbf{V} \tag{1.1}$$

where $\overline{\mathbf{A}}$ is called the system matrix, $\mathbf{I}$ is the surface unknown vector to be solved and $\mathbf{V}$ is the excitation vector. The matrix $\overline{\mathbf{A}}$ can be constructed

using the subspace projection method by projecting the unknown into a linear summation of the basis functions and then testing the integral equation using the dual basis functions. The most popular basis function is the Rao-Wilton-Glisson (RWG) basis function [4], since it is simple and divergence-conforming, which is required by the physical properties of the current unknown. Other more complicated but useful divergence-conforming basis functions, the Wilton-Chen basis function [5] and the Buffa-Christiansen (BC) basis function [6], served as the dual basis function for testing. Other basis functions, such as the loop-tree basis function [7, 8] were also studied to eliminate the low-frequency breakdown issues.

The construction of the matrix $\overline{\mathbf{A}}$ also depends on the integral equation. A few integral equation formulations can be found. The simplest formulation is the electric field integral equation (EFIE) and the magnetic field integral equation (MFIE). These formulations suffer from internal resonance issues at high frequencies. A combined formulation, called the combined field integral equation (CFIE) [9] was proposed to overcome the problems. The formulations, such as Poggio-Miller-Chang-Harrington-Wu-Tsai (PMCHWT) [10, 11] and Müller's formulations [12] are the alternatives to CFIE. At low frequencies, the internal resonance is no longer a problem, but EFIE suffers from the low-frequency breakdown. It has been extensively studied to eliminate this problem [13, 14] for the perfect electric conductor (PEC). In this dissertation, a formulation is proposed to overcome this problem for the dielectrics and general conductors with finite conductivities.

To solve the equation in (1.1), a direct solver is possible if the matrix size is small. As the size of the matrix becomes larger, the iterative solver will become more efficient to reduce the computational cost from $O(N^3)$ to $O(N^2)$. In an iterative solver, only the matrix vector product (MVP) of $\overline{\mathbf{A}} \cdot \mathbf{I}$ is required for a number of times. As the matrix size becomes even larger, filling and storing the matrix $\overline{\mathbf{A}}$ become too time and memory consuming. A compressed storage of $\overline{\mathbf{A}}$ using the fast multipole algorithm (FMA) can be used to accelerate the MVP from $O(N^2)$ to $O(N \log N)$ or $O(N)$ and save the memory storage from $O(N^2)$ to $O(N)$. Therefore, FMA becomes widely used to accelerate MVP in the integral equations.

The FMA is used to accelerate $\overline{\mathbf{A}} \cdot \mathbf{I}$. The physical interpretation of $\overline{\mathbf{A}} \cdot \mathbf{I}$ is the summation of the field radiated by the source at location i with the current amplitude I_i, where i refers to the index of the source. The key reason

that the FMA can be used to accelerate the MVP is because the sources can be grouped to become a new source. Then the far field pattern can be represented by the radiation of the new source. This new source can be, either represented as a summation of a few multipoles at one location, or represented as a summation of plane waves in all directions. These two approaches are termed the multipole expansion or the plane wave expansion. Still there are some limitations in these expansions. The multipole expansion becomes inefficient at high frequencies since the grouping is through a dense matrix and the matrix size becomes increasingly large. The plane wave expansion fails to capture the evanescent waves and it is unstable at low frequencies. A broadband FMA will be extremely useful in the simulations of the multi-scale problems using integral equation. In this dissertation, we will introduce a hybridization of the multipole and plane wave expansions for broadband simulation using FMA.

1.3 Casimir Force Calculations Using Surface Integral Equation

The Casimir force has become an interesting research topic since the highly accurate experimental validations [15, 16]. This tiny force, which arises from the zero point energy of the vacuum, can be potentially useful in the applications of the microelectromechanical systems (MEMS). As a result, it has strongly motivated the theoretical studies of the Casimir force using different approaches.

The first introduction of the Casimir force by Casimir in 1948 [17] suggested that the force is due to the change of zero-point energy in the vacuum. In this approach, calculations of the free-space modes energy are required. Although the total energy is divergent, it can be correctly regulated. A similar approach is to use the scattering matrices to solve this problem [18]. The argument principle method [19] and the path integral method [20] can be used to arrive at the same expression of the Casimir force.

A more general approach was proposed by Liftshitz [21] to calculate the Casimir force between dielectric objects at finite temperature. This approach is based on the fluctuation-dissipation theorem [22, 23] and uses the Maxwell stress tensor to calculate the force.

Both of the above two approaches utilize the Green's function of the environment. Therefore, the computational techniques in the integral equation can be applied in the calculations of the Casimir force. For example, using the argument principle, the Casimir force is directly related to the impedance matrix in the SIE. We will follow this relation, and propose a fast computing scheme.

1.4 An Overview of the Dissertation

Several aspects of the integral equation method in computational electromagnetics and physics are studied in this dissertation.

In Chapter 2, a low-frequency stable SIE method for dielectrics, termed enhanced augmented electric field integral equation (E-AEFIE), is presented. Motivated by the AEFIE formulation for the perfect electric conductor (PEC), the internal and external problems are both augmented with the current continuity equation and re-normalized to eliminate the low-frequency breakdown. A few aspects of this method are studied.

In Chapter 3, E-AEFIE is generalized to conductor problems. The conductive region is simulated as a lossy dispersive medium using a full wave solver. We investigate the evaluations of the integrals of Green's function in lossy media. After comparisons with some other integration methods, we propose a new method to evaluate such integrals. This method turns out to improve the accuracy and efficiency. Moreover, the proposed formulation can be regarded as a generalized impedance boundary condition. It is then used to solve numerical examples of complex circuit structures to demonstrate the accuracy and its capabilities.

In Chapter 4, we propose a broadband multilevel fast multiple algorithm (MLFMA) using a hybridization of the plane wave and the multipole expansions of the Green's function in the analysis of three-dimensional multi-scale electromagnetic problems. The diagonal plane wave expansion is used for low-order harmonics, which captures most of the propagating spectrums, while the dense multipole expansion is used for high-order harmonics, which captures most of the evanescent spectrums. By analyzing the errors and accordingly choosing the numbers of harmonics, the method is free of the low-frequency breakdown and remains accurate at arbitrary low frequencies.

Meanwhile, the method reduces to the conventional diagonal FMA as the frequency increases. Therefore, it can be regarded as the generalization of the conventional dense and diagonal FMAs. Numerical studies in this chapter show that very high accuracies can be achieved using the method.

In Chapter 5, we review the calculations of the Casimir force using the SIE. The Casimir force between two objects is expressed in term of the trace of a matrix, which is directly related to the matrices in the SIE. The Casimir force equation is derived using the argument principle and a fast calculation scheme is proposed using the randomized singular value decompositions. Since this scheme relies on fast computations of the MVP in the SIE, we generalize the hybrid FMA in Chapter 4 to the imaginary frequencies. As a result, a complexity of $O(N)$ can be achieved in this fast scheme. Finally, we validate the method and demonstrate the accuracy of the fast scheme with some numerical examples.

We finally draw the conclusions in Chapter 6 and propose some possible future work.

Chapter 2

An Enhanced Augmented Electric Field Integral Equation for Dielectric Objects

2.1 Introduction

Among many of the numerical approaches to solve electromagnetic (EM) problems, the surface integral equation (SIE) method is an efficient one. The time domain methods, such as the finite different time domain (FDTD) [1] and the finite element time domain (FETD) [2] methods, require discretization of the volume and time marching, which are usually numerically expensive. The finite element method (FEM) and the volume integral equation (VIE) method [3] can also be used to solve EM problems accurately in the frequency domain. However, they require uniform volumetric meshes, which are more difficult to generate than the surface meshes, especially for complicated and multi-scale structures. Meanwhile, the number of unknowns increases dramatically for volume problems compared to surface problems. The SIE method is based on the surface meshes. Therefore, the number of unknowns is manageable even for very large problems. Although the resultant system matrices are dense since the matrix elements are related to the Green's function, fast algorithms to accelerate the matrix vector product can be adopted to reduce the computational costs in iterative solvers.

In many circuit applications, low-frequency (long wavelength) stable EM solvers are urgently required for both perfect electric conductor (PEC) and dielectric structures. However, there is a well-known low-frequency breakdown problem for SIE and FEM. Much effort has been made to tackle this problem. For SIE, the loop-tree decomposition [7, 8, 24] was proposed to perform the quasi Helmheltz decomposition. Hence, after proper normalizations [24], the solenoidal and irrotational currents can be accurately solved at low frequencies. Similar methodology, namely the tree-cotree splitting [25], was applied to the finite element method (FEM). These two methods

introduce basis functions that conform with the properties of the fields or the equivalent currents. Then the representations of the currents and fields become more precise. However, searching for the corresponding loop-tree basis functions can be very expensive, especially for complicated structures with multiple connections.

The augmented electric integral equation (A-EFIE), obtained by augmenting the EFIE with the current continuity equation, offers an elegant way to re-normalize the EFIE without the need for loop-tree decomposition. As a result, it eliminates the low-frequency breakdown [14, 26] without increasing the computational cost since the additional cost arise from matrices of high sparsity. Although there exists an inaccuracy issue with A-EFIE for capacitive and scattering problems at extremely low frequencies, the enhanced A-EFIE with the perturbation method serves as the remedy [27, 28].

As for the dielectrics, there are some well-established and widely used formulations suitable for problems at mid frequencies, such as the combined field integral equations (CFIE) [9], Poggio-Miller-Chang-Harrington-Wu-Tsai (PMCHWT) [10, 11] and Müller's formulations [12]. These formulations are the weighted summations of electric field integral equations (EFIE) and magnetic field integral equations (MFIE) for the internal and external regions. These formulations avoid the internal resonance problem by effectively shifting the internal resonance frequency to a complex number. For low-frequency applications, since the wavelength is usually much larger than the structure size, the internal resonance phenomenon is absent. Therefore, there is no need to apply the summations of EFIE and MFIE for low-frequency dielectric problems. Instead, only the EFIE or MFIE is required. To avoid the introduction of the magnetic field excitations and fictitious magnetic charges, the augmentation technique is applied to EFIE.

A previous work [29] introduces both current and charge in the EFIE and MFIE and formulates a frequency stable integral equation for conductive and dielectric objects. In this formulation, the hyper-singular integral operator can be re-balanced by normalizations by the introduction of charges. It has been demonstrated that this formulation is stable down to the static limit. However, it introduces the magnetic charges and the magnetic field excitations are required, while the A-EFIE formulation does not require MFIE.

In this chapter, the A-EFIE formulations are applied to the dielectric objects in the internal and external regions. The original unknown surface elec-

tric current is converted to two sets of unknowns: the electric current and charge. After proper re-normalizations, a better conditioned matrix system can be formed. To further reduce the condition number and better represent the electric and magnetic currents, the Chen-Wilton [5, 30] or a similar alternative Buffa-Christiansen (BC) basis function [6, 31] can be introduced. In this chapter the BC basis function is chosen as it is widely accepted and used in the EM community. Using this basis function to expand the magnetic current, the system matrix becomes well-conditioned. For problems with a large number of unknowns, the mixed-form fast multipole algorithm (FMA) [32] together with the pre-conditioner is integrated with this formulation for accelerated computations.

This chapter is organized as such: Section 2.2 summarizes the existing formulations of A-EFIE for PEC. Section 2.3 introduces the new A-EFIE formulation for dielectric objects. The choices of the testing and basis functions are discussed. Meanwhile, to accelerate the computations, the integrations of the mixed-form FMA and the pre-conditioner are briefly introduced. This A-EFIE solver for dielectrics is further validated with numerical results in Section 2.4. The improvement of the condition numbers and the convergence are also presented.

2.2 A-EFIE Formulation for PEC

In this section, the A-EFIE formulation for PEC is reviewed. This work has been extensively studied in [14, 26] and its treatment is similar to [29] except that MFIE is not required. For PEC structures, only the external problem needs to be solved by invoking the extinction theorem [33]. To solve the external electric field integral equation (EFIE) with low-frequency stability, the augmentation technique is adopted. By adding the current continuity equation into the formulation, we can re-normalize the equations to overcome the low-frequency breakdown.

2.2.1 Motivations of A-EFIE

The EFIE formulation is widely used for PEC problems. It, however, breaks down for low-frequency problems. The reason is due to the imbalance in the

two operators in the EFIE equation:

$$i\omega\mu\left(\int_{S'} d\mathbf{r}' g(\mathbf{r},\mathbf{r}') + \int_{S'} d\mathbf{r}' \frac{\nabla\nabla}{k^2} g(\mathbf{r},\mathbf{r}')\right)\cdot\mathbf{J}(\mathbf{r}') = -\mathbf{E}_{inc}(\mathbf{r}) \tag{2.1}$$

The ratio of the frequency scalings in the first and second operators in (2.1) is $O((kL)^2)$, where L is the effective length of the object. For low-frequency (electrically small) problems, $kL \to 0$, the two operators are poorly balanced. It is to be noted that there is a large null space of the divergence-free current in the second operator. Since

$$\int_{S'} d\mathbf{r}' \nabla\nabla g(\mathbf{r},\mathbf{r}')\cdot\mathbf{J}(\mathbf{r}') = \int_{S'} d\mathbf{r}' \nabla g(\mathbf{r},\mathbf{r}')\nabla'\cdot\mathbf{J}(\mathbf{r}') \tag{2.2}$$

For small k, the second term (2.1) swamps the first term due to the computational precision. Therefore the vector potential contribution in the first term of (2.1) are not well captured. Also due to that the second term dominates and the null space of the divergence operator in it, the problem becomes very difficult to solve. A-EFIE serves as a remedy for this by introducing the current continuity equation into the formulation. Then a re-balance of the two operators can be achieved.

2.2.2 A-EFIE Formulation for PEC

By introducing the current continuity equation and re-balancing the two operators in (2.1), we have:

$$\mu_r \int_{S'} d\mathbf{r}' g(\mathbf{r},\mathbf{r}')\cdot\tilde{\mathbf{J}}(\mathbf{r}) + \epsilon^{-1}\int_{S'} d\mathbf{r}' \nabla g(\mathbf{r},\mathbf{r}')\tilde{\rho}(\mathbf{r}') = -\frac{\mathbf{E}_{inc}}{\eta_0} \tag{2.3}$$

and the normalized current continuity equation is:

$$\nabla'\cdot\tilde{\mathbf{J}}(\mathbf{r}') + k_0^2\tilde{\rho}(\mathbf{r}') = 0 \tag{2.4}$$

where the current and charge are normalized as $\tilde{\mathbf{J}} = ik_0\mathbf{J}$ and $\tilde{\rho} = c_0\rho$. This treatment is equivalent to introducing the normal electric field component as the unknown [29]. Note that the frequency scalings of the two operators in (2.3) are $O(1)$ while the unknowns are normalized with the frequency. Using

the standard Galerkin's method, (2.3) and (2.4) can be discretized as:

$$\begin{bmatrix} \overline{\mathbf{V}} & \overline{\mathbf{D}}^T \cdot \overline{\mathbf{P}} \\ \overline{\mathbf{D}} & k_0^2 \bar{\mathbf{I}} \end{bmatrix} \cdot \begin{bmatrix} \tilde{\mathbf{J}} \\ \tilde{\boldsymbol{\rho}} \end{bmatrix} = \begin{bmatrix} -\eta_0^{-1}\mathbf{b} \\ 0 \end{bmatrix} \tag{2.5}$$

where $\overline{\mathbf{D}}$ is the matrix form of divergence operator, and $\bar{\mathbf{I}}$ is the identity matrix. The other matrix elements are defined as:

$$\left[\overline{\mathbf{V}}\right]_{mn} = \mu_r \int_S d\mathbf{r} \boldsymbol{\Lambda}_m(\mathbf{r}) \cdot \int_{S'} d\mathbf{r}' g(\mathbf{r}, \mathbf{r}') \boldsymbol{\Lambda}_n(\mathbf{r}') \tag{2.6}$$

$$\left[\overline{\mathbf{P}}\right]_{mn} = \epsilon_r^{-1} \int_S d\mathbf{r} h_m(\mathbf{r}) \int_{S'} d\mathbf{r}' g(\mathbf{r}, \mathbf{r}') h_n(\mathbf{r}') \tag{2.7}$$

$$\mathbf{b}_m = \int_S d\mathbf{r} \boldsymbol{\Lambda}_m(\mathbf{r}) \cdot \mathbf{E}_{inc}(\mathbf{r}) \tag{2.8}$$

where $\boldsymbol{\Lambda}$ is the normalized RWG basis function and h is the pulse basis function.

2.2.3 A-EFIE and EFIE

Since A-EFIE is based on EFIE, A-EFIE can be reduced to EFIE in the matrix form. Using the factorization and inversion of a 2×2 block matrix:

$$\begin{bmatrix} \overline{\mathbf{A}} & \overline{\mathbf{U}} \\ \overline{\mathbf{V}} & \overline{\mathbf{D}} \end{bmatrix}^{-1} = \begin{bmatrix} \bar{\mathbf{I}} & \overline{\mathbf{0}} \\ -\overline{\mathbf{D}}^{-1}\overline{\mathbf{V}} & \bar{\mathbf{I}} \end{bmatrix} \cdot \begin{bmatrix} \overline{\mathbf{B}}^{-1} & \overline{\mathbf{0}} \\ \overline{\mathbf{0}} & \overline{\mathbf{D}}^{-1} \end{bmatrix} \cdot \begin{bmatrix} \bar{\mathbf{I}} & -\overline{\mathbf{U}\mathbf{D}}^{-1} \\ \overline{\mathbf{0}} & \bar{\mathbf{I}} \end{bmatrix} \tag{2.9}$$

where B is the Schur complement matrix defined as:

$$\overline{\mathbf{B}} = \overline{\mathbf{A}} - \overline{\mathbf{U}\mathbf{D}}^{-1}\overline{\mathbf{V}} \tag{2.10}$$

The inverse of the A-EFIE matrix can then be written as:

$$\begin{aligned} \begin{bmatrix} \overline{\mathbf{V}} & \overline{\mathbf{D}}^T \cdot \overline{\mathbf{P}} \\ \overline{\mathbf{D}} & k_0^2 \bar{\mathbf{I}} \end{bmatrix}^{-1} = & \begin{bmatrix} \bar{\mathbf{I}} & \overline{\mathbf{0}} \\ -\frac{1}{k_0^2}\overline{\mathbf{D}} & \bar{\mathbf{I}} \end{bmatrix} \cdot \\ & \begin{bmatrix} \left(\overline{\mathbf{V}} - \frac{1}{k_0^2}\overline{\mathbf{D}}^T \cdot \overline{\mathbf{P}} \cdot \overline{\mathbf{D}}\right)^{-1} & \overline{\mathbf{0}} \\ \overline{\mathbf{0}} & \frac{1}{k_0^2}\bar{\mathbf{I}} \end{bmatrix} \cdot \begin{bmatrix} \bar{\mathbf{I}} & -\frac{1}{k_0^2}\overline{\mathbf{D}}^T\overline{\mathbf{P}} \\ \overline{\mathbf{0}} & \bar{\mathbf{I}} \end{bmatrix} \end{aligned} \tag{2.11}$$

Applying this inverse to (2.5), we find:

$$ik_0\mathbf{J} = \left(\overline{\mathbf{V}} - \frac{1}{k_0^2}\overline{\mathbf{D}}^T \cdot \overline{\mathbf{P}} \cdot \overline{\mathbf{D}}\right)^{-1} \cdot (-\eta_0^{-1}\mathbf{b}) \tag{2.12}$$

$$c_0\boldsymbol{\rho} = \frac{i}{k_0}\overline{\mathbf{D}} \cdot ik_0\mathbf{J} \tag{2.13}$$

where (2.12) is equivalent to EFIE and (2.13) is equivalent to the current continuity equation. Therefore, solving A-EFIE can be reduced to finding $\mathbf{J}$ from EFIE and then using (2.13) to find $\boldsymbol{\rho}$.

A further step to avoid the rank deficiency of the matrix in (2.5) at the static limit is to apply the charge neutrality. In electro-static case, distribution of charges on PEC surface produces zero field inside the PEC given that there are no external excitations. This will give rise to a null space of the matrix (2.5) when $k_0 \to 0$. By assuming that the structure is neutral, i.e. $\sum_i \rho_i = 0$, this null space can be removed. More mathematical discussion of this issue can be found in [26]. Therefore, a reduced charge formulation can be written as:

$$\begin{bmatrix} \overline{\mathbf{V}} & \overline{\mathbf{D}}^T \cdot \overline{\mathbf{P}} \cdot \overline{\mathbf{B}} \\ \overline{\mathbf{F}} \cdot \overline{\mathbf{D}} & k_0^2\overline{\mathbf{I}} \end{bmatrix} \cdot \begin{bmatrix} \tilde{\mathbf{J}} \\ \tilde{\boldsymbol{\rho}}_r \end{bmatrix} = \begin{bmatrix} -\eta_0^{-1}\mathbf{b} \\ 0 \end{bmatrix} \tag{2.14}$$

where $\tilde{\boldsymbol{\rho}}_r$ has one element less than $\tilde{\boldsymbol{\rho}}$. Matrices $\overline{\mathbf{B}}$ and $\overline{\mathbf{F}}$ are used for charge neutrality constraints.

2.3 A-EFIE Formulation for Dielectrics

The A-EFIE formulation can be extended to dielectrics. When the object becomes penetrable, both the internal and external problems need to be solved. In this section, the equations for the two regions can be formulated with the extinction theorem. Then the augmentation technique can be applied to the $\mathcal{L}$ operator to eliminate the low-frequency breakdown. The $\mathcal{K}$ matrix,[1] however, is ill-conditioned if the divergence conforming RWG basis function is used as the testing and basis function. The choice of the testing and basis functions for $\mathcal{K}$ is discussed to produce a well-conditioned matrix.

[1] We will use matrix to mean the matrix form or representation of an operator.

A preconditioner is also presented here.

2.3.1 A-EFIE Formulation for Dielectrics

By introducing the equivalent magnetic current on the surface, the two EFIEs are:

$$\mathcal{L}_{ext}(\mathbf{r},\mathbf{r}')\cdot\mathbf{J}(\mathbf{r}')+\mathcal{K}_{ext}(\mathbf{r},\mathbf{r}')\cdot\mathbf{M}(\mathbf{r}')-\frac{1}{2}\hat{n}\times\mathbf{M}(\mathbf{r})=-\mathbf{E}_{inc}(\mathbf{r}) \quad (2.15)$$

$$\mathcal{L}_{int}(\mathbf{r},\mathbf{r}')\cdot\mathbf{J}(\mathbf{r}')+\mathcal{K}_{int}(\mathbf{r},\mathbf{r}')\cdot\mathbf{M}(\mathbf{r}')+\frac{1}{2}\hat{n}\times\mathbf{M}(\mathbf{r})=0 \quad (2.16)$$

where the subscripts "*ext*" and "*int*" refer to the external and internal operators with the corresponding Green's function. The expression of $\mathcal{K}$ operator is the principal value integral:

$$\mathcal{K}(\mathbf{r},\mathbf{r}')\cdot\mathbf{M}(\mathbf{r}')=\oint_{S'}d\mathbf{r}'\nabla' g(\mathbf{r},\mathbf{r}')\times\mathbf{M}(\mathbf{r}') \quad (2.17)$$

where the first term is the residue term and the second is the principal value integral term. The signs of the $\hat{n}\times I$ terms differ in (2.15) and (2.16) due to different signs of residual values for the external and internal regions problems. Expanding the electric and magnetic currents $\mathbf{J}$ and $\mathbf{M}$ with basis functions $\mathbf{\Lambda}^J$ and $\mathbf{\Lambda}^M$, testing the equations with $\mathbf{T}$ and applying the augmentation technique with the reduced unknowns $\boldsymbol{\rho}_r$, we arrive at the matrix equation:

$$\begin{bmatrix}\overline{\mathbf{V}}_{ext} & -\frac{1}{2}\hat{n}\times\overline{\mathbf{I}}+\overline{\mathbf{K}}_{ext} & \overline{\mathbf{D}}^T\cdot\overline{\mathbf{P}}_{ext}\cdot\overline{\mathbf{B}}\\ \overline{\mathbf{V}}_{int} & \frac{1}{2}\hat{n}\times\overline{\mathbf{I}}+\overline{\mathbf{K}}_{int} & \overline{\mathbf{D}}^T\cdot\overline{\mathbf{P}}_{int}\cdot\overline{\mathbf{B}}\\ \overline{\mathbf{F}}\cdot\overline{\mathbf{D}} & 0 & k_0^2\overline{\mathbf{I}}_r\end{bmatrix}\cdot\begin{bmatrix}ik_0\mathbf{J}\\ \eta_0^{-1}\mathbf{M}\\ c_0\boldsymbol{\rho}_r\end{bmatrix}=\begin{bmatrix}-\eta_0^{-1}\mathbf{b}\\ 0\\ 0\end{bmatrix} \quad (2.18)$$

where the matrix elements are:

$$\left[\overline{\mathbf{V}}\right]_{mn}=\mu_r\int_S d\mathbf{r}\mathbf{T}_m(\mathbf{r})\cdot\int_{S'}ed\mathbf{r}'g(\mathbf{r},\mathbf{r}')\mathbf{\Lambda}_n^J(\mathbf{r}') \quad (2.19)$$

$$\left[\overline{\mathbf{K}}\right]_{mn}=\int_S d\mathbf{r}\mathbf{T}_m(\mathbf{r})\cdot\oint_{S'}d\mathbf{r}'\nabla' g(\mathbf{r},\mathbf{r}')\times\mathbf{\Lambda}_{\mathbf{n}}^{\mathbf{M}}(\mathbf{r}') \quad (2.20)$$

$$\left[\overline{\mathbf{P}}\right]_{mn} = \epsilon_r^{-1} \int_S d\mathbf{r} \nabla \cdot \mathbf{T}_m(\mathbf{r}) \int_{S'} d\mathbf{r}' g(\mathbf{r}, \mathbf{r}') \nabla' \cdot \mathbf{\Lambda}_n^J(\mathbf{r}') \tag{2.21}$$

$$\left[\hat{n} \times \overline{\mathbf{I}}\right]_{mn} = \int_S d\mathbf{r} \mathbf{T}_m(\mathbf{r}) \cdot \left(\hat{n}(\mathbf{r}) \times \mathbf{\Lambda}_{\mathbf{n}}^{\mathbf{M}}(\mathbf{r})\right) \tag{2.22}$$

Other matrices and vectors are defined in the same way as those in (2.5). Note that the testing and basis functions are not specified yet.

2.3.2 Testing and Basis Functions

Equation (2.18) solves the external and internal problems using A-EFIE. It provides an elegant way to solve dielectric problems at low frequencies. However, if the testing and basis functions are not chosen appropriately, the system matrix is ill-conditioned and the problem is still unsolvable. A few requirements need to be satisfied in order to produce a well-tested, well-conditioned system matrix. First, the basis functions to expand the electric and magnetic currents should be divergence-conforming. Other non-divergence conforming basis functions will produce fictitious line charges [30]. Second, the external and internal A-EFIEs should be tested with divergence conforming basis functions. This is because the dual space of the curl-conforming electric field is the divergence-conforming function space [34] [31].

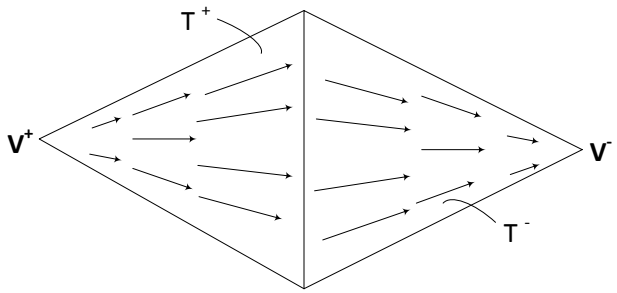

Figure 2.1: RWG divergence conforming basis function on two triangle patches. The triangles T^+ and T^- are the positive charge and negative charge patches; $\mathbf{V}^+$ and $\mathbf{V}^-$ are the vertices of the patches.

The widely used RWG basis function, as shown in Figure 2.1, can be

normalized. The definition and the divergence of this function are:

$$\mathbf{\Lambda}(\mathbf{r}') = \begin{cases} \frac{1}{2A^+}(\mathbf{r}' - \mathbf{V}^+) & \text{if } \mathbf{r}' \in T^+ \\ -\frac{1}{2A^-}(\mathbf{r}' - \mathbf{V}^-) & \text{if } \mathbf{r}' \in T^- \end{cases} \tag{2.23}$$

$$\nabla \cdot \mathbf{\Lambda}(\mathbf{r}') = h(\mathbf{r}') = \begin{cases} \frac{1}{A^+} & \text{if } \mathbf{r}' \in T^+ \\ -\frac{1}{A^-} & \text{if } \mathbf{r}' \in T^- \end{cases} \tag{2.24}$$

where the divergence of it is the pulse basis function h.

Apparently, this basis function is divergence conforming and suitable to be used as the testing and basis function. This is why the RWG basis function is widely applied to EFIE and A-EFIE for PEC effectively. Therefore, we can use the RWG basis function to test the external and internal A-EFIE and to expand the electric current in (2.18). This will give rise to well-conditioned matrices $\overline{\mathbf{V}}$ and $\overline{\mathbf{P}}$. However, there is a testing problem if the magnetic current is also expanded with the RWG function.

One can write down the matrix element related to the magnetic current $\mathbf{M}$ in (2.20) more explicitly:

$$\begin{aligned} \left[\pm\frac{1}{2}\hat{n}\times\bar{\mathbf{I}}+\overline{\mathbf{K}}\right]_{mn} &= \pm\frac{1}{2}\int_S d\mathbf{r}\mathbf{T}_m(\mathbf{r})\cdot\left(\hat{n}\times\mathbf{\Lambda}_{\mathbf{n}}^{\mathbf{M}}(\mathbf{r})\right) \\ &\quad + \int_S d\mathbf{r}\mathbf{T}_m(\mathbf{r})\cdot\int_{S'} d\mathbf{r}'\nabla' g(\mathbf{r},\mathbf{r}')\times\mathbf{\Lambda}_{\mathbf{n}}^{\mathbf{M}}(\mathbf{r}') \end{aligned} \tag{2.25}$$

If $\mathbf{T}(\mathbf{r}) = \mathbf{\Lambda}(\mathbf{r})$ and $\mathbf{\Lambda}^M(\mathbf{r}) = \mathbf{\Lambda}(\mathbf{r})$, i.e. both the testing and basis functions are the RWG basis function, one can observe that the first term in (2.25) vanishes because $\mathbf{\Lambda}(\mathbf{r})\cdot(\hat{n}\times\mathbf{\Lambda}(\mathbf{r})) = 0$. The second term will be very small if S and S' are very close to each other on a smooth surface. As a result, the diagonal terms of the matrix $[\overline{\mathbf{K}}]_{nn} \approx 0$. The matrix element $[\overline{\mathbf{K}}]_{mn}$ represents the amplitude of field radiated from n-th patch to m-th patch. It should be a large scalar number when S and S' are close. This contradiction reveals that using the RWG as the testing and basis function produces a poorly tested and ill-conditioned matrix $\overline{\mathbf{K}}$.

This testing issue is solved by keeping the RWG as the testing function and introducing another divergence-conforming basis function, denoted as $\mathbf{\Gamma}$,

to represent the equivalent magnetic current $\mathbf{M}$:

$$\mathbf{T} = \mathbf{\Lambda}, \quad \mathbf{\Lambda}^M = \mathbf{\Gamma} \tag{2.26}$$

In order to maximize $\mathbf{\Lambda}_m(\mathbf{r}) \cdot (\hat{n} \times \mathbf{\Gamma}_\mathbf{n}(\mathbf{r}))$, the function $\mathbf{\Gamma}(\mathbf{r})$ should be almost orthogonal to $\mathbf{\Lambda}(\mathbf{r})$ [35]. Many efforts have been made to use $\hat{n} \times \mathbf{\Lambda}$ in the MFIE formulation, although it produces fictitious line current since it is not divergence conforming. Other types of dual basis functions, such as Chen-Wilton basis function [5] and Buffa-Christiansen (BC) basis function [6, 31], can also be used. In this chapter, we use the BC basis function, as shown in Figure 2.2. It is divergence-conforming and it is almost orthogonal to the RWG basis function. As a result, the fictitious line current is avoided and the resulting $\overline{\mathbf{K}}$ is a diagonally dominant and well-conditioned matrix.

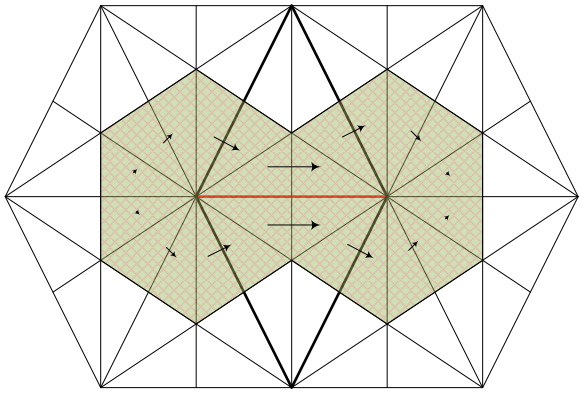

Figure 2.2: Buffa-Christiansen (BC) [6] divergence conforming, quasi curl conforming basis function on a barycentric mesh. The shaded region is the domain of the basis function of the reference edge (in red). The arrows indicate the directions and the amplitudes. Note that the Chen-Wilton basis function [5] is also an alternative.

In summary, the RWG basis function $\mathbf{\Lambda}$ is used as the testing function of the equations and the basis function of $\mathbf{J}$, while the BC basis function is used to expand $\mathbf{M}$. In this manner, the matrices $\overline{\mathbf{V}}$, $\overline{\mathbf{P}}$, and $\overline{\mathbf{K}}$ are all well-tested and the system matrix is well-conditioned.

2.3.3 Preconditioner for Dielectric Formulation

The problem in (2.5) and (2.18) are classified as the generalized saddle point problem [36, 37]. A preconditioner is generally needed as the convergence rate is not satisfactory when the iterative solver is adopted for a large-scale problem. A right preconditioner is employed for this solver. Motivated by the work in [36, 37], we propose a preconditioning matrix by using a factorization of a block matrix:

$$\begin{bmatrix} \overline{\mathbf{A}} & \overline{\mathbf{U}} \\ \overline{\mathbf{V}} & \overline{\mathbf{D}} \end{bmatrix} = \begin{bmatrix} \bar{\mathbf{I}} & \bar{\mathbf{0}} \\ \overline{\mathbf{V}}\overline{\mathbf{A}}^{-1} & \bar{\mathbf{I}} \end{bmatrix} \cdot \begin{bmatrix} \overline{\mathbf{A}} & \bar{\mathbf{0}} \\ \bar{\mathbf{0}} & \overline{\mathbf{D}} - \overline{\mathbf{V}}\overline{\mathbf{A}}^{-1}\overline{\mathbf{U}} \end{bmatrix} \cdot \begin{bmatrix} \bar{\mathbf{I}} & \overline{\mathbf{A}}^{-1}\overline{\mathbf{U}} \\ \bar{\mathbf{0}} & \bar{\mathbf{I}} \end{bmatrix} \tag{2.27}$$

In (2.18), the inverse of the system matrix can be factorized as:

$$\begin{aligned} \overline{\mathbf{M}}^{-1} &= \begin{bmatrix} \bar{\mathbf{I}} & -\overline{\boldsymbol{\alpha}}^{-1}\overline{\boldsymbol{\beta}} \\ 0 & \bar{\mathbf{I}} \end{bmatrix} \cdot \begin{bmatrix} \overline{\boldsymbol{\alpha}}^{-1} & 0 \\ 0 & \overline{\boldsymbol{\Delta}}^{-1} \end{bmatrix} \cdot \begin{bmatrix} \bar{\mathbf{I}} & 0 \\ \overline{\boldsymbol{\gamma}} \cdot \overline{\boldsymbol{\alpha}}^{-1} & \bar{\mathbf{I}} \end{bmatrix} \\ &= \begin{bmatrix} \overline{\boldsymbol{\alpha}}^{-1} & 0 \\ 0 & 0 \end{bmatrix} + \begin{bmatrix} -\overline{\boldsymbol{\alpha}}^{-1} \cdot \overline{\boldsymbol{\beta}} \\ \bar{\mathbf{I}} \end{bmatrix} \cdot \overline{\boldsymbol{\Delta}}^{-1} \cdot \begin{bmatrix} -\overline{\boldsymbol{\gamma}} \cdot \overline{\alpha}^{-1} & \bar{\mathbf{I}} \end{bmatrix} \end{aligned} \tag{2.28}$$

where

$$\overline{\boldsymbol{\alpha}} = \begin{bmatrix} \overline{\mathbf{V}}_{ext} & \overline{\mathbf{K}}_{ext} \\ \overline{\mathbf{V}}_{int} & \overline{\mathbf{K}}_{int} \end{bmatrix} \tag{2.29}$$

$$\overline{\boldsymbol{\beta}} = \begin{bmatrix} \overline{\mathbf{D}}^T \cdot \overline{\mathbf{P}}_{ext} \cdot \overline{\mathbf{B}} \\ \overline{\mathbf{D}}^T \cdot \overline{\mathbf{P}}_{int} \cdot \overline{\mathbf{B}} \end{bmatrix} \tag{2.30}$$

$$\overline{\boldsymbol{\gamma}} = \begin{bmatrix} \overline{\mathbf{F}} \cdot \overline{\mathbf{D}} & 0 \end{bmatrix} \tag{2.31}$$

and $\overline{\boldsymbol{\Delta}}$ is the Schur complement matrix:

$$\overline{\boldsymbol{\Delta}} = k_0^2 \bar{\mathbf{I}}_r - \overline{\boldsymbol{\gamma}} \cdot \overline{\boldsymbol{\alpha}}^{-1} \cdot \overline{\boldsymbol{\beta}} \tag{2.32}$$

Since the matrices $\overline{\boldsymbol{\alpha}}$, $\overline{\boldsymbol{\beta}}$ and $\overline{\boldsymbol{\Delta}}$ are dense, and a preconditioner only requires an approximation of the inverse of the system matrix, we use the

diagonal terms to construct the preconditioner:

$$\overline{\boldsymbol{\alpha}} = \begin{bmatrix} \left[\overline{\mathbf{V}}_{ext}\right]_{diag} & \left[\overline{\mathbf{K}}_{ext}\right]_{diag} \\ \left[\overline{\mathbf{V}}_{int}\right]_{diag} & \left[\overline{\mathbf{K}}_{int}\right]_{diag} \end{bmatrix} \tag{2.33}$$

$$\overline{\boldsymbol{\beta}} = \begin{bmatrix} \overline{\mathbf{D}}^T \cdot \left[\overline{\mathbf{P}}_{ext}\right]_{diag} \cdot \overline{\mathbf{B}} \\ \overline{\mathbf{D}}^T \cdot \left[\overline{\mathbf{P}}_{int}\right]_{diag} \cdot \overline{\mathbf{B}} \end{bmatrix} \tag{2.34}$$

Then the inverse of $\overline{\boldsymbol{\alpha}}$ can be obtained analytically as $\overline{\boldsymbol{\alpha}}$ is a 2×2 block matrix with each block as a diagonal matrix. After these treatments, $\overline{\mathbf{M}}^{-1}$ is decomposed into sparse matrix multiplications and a summation. One can solve $\overline{\boldsymbol{\Delta}} \cdot \mathbf{y}' = \mathbf{x}'$ with the multifrontal method to achieve the product of $\overline{\boldsymbol{\Delta}}^{-1}$ and $\mathbf{x}'$. The size of the matrix that needs to be solved numerically is reduced from $2e + p$ to p, where e and p are the numbers of the edges and the patches respectively. Meanwhile, the number of non-zero elements is reduced. Then the numerical solution for $\mathbf{y}'$ in $\overline{\boldsymbol{\Delta}} \cdot \mathbf{y}' = \mathbf{x}'$ becomes more efficient.

2.3.4 Mixed-Form Fast Multipole Algorithm

In order to tackle multi-scale EM problems with a large number of unknowns, an iterative solver with an accelerated matrix vector product is preferred over direct solvers. Meanwhile, both the low-frequency and mid-frequency physics should be captured accurately because multi-scale structures involve very small details and relatively large geometries. A fast algorithm, termed mixed-form fast multipole algorithm [32], is adopted. This algorithm is based on fast multipole algorithm (FMA) and combines the multipole and plane wave expansions of EM wave adaptively. When the box sizes at low levels of an octree are small compared to the wavelength (for example, smaller than 0.1 wavelengths), EM waves are aggregated, translated and disaggregated by multipoles to capture the low-frequency physics. As the box sizes in higher levels are comparable to the wavelength, the multipole expansions are converted to the plane wave representations to capture the wave physics. Therefore, both the small-scale and large-scale parts can be accelerated accurately and efficiently. As for the computational cost, if only multipole expansions are used, the computational cost of the matrix vector product is reduced from $O(N^2)$ to $O(N)$. If both the multipole and plane wave expansions are involved, the cost is reduced to $O(N \log N)$. However, to capture

the wave physics, the use of plane wave expansion is warranted.

In the matrix equation (2.18), the matrix vector products related to the dense matrices $\overline{\mathbf{V}}$, $\overline{\mathbf{K}}$, and $\overline{\mathbf{P}}$ can be accelerated with the mixed-form FMA, for both external and internal regions. Other matrices, $\overline{\mathbf{D}}$, $\overline{\mathbf{F}}$, $\overline{\mathbf{B}}$, and $\overline{\mathbf{I}}_r$, are highly sparse and the computational cost is $O(N)$. Therefore, the overall cost of the matrix vector product is either $O(N \log N)$ or $O(N)$, depending on the expansions of the waves and the frequency.

With the mixed-form FMA, problems with over 1 million unknowns can be solved with an affordable computational expense, as shall be shown in Section 2.4.

2.4 Numerical Results

In this section, some numerical validations of this method are presented. Using only the method of moment (MoM), the condition numbers of three sets of meshes are studied. Then the convergence histories with and without the proposed preconditioner are compared to show the effectiveness of this preconditioner. After that, scattering problems are solved and compared with Mie series and other numerical solvers, which show that accurate results can be obtained. Moreover, a lossy material problem is presented using this method. Finally, some other numerical examples with a large number of unknowns and their computational costs are presented.

2.4.1 Condition Number of the System Matrix

The matrix elements of the system matrix in (2.18) can be filled using MoM. Then the condition numbers of the system matrices at various frequencies are computed for three sets of meshes (A, B and C) of a 1 m sphere with relative permittivity $\epsilon_r = 2.0$. Table 2.1 shows the numbers of the edges and triangles for the meshes.

By sweeping the frequencies from 3×10^{-3} to 3×10^{8} Hz, the condition numbers are recorded. Figure 2.3 shows the condition numbers as a function of frequency. It is apparent that the system matrices have a constant condition number at low frequencies. This is because the frequency-dependent parameters of the operators $\mathcal{L}$, $\mathcal{K}$, and $\mathcal{P}$ have been moved to the unknowns,

Table 2.1: Geometry information of the meshes.

Mesh ID	Number of Edges	Number of Triangles
Mesh A	954	636
Mesh B	2196	1464
Mesh C	4014	2676

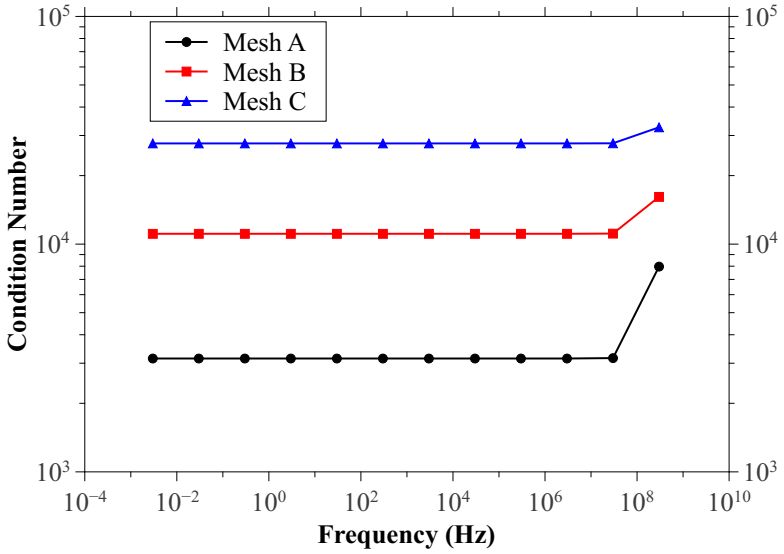

Figure 2.3: The condition numbers of the system matrices as frequency varies for three sets of meshes.

instead of the matrix elements. Therefore, a relatively small condition number and a fast convergence rate are guaranteed for low-frequency problems. As the mesh becomes denser, the condition number of the system matrix increases due to the spectrum of the $\mathcal{L}$ operator [34].

2.4.2 Convergence History

For large-scale problems, an iterative solve is usually used to replace the direct solver, such as LU decomposition. The computational cost will be reduced from N^3 to N^2. Two kinds of iterative solvers, GMRES [38] and BiCGSTAB [39], are applied to solve the scattering problem of a sphere (mesh A) excited by the plane wave at 10 Hz. The restart number of the GMRES solver is set to 30 and GMRES-30 is used to denote this configuration.

The convergence histories using these two iterative solvers are recorded

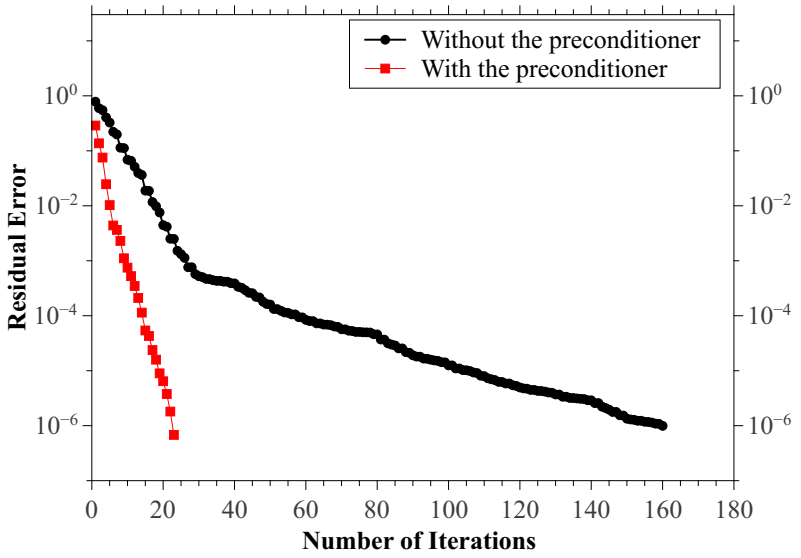

Figure 2.4: A comparison of the convergence histories of the GMRES-30 solver with and without the preconditioner for mesh C.

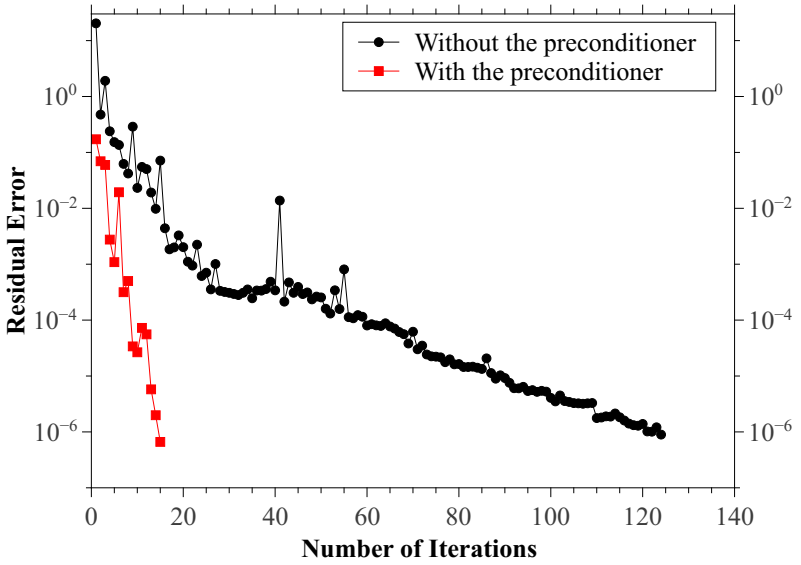

Figure 2.5: A comparison of the convergence histories of the BiCGSTAB solver with and without the preconditioner for mesh C.

with and without the proposed pre-conditioner in (2.28). Figures 2.4 and 2.5 show the recorded convergence histories of mesh C. Both comparisons illustrate a superior convergence performance with the preconditioner. Using the preconditioner, both iterative solvers converge to a relative error of 10^{-6} within 23 iterations, while it takes over 120 iterations without the

Table 2.2: Numbers of iterations with and without the preconditioner using GMRES and BiCGSTAB.

	Number of Iterations (with Preconditioning)		Number of Iterations (without Preconditioning)	
Mesh ID	GMRES-30	BiCGSTAB	GMRES-30	BiCGSTAB
Mesh A	23	15	160	124
Mesh B	28	19	230	164
Mesh C	34	24	470	285

preconditioner. It is also validated by numerical experiments, as shown in Table 2.2, that for a simple structure like a sphere, with the preconditioning, the number of iterations stays rather stable as the mesh density increases. However, without preconditioning, dramatic increase in the numbers of iterations is observed. The conditioned and unconditioned system converge to the same solution, as can be observed from Figure 2.6: the error is about $O(10^5)$ smaller than the amplitude of the solution.

2.4.3 Scattering

To validate the accuracy of this formulation, sphere and cube scattering simulations with the mixed-form FMA accelerations are performed. Both the plane wave and the point source are used as the excitation source. Radar cross section (RCS) and near field are computed for the plane-wave excitation. Both results are compared with the corresponding Mie series.

A sphere of 1 m radius and relative permittivity $\epsilon_r = 11.7$ (silicon) is located at the origin. It is discretized into 35,136 edges and 23,424 triangles. Therefore the total number of unknowns is 93,695. The plane wave is propagating in the z direction and polarized in the x direction. The RCS is computed on the **E**-plane (xz plane) and **H**-plane (yz plane).

GMRES-30 is chosen for this simulation. The relative error tolerance is set to 10^{-4}. Figure 2.7 shows the simulation and Mie series comparisons at the **E** and **H** planes when excited by the plane wave at 30 Hz. A cube of 1 m^3 volume with relative permittivity $\epsilon_r = 12.9$ (GaAs) is simulated as well. There are 12,885 edges and 8,590 triangles in the mesh. Figure 2.8 shows the comparisons of RCSs at 100 MHz using the A-EFIE solver for dielectrics

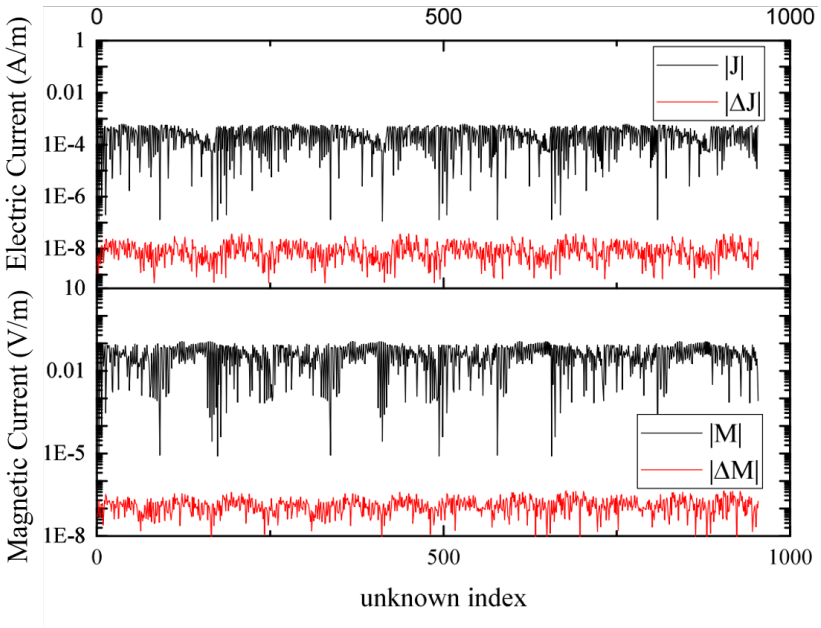

Figure 2.6: A comparison of the solutions to the preconditioned and unpreconditioned systems.

and the finite element boundary integral (FEBI) solver [40] . Obviously, the comparisons to analytical solutions and FEBI show a good accuracy of this formulation.

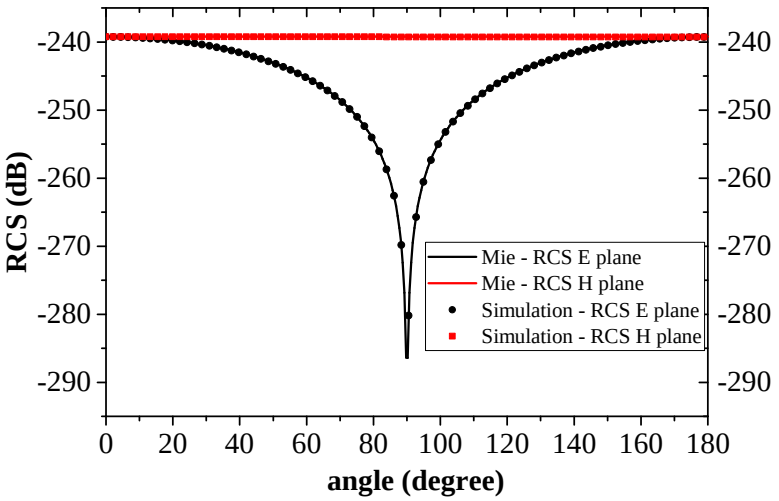

Figure 2.7: A comparison of the simulated RCS and the Mie series results on the electric field plane (E plane) and the magnetic field plane (H plane).

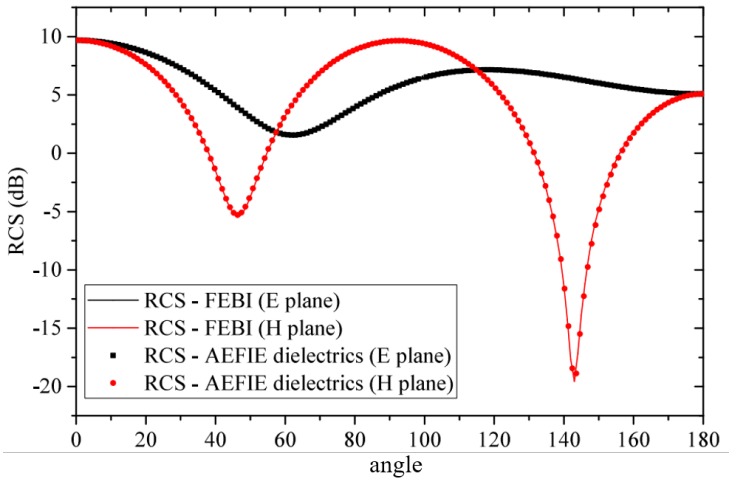

Figure 2.8: A comparison of the simulated RCS and FEBI results at 100 MHz for a cube.

Both simulation results in Figures 2.7 and 2.8 match well with the Mie series and other numerical solvers, validating the accuracy of this formulation at mid and low frequencies. It is to be noted that if the frequency approaches zero, there exists a low-frequency inaccuracy issue. This problem can be remedied by the perturbation theory as discussed in [28].

Table 2.3: Computational costs of the periodic-structure problems. (Simulations are performed on a computer with 6-core Intel Xeon CPU with 2.30 GHz clock and 64 GB RAM.)

Mesh ID	Mesh D	Mesh E	Mesh F	Mesh G
Total Number of Unknowns	317,999	549,503	872,591	1,302,527
Total Number of Iterations	22	23	23	23
Total Iteration Time (s)	476.0	714.0	1870	3024
Time per Iteration (s)	20.7	31.0	81.3	131.5
Peak Memory Usage (GB)	5.3	10.1	11.8	15.6

2.4.4 Periodic Array Scattering

Periodic arrays are also simulated to validate the large-scale stability of this solver. Multiple copies of spheres with 10 μm radius are aligned periodically in x, y, and z directions. The period is 30 μm in each direction. Four sets of meshes, namely D ($5 \times 5 \times 5$ elements), E ($6 \times 6 \times 6$ elements), F

($7\times7\times7$ elements) and G ($8\times8\times8$ elements) are simulated at the frequency of 300 GHz under the illumination of the plane wave. Table 2.3 shows the computational cost of iterative solver with the mixed form FMA acceleration for each problem. It is seen that problems with over 1 million unknowns can be solved with reasonable computational costs.

Figure 2.9 shows the electric charge distributions when the periodic array D is illuminated by the plane wave with x polarization at 300 GHz. It is observed that the charge distributions of the small spheres of 10 μm radius look like electric dipoles, which is consistent with the expectation and physics of small particle scattering.

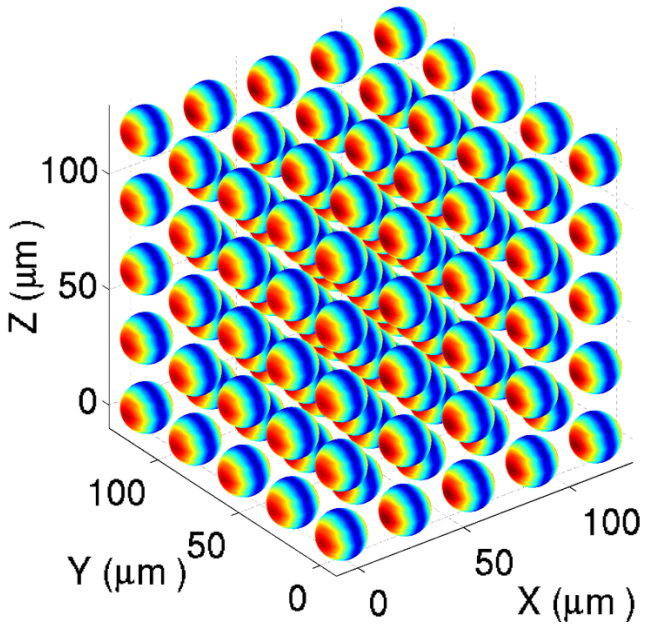

Figure 2.9: The electric charge distribution on mesh D, excited by a plane wave at 300 GHz.

2.4.5 Lossy Plasmonic Material

This method can be used for conductive and plasmonic materials if the material is not extremely lossy. Otherwise, special treatments of the lossy kernel integrations are required [41]. Simulations of two closely spaced spheres are performed to demonstrate the near field coupling of gold particles. The complex permittivity of gold at optical frequency is obtained from the Brendel-Bormann model [42], for example, $\epsilon_r = -5.33 + 1.97i$ at 550 nm. In order

that this simulations is performed at long wavelength regime, the diameters of the two spheres are 15 nm and they are spaced 1.5 nm away from each other. A near field profile on $z = 0$ plane is shown in Figure 2.10. Note that the total field inside the gold sphere is set to zeros. One can observe that the dipole-dipole coupling between the two gold particles greatly enhances the field at the gap region. This solver will be potentially useful to study plasmonic resonance.

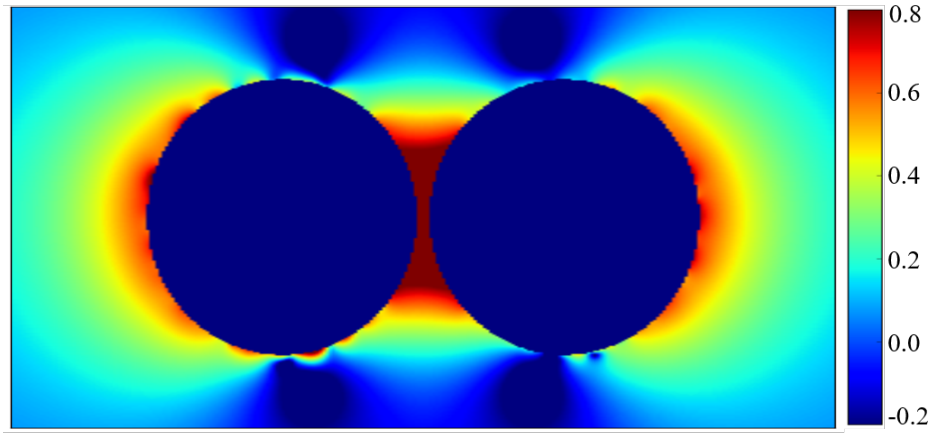

Figure 2.10: The total near field profile of the two gold spheres at wavelength $\lambda = 550$ nm.

2.5 Conclusion

The new A-EFIE formulation for dielectrics is fully developed in this chapter. The original A-EFIE for PEC is utilized for the external region. For the internal region, a similar technique is applied. From the BC and Chen-Wilton basis functions, we choose to use the BC basis function. Then a well-conditioned system matrix can be formulated. The accuracy of this method is validated with the comparisons to the Mie series and other numerical solutions. The proposed pre-conditioning scheme also proves to be effective and efficient by the numerical results. With the simulations of the periodic spherical arrays, it can be seen that this is an efficient method for problems with over 1 million unknowns. With the simulations of the nano-particles, we demonstrate that this method can be potentially useful for lossy materials simulations and the study of plasmonic resonance.

Chapter 3

The Enhanced Augmented Electric Field Integral Equation for Conductive Structures

3.1 Introduction

Computational electromagnetics (CEM) has been widely used in the simulations of circuit interconnect problems. As the operation frequency increases, there are needs for CEM tools to capture the low-frequency physics (of which some CEM methods fail to capture), as well as the wave physics (of which conventional quasi-static methods fail to capture). To satisfy this broadband stability requirement, some methods [7, 8, 24, 25, 14] have been developed for perfect electric conductor (PEC) structures. In these methods, the low-frequency issues in the integral equation method and finite element method are well addressed. Among these methods, we are particularly interested in the augmented electric field integral equation (A-EFIE) since at low- and mid-frequencies, this method is accurate and stable [14], and no loop-tree decomposition is required.

As the fine details get increasingly smaller in many circuit interconnect and nanotechnology applications, the skin effects become an important issue. Therefore, approximating good conductors as PEC is no longer valid. A simple remedy is to use the Leontovich boundary condition [43], which is also known as the impedance boundary condition (IBC) [44]. In this approximation model, the equivalent electric and magnetic currents are orthogonal to each other and related by the surface impedance of the conductor. As a result, the magnetic current can be expressed in terms of the electric current and the pertinent matrix equation becomes simple. Some research has been done to formulate the IBC solvers [45, 46, 47] with different combinations of the electric field integral equation (EFIE) and magnetic field integral equation (MFIE). A combination of the Rao-Wilton-Glisson (RWG) basis function [4] and the Buffa-Christiansen basis functions [6], which is widely

used in the Calderón pre-conditioners [31, 48], were also used to formulate IBC solvers. But the study of the application of IBC to the AEFIE has not been reported. Although the IBC approximation has proved effective in the high-frequency regime for good conductors, it becomes inaccurate as the skin depth becomes comparable to the size of the structures, especially in low-frequency applications and for small scale problems.

When the skin depth becomes large, the localized IBC is not sufficient to describe the relationship between the electric and magnetic currents. Instead, a global IBC is required. A global surface impedance (GSI) [49] for the partial-element equivalent circuit (PEEC) method was proposed to address this issue in conductors. This method models the cross section using finite differences to find the global relationship between the electric and magnetic currents. Therefore, this method is especially useful for structures with fixed cross section. For arbitrary structures, however, the computational cost will increase. This method is useful when the skin depth is compared to the wavelength and the loop-tree decomposition [7, 8] is employed to overcome the low-frequency breakdown. However, the cases of arbitrary large skin depth were not discussed.

Another rigorous full wave approach was proposed in [50]. The internal problem is solved with MFIE and a matrix is generated to represent the coupling between the electric and magnetic currents. However, the ill-conditioned issue [34, 51] persists: the basis function and the testing function are not orthogonal to each other for the MFIE operator, which gives rise to an ill-conditioned matrix. Meanwhile, in [50], the low-frequency issue has not been addressed.

Another low-frequency stable formulation [29] can be used to solve dielectric and conductor problems. Alternatively, we can also solve the highly conductive materials as dispersive media using the AEFIE method for dielectrics [52, 53]. In this chapter, we will first briefly introduce the formulation of this method. The augmentation technique is applied and the low-frequency breakdown is properly solved. We then derive a new set of equations to evaluate the integrals of Green's function in lossy media. These equations are motivated by a simple approximation method for Green's function in very lossy media. As a result, this method is very accurate in the evaluation of these integrals. Then we will show that this method can be regarded as a generalized impedance boundary condition method, since it

reduces to an IBC formulation if the electric and magnetic currents are assumed coupled locally. Then this method is accelerated with the mixed-form fast multipole algorithm (FMA) [32], and a preconditioner suitable for saddle point problems [36]. Finally some numerical examples are presented to validate the method, as well as demonstrating its capabilities of solving complex problems with a large number of unknowns.

3.2 Methods

To solve the conductor problems, we adopt the formulation from our previous work: the AEFIE for dielectrics [52]. We will first briefly introduce the formulation in this section. However, there are some concerns regarding solving conductors as dispersive dielectric media using this method. First, the evaluations of the integrals associated with the fast oscillatory and decaying Green's function, which appears in the case of conductors, become inaccurate using the conventional singularity subtraction method [54, 55]. A more robust method is proposed to overcome this difficulty. Second, we will study how this formulation converges to the impedance boundary condition (IBC) approximation and perfect electric conductor (PEC) cases as the conductivity increases. Then this method will be a general formulation valid from dielectrics to conductors.

3.2.1 Formulation

The formulation for general dielectrics was presented in [52]. The matrix equation is:

$$\begin{bmatrix} \overline{\mathbf{V}}_{ext} & -\frac{1}{2}\hat{n}\times\overline{\mathbf{I}}+\overline{\mathbf{K}}_{ext} & \overline{\mathbf{D}}^{T}\cdot\overline{\mathbf{P}}_{ext}\cdot\overline{\mathbf{B}} \\ \overline{\mathbf{V}}_{int} & \frac{1}{2}\hat{n}\times\overline{\mathbf{I}}+\overline{\mathbf{K}}_{int} & \overline{\mathbf{D}}^{T}\cdot\overline{\mathbf{P}}_{int}\cdot\overline{\mathbf{B}} \\ \overline{\mathbf{F}}\cdot\overline{\mathbf{D}} & 0 & k_0^2\overline{\mathbf{I}}_r \end{bmatrix} \cdot \begin{bmatrix} ik_0\mathbf{J} \\ \eta_0^{-1}\mathbf{M} \\ c_0\boldsymbol{\rho}_r \end{bmatrix} = \begin{bmatrix} -\eta_0^{-1}\mathbf{b} \\ 0 \\ 0 \end{bmatrix} \tag{3.1}$$

where the matrix elements are:

$$\left[\overline{\mathbf{V}}\right]_{mn} = \mu_r \int_S d\mathbf{r}\mathbf{T}_m(\mathbf{r}) \cdot \int_{S'} d\mathbf{r}' g_i(\mathbf{r},\mathbf{r}')\mathbf{\Lambda}_n^J(\mathbf{r}') \tag{3.2}$$

$$\left[\overline{\mathbf{K}}\right]_{mn} = \int_S d\mathbf{r}\mathbf{T}_m(\mathbf{r}) \cdot \int_{S'} d\mathbf{r}'\nabla' g_i(\mathbf{r},\mathbf{r}') \times \mathbf{\Lambda}_\mathbf{n}^\mathbf{M}(\mathbf{r}') \tag{3.3}$$

$$\left[\overline{\mathbf{P}}\right]_{mn} = \epsilon_r^{-1} \int_S d\mathbf{r}\nabla \cdot \mathbf{T}_m(\mathbf{r}) \int_{S'} d\mathbf{r}' g_i(\mathbf{r},\mathbf{r}')\nabla' \cdot \mathbf{\Lambda}_n^J(\mathbf{r}') \tag{3.4}$$

$$\left[\hat{n} \times \overline{\mathbf{I}}\right]_{mn} = \int_S d\mathbf{r}\mathbf{T}_m(\mathbf{r}) \cdot \left(\hat{n}(\mathbf{r}) \times \mathbf{\Lambda}_\mathbf{n}^\mathbf{M}(\mathbf{r})\right) \tag{3.5}$$

$$[\mathbf{b}]_m = \int_{S'} d\mathbf{r}\mathbf{T}_m(\mathbf{r}) \cdot \mathbf{E}_{inc}(\mathbf{r}) \tag{3.6}$$

and $\overline{\mathbf{D}}$ is the matrix representation of the divergence operator, $\overline{\mathbf{B}}$ is a matrix that maps from the reduced charge unknowns $\boldsymbol{\rho}_r$ to the conventional charge unknowns $\boldsymbol{\rho}$, $\overline{\mathbf{F}}$ is the reverse mapping matrix [14], and $g_i(\mathbf{r},\mathbf{r}')$ is the Green's function, where the subscript i can be ext or int to represent the external or internal regions, $\mathbf{T}(\mathbf{r})$ is the testing function, $\mathbf{\Lambda}(\mathbf{r})$ is the basis function while the superscript J and M are used to denote the basis function for the electric current and the magnetic current.

The inner integral in (3.3) is the principal value integral, while the residual part is absorbed into the identity term, by assuming that the surface is smooth. In summary, the RWG basis function [4] is used as the testing function and basis function for $\mathbf{J}$ and the Buffa-Christiansen (BC) basis function [6] is used as the basis function for $\mathbf{M}$. More detailed discussions can be found in [52].

The matrix equation in (3.1) can be extended to solving conductor problems, by solving the internal problem as lossy dielectrics. In the next subsections, we will investigate the evaluations of the inner integrals in the matrix elements (3.2)–(3.4).

3.2.2 Integral Evaluations

The first equation in (3.1) is the integral equation in the external region, which is usually dielectric with little or no losses. The integrals in this region can be accurately calculated using the conventional singularity subtraction method. The second equation in (3.1) represents the integral equation inside the object medium. For conductors, assuming non-magnetic, the complex

wave number k is:

$$k = \omega\sqrt{\epsilon\mu} = k_0\sqrt{\epsilon_r' + i\frac{\sigma}{\omega\epsilon_0}} = k' + ik'' \tag{3.7}$$

If $\epsilon_r' \ll \frac{\sigma}{\omega\epsilon_0}$, $k' \approx k''$ and $k' \approx k_0\sqrt{\frac{\sigma}{2\omega\epsilon_0}}$.

Then in (3.2)–(3.4), the Green's function becomes:

$$g(\mathbf{r}, \mathbf{r}') = \frac{1}{4\pi R}e^{ik'R}e^{-k''R} \tag{3.8}$$

where $R = |\mathbf{r} - \mathbf{r}'|$. This represents a fast oscillatory and decaying function.

To evaluate the integrals in (3.2)–(3.4) and the subsequent calculations of the field from $\mathbf{J}$ and $\mathbf{M}$, we emphasize on the evaluations of the inner integral. They are of the form:

$$I_1 = \int_{S'} d\mathbf{r}' \frac{e^{ikR}}{4\pi R} \tag{3.9}$$

$$\mathbf{I}_2 = \int_{S'} d\mathbf{r}' \frac{e^{ikR}}{4\pi R}(\mathbf{r}' - \mathbf{q}) \tag{3.10}$$

$$\mathbf{I}_3 = \int_{S'} d\mathbf{r}' \nabla \left(\frac{e^{ikR}}{4\pi R}\right) \tag{3.11}$$

$$\mathbf{I}_4 = \int_{S'} d\mathbf{r}' \nabla \left(\frac{e^{ikR}}{4\pi R}\right) \times (\mathbf{r}' - \mathbf{q}) \tag{3.12}$$

where $\mathbf{q}$ is usually a vertex of the triangle S'.

3.2.2.1 Conventional Singularity Subtraction

One way to evaluate these is to use the conventional singularity subtraction method [54, 55]. The singular parts are extracted and evaluated analytically.

The non-singular parts are calculated numerically using quadratures. However, as will be shown later in Figure 3.2, this approach gives rise to large errors if the material is highly lossy. This is due to that the singular terms are not the major contributions to the integrals (3.9)–(3.12), and the evaluations of the non-singular parts are inaccurate.

3.2.2.2 Circle Approximation

We can investigate the major contributions to the integrals by making some assumptions: Assuming that the observation point $\mathbf{r}$ lies on the source triangle and k'' is large compared to the inverse of the triangle size, the integral domain S' can be approximated by a circular domain C', which is centered at $\mathbf{r}$ and has a radius of R, i.e.

$$\int_{S'} d\mathbf{r}' g(\mathbf{r}, \mathbf{r}') \approx \int_{C'} d\mathbf{r}' g(\mathbf{r}, \mathbf{r}') \tag{3.13}$$

Therefore $k''R \to \infty$, $e^{ikR} \to 0$ and

$$\int_{C'} d\mathbf{r}' g(\mathbf{r}, \mathbf{r}') = 2\pi \int_0^R d\rho\rho \frac{e^{ik\rho}}{4\pi\rho} = \frac{i}{2k} \tag{3.14}$$

Similarly, another integral can be approximated as:

$$\begin{aligned} \int_{C'} d\mathbf{r}' g(\mathbf{r}, \mathbf{r}')(\mathbf{r}' - \mathbf{q}) &= 2\pi \int_0^R d\rho\rho \frac{e^{ik\rho}}{4\pi\rho}(\mathbf{r}' - \mathbf{q}) \\ &= \frac{i}{2k}(\mathbf{r} - \mathbf{q}) \end{aligned} \tag{3.15}$$

Under the conditions that the observation point $\mathbf{r}$ lies inside the source triangle S', equations (3.14) and (3.15) can be used to approximate the integrals I_1, $\mathbf{I}_2$ in (3.9) and (3.10). By analyzing the residual parts on a smooth surface, the normal component of $\mathbf{I}_3$ and the tangential component of $\mathbf{I}_4$ can be found to be:

$$\mp \frac{1}{2}\hat{n} \quad \text{and} \quad \mp \frac{1}{2}\hat{n} \times (\mathbf{r} - \mathbf{q}) \tag{3.16}$$

When $\mathbf{r}$ is on the side which $\hat{n}$ is pointing to, the negative sign is chosen; otherwise, the positive sign is chosen.

Although this method is simple, there are some obvious drawbacks. First, the observation point $\mathbf{r}$ has to be chosen on the triangle. Second, the imaginary part of the wave number must be very large. This is not the general case for our problem.

However, this method provides some insight regarding the integrals for conductive materials. If $\mathbf{r}$ resides on the source plane, as the conductivity increases, the integral of the forms (3.9)–(3.12) should converge to (3.14)–(3.16). In other words, (3.14)–(3.16) are the major contributions to the

integrals for conductive materials.

3.2.2.3 Line Integral Method

A line integral result [50] was derived to evaluate the integrals in (3.9)–(3.12). This method turns out to be efficient and accurate for both lossless and lossy media. In this method, the surface integral is converted into three line integrals by coordinate transformations, as derived in [50]. Therefore, this method is denoted as the line integral method.

However, there are still some singularities in the expression of the line integrals, which affect the accuracy of the numerical integration. Also it is not very clear why it is especially useful for integrals of Green's function in lossy media.

3.2.2.4 Modified Integral Method

The line integral method can be further simplified to remove the singularities. As a result, the convergence of the numerical integration is accelerated and the method becomes more efficient. Meanwhile, after the modifications, it captures the results in the circle approximation method. The terms in (3.14)–(3.16) can be extracted. Some extra terms, which act as the corrections to eqrefeq::approx1–(3.16), can be evaluated numerically using the quadrature rules. For (3.9), there is a simple expression, as derived in the Appendix A:

$$I_1 = \frac{i}{4\pi k}\left(I_0 - I_\alpha\right) \tag{3.17}$$

where

$$I_0 = \sum_{i=1,h_i\neq 0}^{3} \int_{\theta_i^-}^{\theta_i^+} d\theta e^{ikd} \tag{3.18}$$

$$I_\alpha = \sum_{i=1,h_i\neq 0}^{3} \int_{\theta_i^-}^{\theta_i^+} d\theta e^{ikR(\theta)} \tag{3.19}$$

Defining some intermediate integrals, such as $\mathbf{I}_\beta$, $\mathbf{I}_\perp$ and $\mathbf{I}_\parallel$, we can re-write (3.10)–(3.12) as:

$$\mathbf{I}_2 = (\mathbf{r}_0 - \mathbf{q})I_1 + \frac{1}{4\pi}\mathbf{I}_\beta \tag{3.20}$$

$$\mathbf{I}_3 = \frac{1}{4\pi}\left(\mathbf{I}_\perp - \mathbf{I}_\parallel\right) \tag{3.21}$$

$$\mathbf{I}_4 = \frac{1}{4\pi}\mathbf{I}_\perp \times (\mathbf{r}_0 - \mathbf{q}) + \frac{1}{4\pi}(\mathbf{r} - \mathbf{q}) \times \mathbf{I}_\parallel \tag{3.22}$$

where $\mathbf{I}_\beta$, $\mathbf{I}_\perp$ and $\mathbf{I}_\parallel$ are defined as:

$$\mathbf{I}_\beta = \int_{S'} d\mathbf{r}' \frac{e^{ikR}}{R}\boldsymbol{\rho}(\mathbf{r}') \tag{3.23}$$

$$\mathbf{I}_\perp = \mathbf{d}\int_{S'} d\mathbf{r}' \frac{ikR - 1}{R^3}e^{ikR} \tag{3.24}$$

$$\mathbf{I}_\parallel = \int_{S'} d\mathbf{r}' \frac{ikR - 1}{R^3}e^{ikR}\boldsymbol{\rho}(\mathbf{r}') \tag{3.25}$$

$$\boldsymbol{\rho}(\mathbf{r}') = \mathbf{r}' - \mathbf{r}_0, \qquad \mathbf{d} = \mathbf{r} - \mathbf{r}_0 = \pm d\hat{n} \tag{3.26}$$

where $\mathbf{r}_0$ is the projection of $\mathbf{r}$ on the source triangle.

First, in this modified method, some singularities, which appear in the original line integral method, are removed. For example, in [50], I_α is written as:

$$I_\alpha = \sum_{i=1}^{3}\int_{x_i^-}^{x_i^+} dx \frac{h_i}{h_i^2 + x^2}e^{ik\sqrt{h_i^2+d^2+x^2}} \tag{3.27}$$

When $h_i \to 0$, there is a singularity in the integrand. Then the integrand is no longer a smooth function and numerical integration could be problematic. After transforming the integration from x in (3.27) to the angular integral in (3.19), the singularity is removed.

A comparison of the convergence using different number of quadrature points in the line integral method and modified method is shown in Figure 3.1. We can observe that using the modified integral method, the values of the integral converge faster and therefore fewer quadrature points are required, especially when one of the h_i is small. This is because the singularity in (3.27) is removed in (3.19).

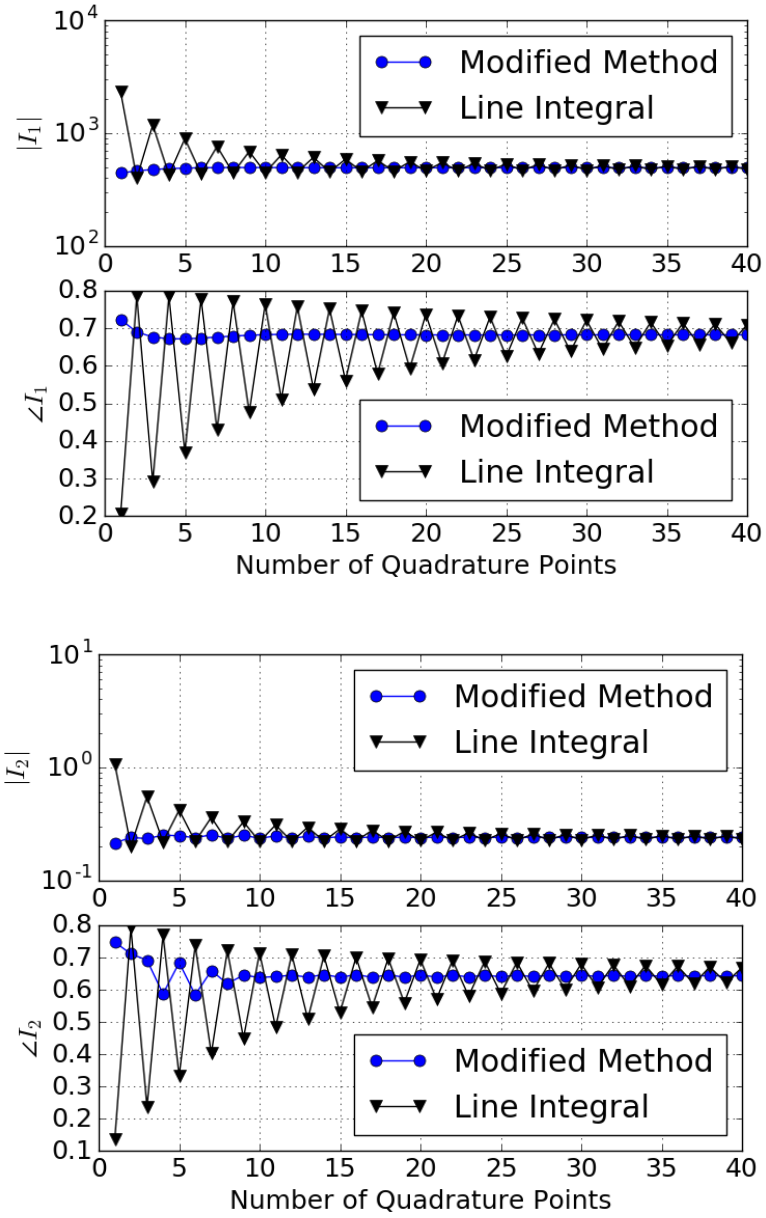

Figure 3.1: The results of I_1 and $\mathbf{I}_2$ evaluated with different number of quadrature points. In this example, the coordinates (in mm) of the triangle vertices are $(0,0,0)$, $(0,1,0)$ and $(1,0,0)$. The coordinates (in mm) of the observation point $\mathbf{r}$ are $(0.49,0.5,0.0)$. The conductivity is 10^6 S/m and the frequency is 30 MHz. Top: the amplitude and phase of I_1. Bottom: the amplitude and phase of the y component of $\mathbf{I}_2$.

Second, the results can be reduced to those of the circle approximation method. Note that I_0 can be simplified to be a constant, depending on the location of the projection point $\mathbf{r}_0$.

- If $\mathbf{r}_0$ is inside the triangle, $I_0 = 2\pi e^{ikd}$.
- If $\mathbf{r}_0$ is on the boundary of the triangle, $I_0 = \pi e^{ikd}$.
- If $\mathbf{r}_0$ is outside the triangle, $I_0 = 0$.

When k'' becomes very large, the integrals (3.19) and (3.23) (see (A.17) in Appendix A) reduce to zero. Then $I_1 = \frac{i}{4\pi k} I_0$ and $\mathbf{I}_2 = \frac{i}{4\pi k} I_0(\mathbf{r_0} - \mathbf{q})$, which are equivalent to (3.14) and (3.15) by assuming $d = 0$ and $\mathbf{r}_0$ on the triangle, i.e. $I_0 = 2\pi$. Similarly, (3.25) (see (A.19) in Appendix A) and the first term in (A.8) are reduced to zero, leaving $\mathbf{I}_3 = \mp\frac{1}{4\pi} I_0 \hat{n}$ and $\mathbf{I}_4 = \mp\frac{1}{4\pi} I_0 \hat{n} \times (\mathbf{r}_0 - \mathbf{q})$, which are equivalent to (3.16). Therefore, the above integrals of I_1, $\mathbf{I}_2$, $\mathbf{I}_3$ and $\mathbf{I}_4$ are reduced to the results of the circle approximation method, if the observation point $\mathbf{r}$ resides on the triangle ($d = 0$ and $\mathbf{r} = \mathbf{r}_0$) and the material is very lossy ($k'' \to \infty$).

To validate the accuracy of the methods, we compare the amplitudes of I_a using different methods, as shown in Figure 3.2. For low frequencies, k'' is small, the singularity subtraction can be used as the benchmark. The results of the modified method match well with those of the singularity subtraction, as well as those of the quadrature points methods. The circle approximation method becomes inaccurate since it is only valid for large k''. As the frequency and k'' increase, the circle approximation can be used as the benchmark. The results of the modified method match well with those of the circle approximation method for $k''h > 10$, and the singularity subtraction method becomes inaccurate in such a regime. For extremely large k'', the results using the quadratures start to deviate from the correct results, as the number of quadrature point decreases. This is due to the difficulties to capture the I_0 term using numerical integration. Therefore, from low to high k'', the modified method always gives rise to the accurate results.

In summary, we proposed a robust and accurate method to calculate the integrals in the method of moments. The singularity is removed from the original line integral method to improve the accuracy and it can be seen that this method is equivalent to the simple circle approximation for highly lossy materials. This method is especially suitable for conductor problems, since it captures the losses well and converges faster than the line integral method.

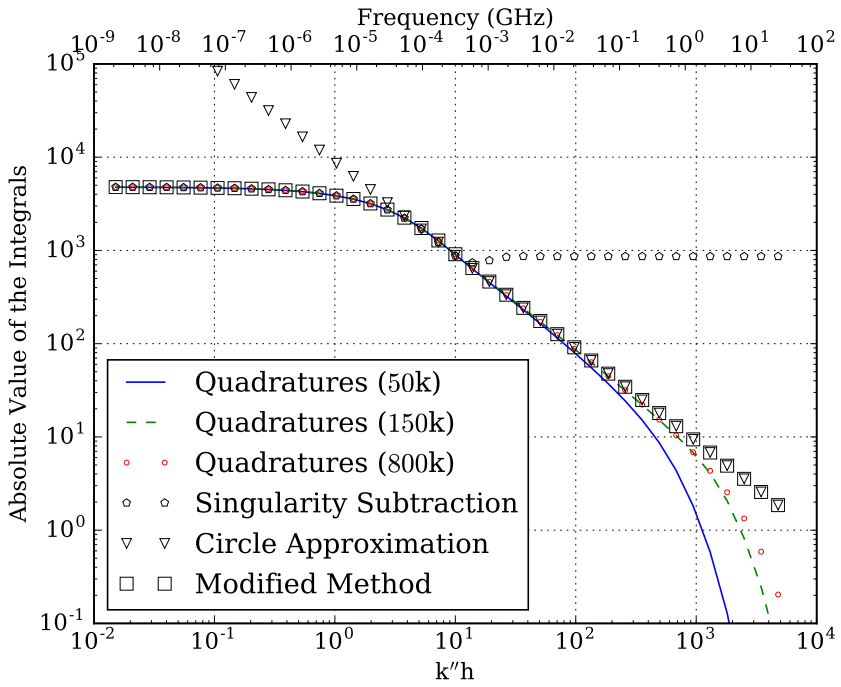

Figure 3.2: A comparison of the amplitude of I_a using different methods: integrating using 50, 150 and 800 thousand quadrature points, the singularity subtraction method, the circle approximation method, and the modified integral method with ten quadratures. The medium is copper with $\sigma = 5.8 \times 10^7$ S/m. The frequency is swept from DC to 40 GHz.

3.2.3 PEC and IBC Approximations

As a general method for dielectrics and conductors, this method will converge to the AEFIE for PEC [14] if the conductivity is infinite. This can be easily seen from the equations for the matrix elements in (3.2)–(3.5) for the internal region: If $\sigma \to \infty$, then $k' \to \infty$ and $k'' \to \infty$, the matrix element for $\overline{\mathbf{V}}$, $\overline{\mathbf{K}}$, and $\overline{\mathbf{P}}$ are reduced to zeros, leaving only the identity matrix blocks. Since the identity matrix block is non-singular, the magnetic current should always be zero. Then (3.1) is reduced to the AEFIE equation for PEC.

When the conductivity is extremely large, but still finite, the formulation can be reduced to an IBC formulation. For materials with large conductivities, the circle approximation will give a good approximation of the matrix element in (3.1) for the internal problem. The off-diagonal matrix elements in $\overline{\mathbf{V}}$, $\overline{\mathbf{K}}$, and $\overline{\mathbf{P}}$ can be assumed to be zero due to the loss of the Green's

function. Therefore,

$$\left[\overline{\mathbf{V}}_{int}\right]_{mm} \approx \mu_r \frac{i}{2k} \langle \mathbf{T}_m, \mathbf{\Lambda}_m^J \rangle \tag{3.28}$$

$$\left[\hat{n} \times \overline{\mathbf{I}}\right]_{mm} \approx \langle \mathbf{T}_m, \hat{n} \times \mathbf{\Lambda}_m^M \rangle \tag{3.29}$$

$$\left[\overline{\mathbf{P}}_{int}\right]_{mm} \approx \epsilon_r^{-1} \frac{i}{2k} \langle \nabla \cdot \mathbf{T}_m, \nabla \cdot \mathbf{\Lambda}_m^J \rangle \tag{3.30}$$

$$\left[\overline{\mathbf{K}}_{int}\right]_{mm} = 0 \tag{3.31}$$

where

$$\langle f, g \rangle = \int_S d\mathbf{r} f(\mathbf{r}) \cdot g(\mathbf{r}) \tag{3.32}$$

Noticing that $\epsilon_r = \frac{k^2}{k_0^2}$ and k has large real and imaginary parts in the conductor, we can conclude that $\left[\overline{\mathbf{V}}_{int}\right]_{mm} \gg \left[\overline{\mathbf{P}}_{int}\right]_{mm}$. Therefore, by assuming $\mu_r = 1$, the second equation in (3.1) becomes:

$$\langle \mathbf{T}_m, \frac{i}{k} \cdot ik_0 \mathbf{J} + \hat{n} \times \frac{1}{\eta_0} \mathbf{M} \rangle = 0 \tag{3.33}$$

This equation is equivalent to the simple expression of IBC:

$$\eta \mathbf{J} = \hat{n} \times \mathbf{M} \tag{3.34}$$

The above discussions reveal that the proposed method can be regarded as a generalized impedance boundary condition method [50, 56]. When the conductivity is extremely large, the formulation is reduced to the IBC formulation similar to [46], where dual basis functions are used to represent the electric and magnetic currents. As the conductivity decreases, the coupling between the electric and magnetic current becomes global, as the matrices for the internal problem become denser.

3.3 Numerical Results

In this section, we first validate the results using two simple examples: a scattering problem with far field compared to the Mie series, and a skin depth simulation in a simple transmission line problem. Then by adopting a suitable fast solver and a pre-conditioner, this method is used to simulate

complex circuit structures.

3.3.1 Validation

3.3.1.1 Scattering of a Conducting Sphere

A 1 m sphere with $\epsilon_r = 1.5$ and $\mu_r = 1$ is illuminated by a plane wave at 200 MHz. The average size of mesh elements is $h = 0.11$ m. In order to validate the accuracy of the proposed method from dielectrics to conductors, we choose a few values of conductivity: $\sigma = 10^3$ S/m (skin depth $\delta_s \approx 0.001$ m), $\sigma = 10$ S/m ($\delta_s \approx 0.011$ m), $\sigma = 0.1$ S/m ($\delta_s \approx 0.12$ m), $\sigma = 0.01$ S/m ($\delta_s \approx 0.68$ m), and $\sigma = 0.001$ S/m ($\delta_s \approx 6.5$ m). The far field is calculated and compared to the Mie series. As shown in the first figure in Figure 3.3, all the simulation results match well with the Mie series from fully penetrable regime ($\sigma = 0.001$ S/m) to nearly the PEC regime ($\sigma = 10^3$ S/m). For $\sigma > 10^3$ S/m, the RCS curves will be very similar to the PEC curve. To compared with the IBC solutions, the far field for these conductivities are calculated using IBC Mie series. As shown in the second figure in Figure 3.3, the IBC solution starts to deviate from the Mie series if $\sigma < 0.1$ S/m (or $\delta_s > h$). This can be obviously seen from the plots of $\sigma = 0.01$ S/m and $\sigma = 0.001$ S/m. This example validates the accuracy of the far field calculations for the dielectric to conductive objects using the proposed method.

3.3.1.2 Skin Depth in a Transmission Line

A simple transmission line model with circular cross-sections is excited by a delta-gap source at the port, as in Figure 3.4. The conductivity of the material is set to be $\sigma = 10^7$ S/m. Assuming that the electric current flowing inside the conductor is proportional to the electric field, we can visualize the skin depth inside the conductor. The electric field at the cross section with $x = 50$ μm is evaluated at different frequencies. As can be seen from Figure 3.4, at 0.8 GHz the current is fully developed inside the conductors, while as frequency increases to 6 GHz, the current concentrates near the surface of the conductor. The observed skin depth roughly agrees with the calculated skin depth on a planar surface. But the observed skin depth is

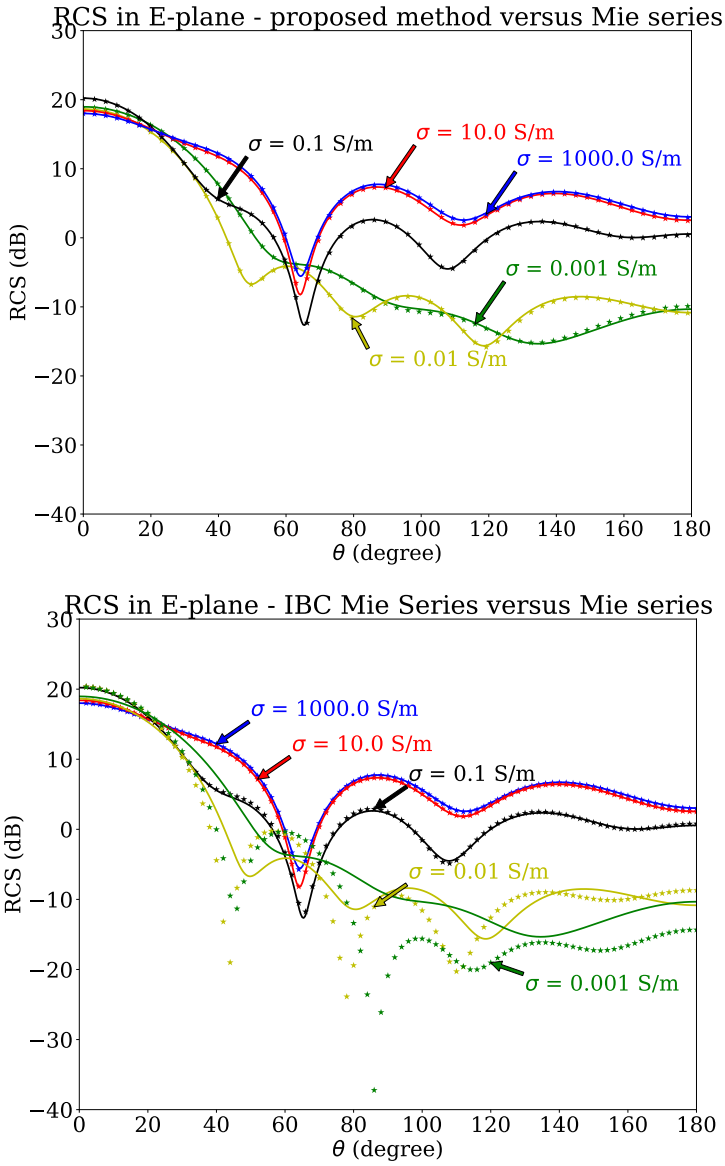

Figure 3.3: The radar cross section (RCS) in electric field planes for different conductivities using the proposed method and the IBC Mie series. The solid lines represent the Mie series and the dots represent the simulated field and the IBC Mie series. The different colors of lines and dots represent the different conductivities used for the simulations.

slightly larger than the calculation. For example, the observed skin depth is 2.35 μm and the calculated skin depth on a planar surface is 2.05 μm. These differences are due to the geometry effects.

3.3.2 Large-Scale Simulations

In order to solve large and complex problems using this method, a multipole based fast algorithm [57, 58, 59, 60] can be used to accelerate the matrix vector product. Since the problems we are interested in are mid-size structures with some fine details (small element sizes compared to the wavelength), the fast algorithm needs to be accurate and robust for such cases. Therefore, we choose to use the mixed-form fast multipole algorithm (FMA) [32]. In this method, the multipoles are used to expand waves at lower level (smaller boxes), and the plane waves are used to expand waves at higher level (boxes size larger than 0.15 wavelength). A transition between the two can be performed efficiently as the box size reaches a critical point. For the internal problem, due to the high conductivities of the examples, only the near interactions of the elements are needed and FMA is not in use. This is because the Green's function decays exponentially with $e^{-k''R}$. Then the errors for dropping the far interaction contributions can be bounded by controlling the leafy level box size in FMA for a large $k''d$, where d denotes the leafy level box size. A systematic consideration can be found in [61]. Therefore, sparse matrices are sufficient to store these matrix elements. These matrix elements can be calculated accurately using the modified method proposed in this chapter. Otherwise, large errors in the matrix elements will give rise to failure to convergence or meaningless results.

Moreover, a pre-conditioner is used for the simulations. The form of the pre-conditioner matrix is the same as that for the dielectrics in [52]. It has been shown that the pre-conditioner accelerates the convergence greatly for dielectrics. In the case of lossy media, the matrices for the internal problem can be regarded as a sparse version of dielectrics, since the Green's function decays out quickly at large distances. As a saddle point problem [36, 37], similar to the problem in [52], this problem can be accelerated with the same form of the pre-conditioner.

With these techniques, we can simulate complex circuit structures. Three

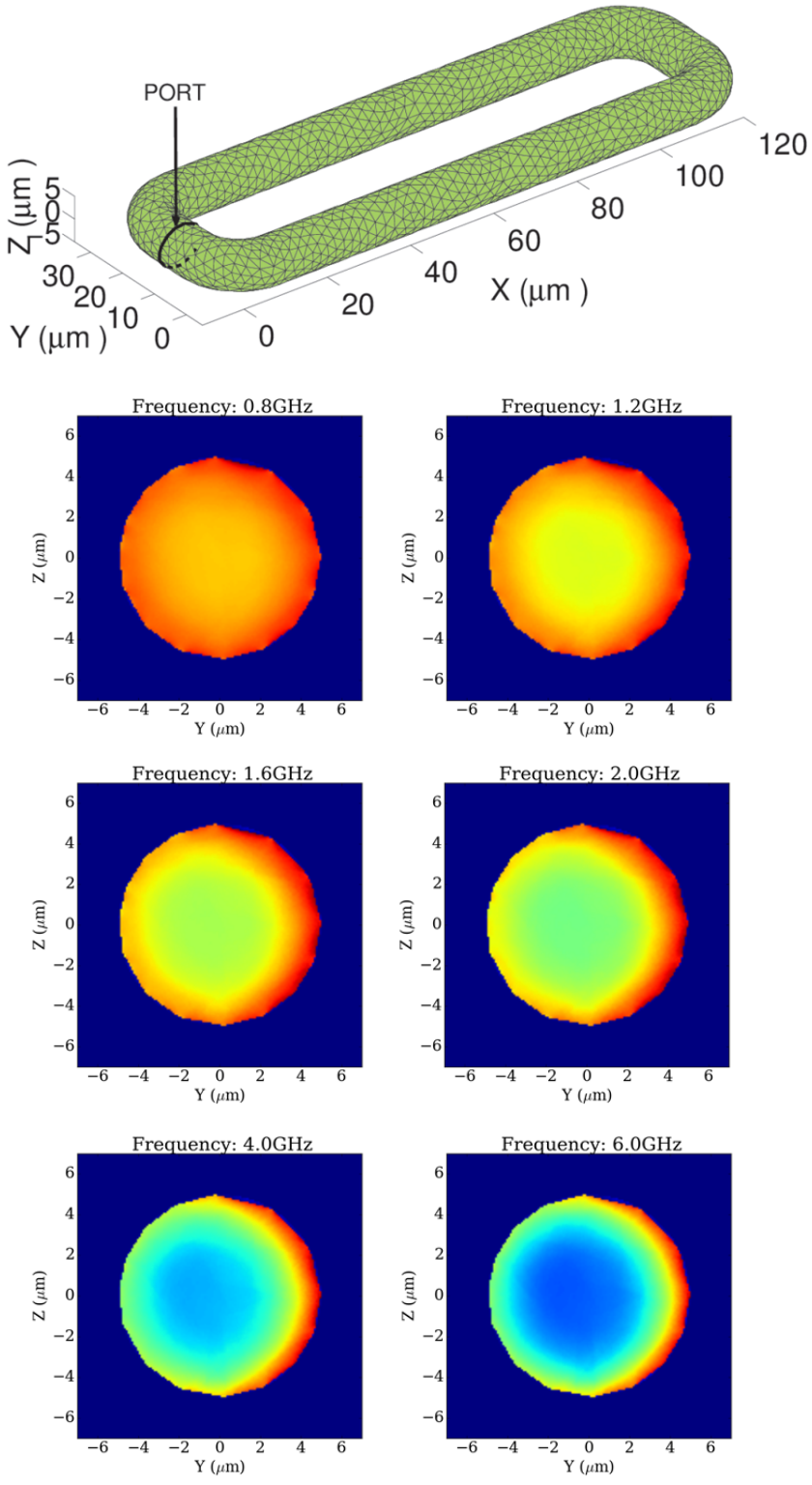

Figure 3.4: Simulation results of a transmission line (TL). Top: the TL model with a excitation port. Bottom: the normalized current flowing at the cross section of the TL at different frequencies showing skin effects.

of these structures, from simpler to more complex, are presented in this section.

3.3.2.1 Two-Layer Circuit Board I

A two-layer circuit board, with a differential trace and ground pads connected to a ground plane by vias, is simulated, as in Figure 3.5. The metal layers are assumed to be copper ($\sigma = 5.8 \times 10^7$ S/m). The background is assumed to have a relative permittivity of 3.4 and a loss tangent of 0.02. Each layer of copper is 15 μm thick and the distance between the copper layers is about 30 μm. The total number of unknowns of the structure is about 83,000. The circuit is excited by a delta-gap source at the ports from 1 GHz to 36 GHz. Then the scattering matrix can be found for this frequency range. The scattering parameters S_{12} at these frequencies are plotted in Figure 3.5.

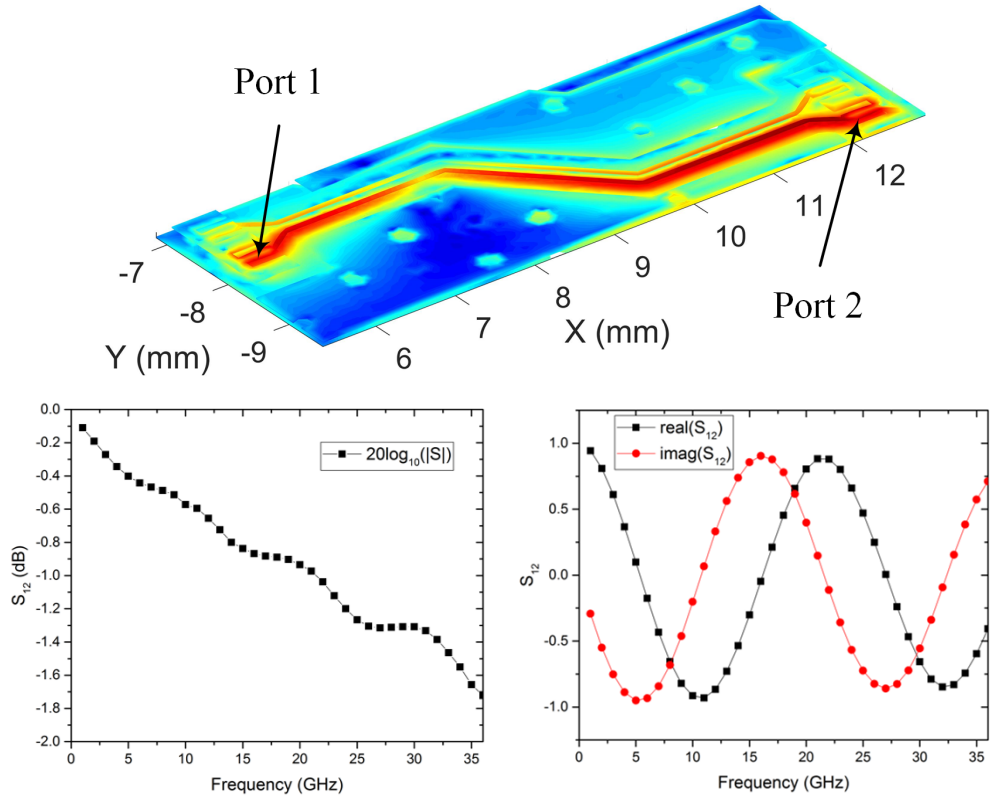

Figure 3.5: Simulation results of the circuit board I. Top: the current distribution at 8 GHz. Middle: scattering parameters S_{12} in dB. Bottom: the real and imaginary parts of the scattering parameters S_{12}.

3.3.2.2 Two-Layer Circuit Board II

Another more complex two-layer circuit board, similar to circuit board I but larger in size, is simulated as shown in Figure 3.6. The metal and background materials are the same as those for circuit board I. The thickness of the metal layers and the distance between the layers are also the same as for circuit board I. The scattering parameters S_{12} are plotted from 1 GHz to 12 GHz. The total number of unknowns is around 480,000.

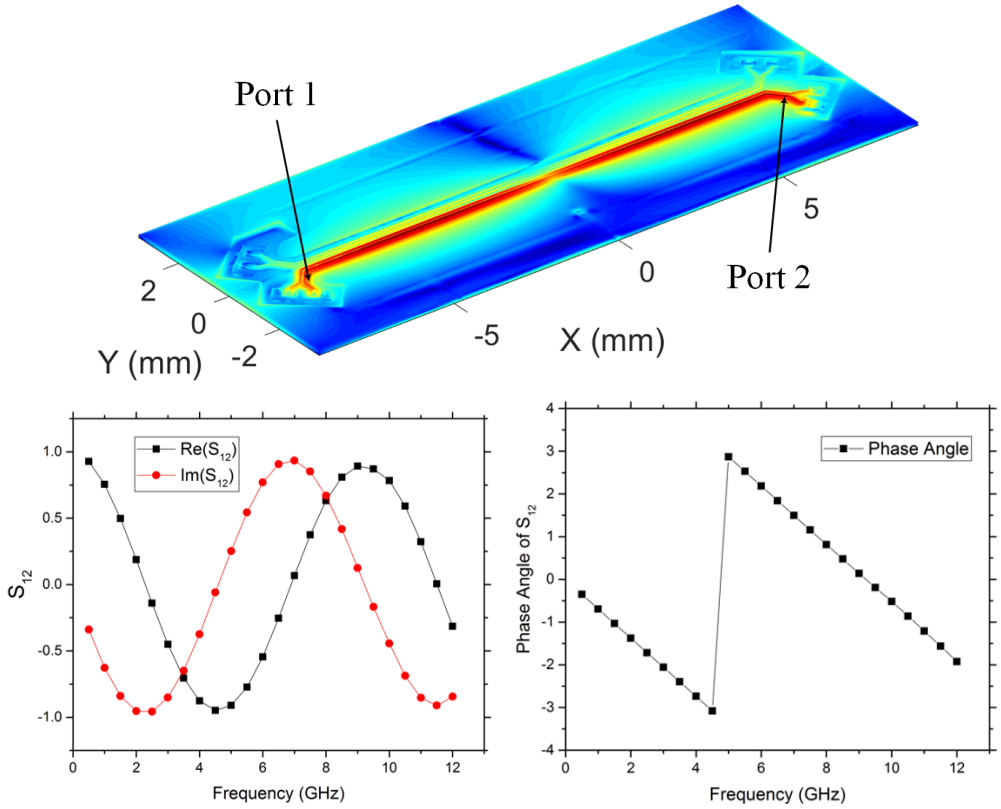

Figure 3.6: Simulation results of the circuit board II. Top: the current distribution at 10 GHz. Middle: the real and imaginary parts of the scattering parameters S_{12}. Bottom: the phase of the scattering parameters S_{12}.

3.3.2.3 Four-Layer Circuit Board III

In the last part, we demonstrate a larger and more complex example, with over 2 million unknowns and a lot of fine details, as shown in Figure 3.7. Each layer is still assumed to be copper, and the background material is the same as that in the circuit boards I and II. The top two layers and the

bottom two layers are close to each other (with 30 μm gap). But as typical for organic package substrates, there is a large gap (about 750 μm) between the top and bottom parts. A current distribution at 2 GHz of the simulation is shown in Figure 3.7. In this case, the iterative solver requires 130 steps to converge to the solution with a tolerance of 10^{-2}.

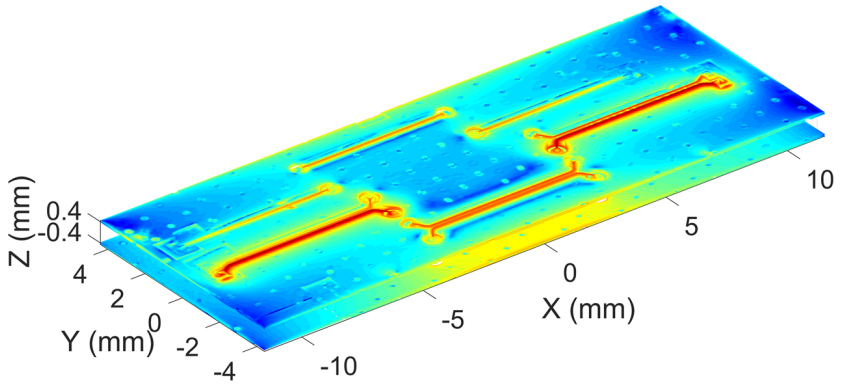

Figure 3.7: The current distribution of the circuit board III at 2 GHz.

The above three examples demonstrate the usage of this method to solve multi-scale problems with a large number of unknowns. In the demonstrated examples, the fine details in the structures are much smaller than the wavelength while the size of the geometry is comparable to the wavelength. By using the proposed method, the multi-scale nature of the problem is well addressed by the use of the mixed-form FMA and the proposed pre-conditioner. Therefore, such problems with a large number of unknowns can be efficiently solved using this method.

3.4 Conclusion

In this chapter, we demonstrate a generalization of the AEFIE for dielectrics for solving lossy conductor problems. We proposed a novel and accurate way to evaluate the integrals of Green's function in lossy media. This approach is motivated by the simple circle approximation. It is shown that the proposed method is equivalent to the IBC approximation if the electric and magnetic current are only locally coupled. Therefore, it can be regarded as a generalized impedance boundary condition method. Finally, some simple

numerical examples are first demonstrated to validate the accuracy of the method. Then some circuit structures are simulated as a demonstration of the capability of the method for large and complex models.

Chapter 4

A Broadband Multilevel Fast Multipole Method Using Plane Wave and Multipole Hybridization

4.1 Introduction

The fast multipole algorithm (FMA) has been extensively studied for more than twenty years since its first application in the calculations of the Coulomb interactions between charged particles [62, 63]. Later this method was extended to solving the Helmholtz equation in electrodynamic problems [64] and solving the scattering problem using the integral equation [65, 66]. One of the most important applications of FMA is to accelerate the matrix-vector products in the integral equation formulations for electromagnetic (EM) problems in a multilevel manner [67, 68, 59]. The complexity can be reduced, for example in the surface integral equation (SIE), from $O(N^2)$ to $O(N)$ in static and quasi-static cases and to $O(N \log N)$ in dynamic cases [57].

The acceleration by FMA is so remarkable that it has aroused plenty of interests in improving the efficiencies and the accuracies in broadband applications. To achieve this goal, three kinds of expansions of the Green's function were proposed under the framework of the FMA: the multipole expansion, the plane wave expansion and the exponential expansion (also known as the inhomogeneous plane wave expansion or the spectral representation). The precursory work [63] was based on the multipole expansion, in which the translation matrices are dense. The technique of "point-and-shoot" can be applied to reduce the dense matrices into sparse ones. This approach is particularly efficient and accurate for static and quasi-static EM problems and this method is also known as the low-frequency FMA (LF-FMA) or the dense FMA. For electrodynamic problems, the plane wave expansion was later introduced in [64] and succinctly re-derived in [69] to diagonalize the translation matrices. The efficiency was further improved by successfully applying

the Lagrange interpolation [70], which allows for more efficient samplings at different levels in MLFMA. Other interpolation methods based on the fast Fourier transform were also studied [71]. This class of FMA schemes is also known as the mid-frequency FMA or the diagonal FMA. In the exponential expansion, the Green's function is explicitly split into the propagating and evanescent spectra [72]. However, the convergence to the Green's function is highly directional, especially at low frequencies. At wave-physics frequencies, a steepest descent path for the integrations can be found to achieve an optimal convergence. This approach is termed the fast inhomogeneous plane wave algorithm (FIPWA) [73]. At low frequencies, one can separately consider six translation directions [74] or design a complex integral path to capture the deep evanescent wave accurately [75].

The multipole expansion is inefficient at high frequencies since the translation matrices are dense and a large number of harmonics is required. The plane wave expansion, on the other hand, suffers from the low-frequency breakdown due to its failure to capture the evanescent waves. The exponential expansion also requires different treatments at different frequency regimes. The emerging multi-scale problems [14, 76, 52, 77, 78] call for a broadband FMA with good accuracies.

A mixed-form FMA was proposed in [32] for broadband simulations. The multipole expansion is used at the low-frequency regime and the plane wave expansion is used at the higher-frequency regime. A transformer is employed to convert between the multipole and the plane wave expansions. An accuracy level of 10^{-2} can be achieved using a small number of harmonics. Recently, an enhanced mixed-form FMA with the rotation technique was proposed to improve the accuracy in the transformation region [79]. Such a treatment makes the algorithm error controllable in broadband applications.

Another broadband FMA with a new mixed form was proposed in [80]. This method uses the multipole expansion at extremely low frequencies, the exponential expansion at middle frequencies, and the plane wave expansion at higher frequencies. High accuracy can be achieved at all frequencies using this scheme.

A non-directional plane wave algorithm was then proposed [81]. The conventional plane-wave expansion was studied first in $\hat{z}$ direction and an optimal integral path was found to make it low-frequency stable. Then a QR-based method was applied to allow translations in other directions. High accuracy

can be achieved and the direction dependence issue was eliminated compared to exponential expansions.

In a recent work, a broadband MLFMA based on the approximated diagonalization of the Green's function was proposed [82]. The formula is based on the plane wave expansion with the approximations of the Bessel function and the Hankel function of the first kind. Using this method, an accuracy of 10^{-2} can be achieved at low frequencies.

In this chapter, we propose a novel hybrid FMA. As opposed to using different expansions at different frequency regimes, the multipole and the plane wave expansions are used simultaneously. The plane wave expansion factorized the low-order harmonics and the multipole expansion captures the high-order harmonics to better control the accuracy. The rotation technique is then used to improve the efficiency in the multipole expansion. At low frequencies, the number of harmonics represented by the plane wave has to be small and well controlled to avoid the low-frequency breakdown. As the frequency increases, the number of plane wave harmonics increases, and this method will eventually reduce to the conventional diagonal FMA at higher frequencies. The algorithm is therefore stable at all frequencies. The error can be controlled up to 10^{-8} and the method is particularly useful when high accuracies are required.

The chapter is organized as follows: in Section 4.2, we review the necessary background of the dense FMA and the diagonal FMA, followed by the formulation of the proposed hybrid FMA. The error analysis is performed to control the accuracy and the rotation technique is briefly introduced for efficiency improvements. In Section 4.3, we present the simulation errors of the algorithm for the worst cases and some general application cases. Then the algorithm is applied to an integral equation formulation to solve EM scattering problems at a very low frequency and a higher frequency for numerical validations. We finally draw a conclusion in Section 4.4.

4.2 Methods

In this section, we propose the formulation for the hybrid FMA. Brief reviews of the diagonal plane wave expansion and the dense multipole expansion are given, followed by the derivations of the proposed method and some

numerical details.

4.2.1 Reviews of the Conventional FMA

In this section, we briefly review the diagonal FMA using plane waves and the dense FMA using multipoles. The reviews and the discussions will motivate the novel hybridization scheme in this chapter.

4.2.1.1 The Diagonal FMA Using Plane Waves

The diagonal FMA utilizes the addition theorem, in which the scalar Green's function is expressed as:

$$\frac{e^{ikr_{ij}}}{r_{ij}} = ik\sum_{l=0}^{\infty}(-1)^l(2l+1)j_l(kd)h_l^{(1)}(kr_{mn})P_l(\hat{d}\cdot\hat{r}_{mn}) \tag{4.1}$$

where the vectors are defined as: $\mathbf{r}_{ij} = \mathbf{r}_i - \mathbf{r}_j$, $\mathbf{d} = \mathbf{r}_{im} + \mathbf{r}_{nj}$ and $d < r_{mn}$. The functions j_l, $h_l^{(1)}$ and P_l are the spherical Bessel function, spherical Hankel function of the first kind and the Legendre polynomial of the order l respectively. The plane wave expansion is realized by using:

$$j_l(kd)P_l(\hat{d}\cdot\hat{r}_{mn}) = \frac{1}{4\pi i^l}\int d^2\hat{k}e^{i\mathbf{k}\cdot\mathbf{d}}P_l(\hat{k}\cdot\hat{r}_{mn}) \tag{4.2}$$

Truncating the summation in (4.1) to a finite number L and swapping the orders of the summation and the integral, the Green's function is approximated as:

$$\frac{e^{ikr_{ij}}}{r_{ij}} \approx ik\int d^2\hat{k}e^{i\mathbf{k}\cdot\mathbf{r}_{im}}\cdot\alpha(L^-,\mathbf{r}_{mn})\cdot e^{i\mathbf{k}\cdot\mathbf{r}_{nj}} \tag{4.3}$$

where

$$\alpha(L^-,\mathbf{r}_{mn}) = \frac{1}{4\pi}\sum_{l=0}^{L} i^l(2l+1)h_l^{(1)}(kr_{mn})P_l(\hat{k}\cdot\hat{r}_{mn}) \tag{4.4}$$

With the interpolation techniques [70, 71], a complexity of $\mathcal{O}(N\log N)$ can be achieved at mid frequencies.

The factorization of the Green's function in (4.3) becomes inaccurate at low frequencies due to two major reasons. First, as $k\to 0$, $h_l^{(1)}(kr_{mn}) \to (kr_{mn})^{-(l+1)}$. The higher-order terms swamp the contributions from the low-order terms in the summation in (4.4). Second, the plane wave representa-

tions of the spherical Bessel function in (4.2) becomes numerical unstable. This is because the integrand at the right-hand side of (4.2) is of the amplitude $\mathcal{O}(1)$, while at the left-hand side, $j_l(kd) \to (kd)^l$ and becomes exponentially small with respect to l at low frequencies. Cancellations at the right-hand side become increasingly difficult to converge to the small value at the left-hand side.

The failures at low frequencies in (4.3) can be physically interpreted as the difficulties in capturing the evanescent waves using the plane wave expansion. These evanescent waves, at low frequencies, are encapsulated largely in the higher-order terms at the right-hand side of (4.1). The higher-order terms become fast oscillatory in the angular direction since $P_l(\hat{d} \cdot \hat{r}_{mn})$ becomes more oscillatory for higher orders. Therefore they become faster decaying in the radial direction. However, the low-order terms, which captures most of the propagating waves, can still be represented by plane waves at low frequencies. In order to capture the evanescent waves accurately, the dense FMA can be used.

4.2.1.2 The Dense FMA Using Multipoles

The low-frequency-stable dense-matrix multipole expansions of the Green's function is [13]:

$$\frac{e^{ikr_{ij}}}{r_{ij}} = ik\boldsymbol{\beta}(\mathbf{r}_{ip}) \cdot \overline{\boldsymbol{\beta}}(\mathbf{r}_{pm}) \cdot \overline{\boldsymbol{\alpha}}(\mathbf{r}_{mn}) \cdot \overline{\boldsymbol{\beta}}(\mathbf{r}_{nq}) \cdot \boldsymbol{\beta}(\mathbf{r}_{qj}) \tag{4.5}$$

The right-hand side of (4.5), from right to left, reads radiation pattern $\boldsymbol{\beta}(\mathbf{r}_{qj})$, aggregation $\overline{\boldsymbol{\beta}}(\mathbf{r}_{nq})$, translation $\overline{\boldsymbol{\alpha}}(\mathbf{r}_{mn})$, disaggregation $\overline{\boldsymbol{\beta}}(\mathbf{r}_{pm})$ and receiving pattern $\boldsymbol{\beta}(\mathbf{r}_{ip})$. The matrix elements are indexed by the orders of the spherical harmonics $L = (l, m)$. The explicit expressions of the elements in $\overline{\boldsymbol{\beta}}$ and $\overline{\boldsymbol{\alpha}}$ are:

$$\beta_{L',L}(\mathbf{r}'') = \sum_{l''=|l-l'|}^{l+l'} 4\pi i^{(l'+l''-l)} \mathcal{A}_{L,L',L''} \cdot Y_{l'',m-m'}(\theta'', \phi'') j_{l''}(kr'') \tag{4.6}$$

$$\alpha_{L',L}(\mathbf{r}'') = \sum_{l''=|l-l'|}^{l+l'} 4\pi i^{(l'+l''-l)} \mathcal{A}_{L,L',L''} \cdot Y_{l'',m-m'}(\theta'', \phi'') h^{(1)}_{l''}(kr'') \tag{4.7}$$

where $\mathcal{A}_{L,L',L''}$ is the Gaunt coefficient, which is non-zero only when $l+l'+l''$ is even [33, pp. 591-596]. The radiation pattern is a column vector with $l = m = 0$ and the receiving pattern is a row vector with $l' = m' = 0$.

Equation (4.5) denotes a two-level FMA. It can be easily generalized to multilevel by further factorizing the radiation and receiving patterns:

$$\boldsymbol{\beta}(\mathbf{r}_{ip}) = \boldsymbol{\beta}(\mathbf{r}_{is}) \cdot \overline{\boldsymbol{\beta}}(\mathbf{r}_{sp}) \tag{4.8}$$

$$\boldsymbol{\beta}(\mathbf{r}_{qj}) = \overline{\boldsymbol{\beta}}(\mathbf{r}_{qt}) \cdot \boldsymbol{\beta}(\mathbf{r}_{tj}) \tag{4.9}$$

These factorizations will be useful in the multilevel generalizations of the hybrid scheme.

The dense FMA involves the products of dense matrices and vectors. It becomes computationally inefficient at high frequencies when the sizes of the matrices increase due to the needs of more multipole harmonics. The evanescent waves at low frequencies can be well captured by accurately calculating the high-order harmonics. Hence it can be used for the Green's function factorization with high accuracies.

4.2.2 A Review of the Diagonal FMA Using Inhomogeneous Plane Waves

To have a complete review of the conventional expansion of FMA, we will review the diagonal fast inhomogeneous plane wave algorithm (FIPWA). Since this method relies on the choices of the integration path, we will discuss the extensions of this method to a general complex wave number k in this section.

4.2.2.1 Derivation of the Fast Inhomogeneous Plane Wave Algorithm

In FIPWA, the Green's function is factorized with the plane waves by leveraging the Weyl identity [33]:

$$\frac{e^{ikr}}{r} = i \int_0^\infty dk_\rho \frac{k_\rho}{k_z} J_0(k_\rho \rho) e^{ik_z|z|} \tag{4.10}$$

where the Bessel function of 0-th order $J_0(k_\rho\rho)$ can be represented with plane waves in the cylindrical coordinate:

$$J_0(k_\rho\rho) = \frac{1}{2\pi}\int_0^{2\pi} d\phi e^{ik_\rho\rho\cos(\phi-\beta)} \tag{4.11}$$

and the angle β is arbitrary.

Plugging (4.11) into (4.10), the plane wave expansion of the Green's function is:

$$\frac{e^{ikr}}{r} = \frac{i}{2\pi}\int_0^{2\pi} d\phi \int_0^{\infty} dk_\rho \frac{k_\rho}{k_z} e^{ik_\rho\rho\cos(\phi-\beta)+ik_z|z|} \tag{4.12}$$

Apparently, for $z > 0$, the exponent of the integrand in (4.12) becomes $ik_\rho\rho\cos(\phi-\beta) + ik_z z = i\mathbf{k}\cdot\mathbf{r}$. The vector $\mathbf{k}$ is defined with the amplitude k and the angles in the spherical coordinate (θ, ϕ). The vector $\mathbf{r}$ is defined with the cylindrical coordinate vector $\boldsymbol{\rho} = (\rho, \beta)$ and z. The inner integral in (4.12) is over k_ρ, and it can be converted to an integral over complex angle γ with the following change of variables:

$$k_\rho = k\sin\gamma \qquad k_z = k\cos\gamma \tag{4.13}$$

Then the inhomogeneous plane wave expansion becomes:

$$\frac{e^{ikr}}{r} = \frac{ik}{2\pi}\int_0^{2\pi} d\phi \int_{\text{SIP}} d\gamma \sin\gamma e^{ik\rho\cos(\phi-\beta)\sin\gamma+ik|z|\cos\gamma} \tag{4.14}$$

The integration path of γ is the Sommerfeld integration path (SIP) determined by (4.13). The SIP depends on the amplitude and phase of k when k is complex. In Figure 4.1, the SIPs can be found for a fixed $|k|$ with varying phase angle of complex wave number k. The integral path parallel to the real axis captures the propagation waves and the integral path parallel to the imaginary axis captures the evanescent waves.

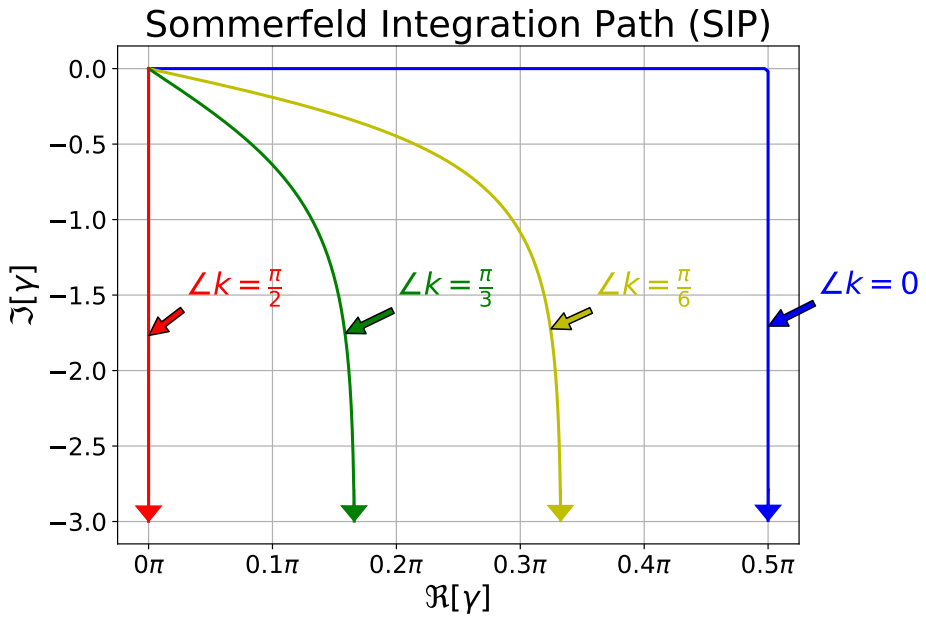

Figure 4.1: The SIPs for different angles of k with fixed amplitude $|k|$.

We define the integration of interest, the inner integral in (4.14), as:

$$I(\phi) = \int_{\text{SIP}} d\gamma \sin\gamma e^{ik\rho\cos(\phi-\beta)\sin\gamma + ik|z|\cos\gamma} \tag{4.15}$$

The convergence rate along SIP is slow. We need to find the steepest descent path (SDP) by studying:

$$I(\phi) = \int_{\text{SIP}} d\gamma f(\gamma) e^{h(\gamma)} \tag{4.16}$$

where

$$f(\gamma) = \sin\gamma \qquad h(\gamma) = ik(\rho\cos(\phi-\beta)\sin\gamma + |z|\cos\gamma) \tag{4.17}$$

The function $h(\gamma)$ is a phase of plane wave $\mathbf{k}$ in the direction of $\mathbf{r}$. The vector $\mathbf{k} = (k, \gamma, \phi)$ in the spherical coordinate, and $\mathbf{r} = (\rho, \beta, |z|)$ is the cylindrical coordinate:

$$i\mathbf{k}\cdot\mathbf{r} = i(k\sin\gamma\cos\phi, k\sin\gamma\sin\phi, k\cos\gamma)\cdot(\rho\cos\beta, \rho\sin\beta, |z|) = h(\gamma) \tag{4.18}$$

Since:

$$h(\gamma) = ikA\cos(\gamma - \gamma_0) \tag{4.19}$$

where:

$$A = \sqrt{\rho^2 \cos^2(\phi - \beta) + z^2} \qquad \gamma_0 = \tan^{-1}\left(\frac{\rho \cos(\phi - \beta)}{|z|}\right) \tag{4.20}$$

The stationary point of $h(\gamma)$ is γ_0 with $h'(\gamma_0) = 0$. The SDP requires:

$$\begin{cases} \Re\left[h(\gamma) - h(\gamma_0)\right] \leq 0 \\ \Im\left[h(\gamma) - h(\gamma_0)\right] = 0 \end{cases} \tag{4.21}$$

By letting $\gamma = \gamma_R + i\gamma_I$ and $k = k_R + ik_I$ for a general complex wave number:

$$\Re\left[h(\gamma) - h(\gamma_0)\right] = k_R \sin(\gamma_R - \gamma_0) \sinh\gamma_I - k_I \cos(\gamma_R - \gamma_0) \cosh\gamma_I + k_I \tag{4.22}$$

$$\Im\left[h(\gamma) - h(\gamma_0)\right] = k_R \cos(\gamma_R - \gamma_0) \cosh\gamma_I - k_I \sin(\gamma_R - \gamma_0) \sinh\gamma_I + k_R \tag{4.23}$$

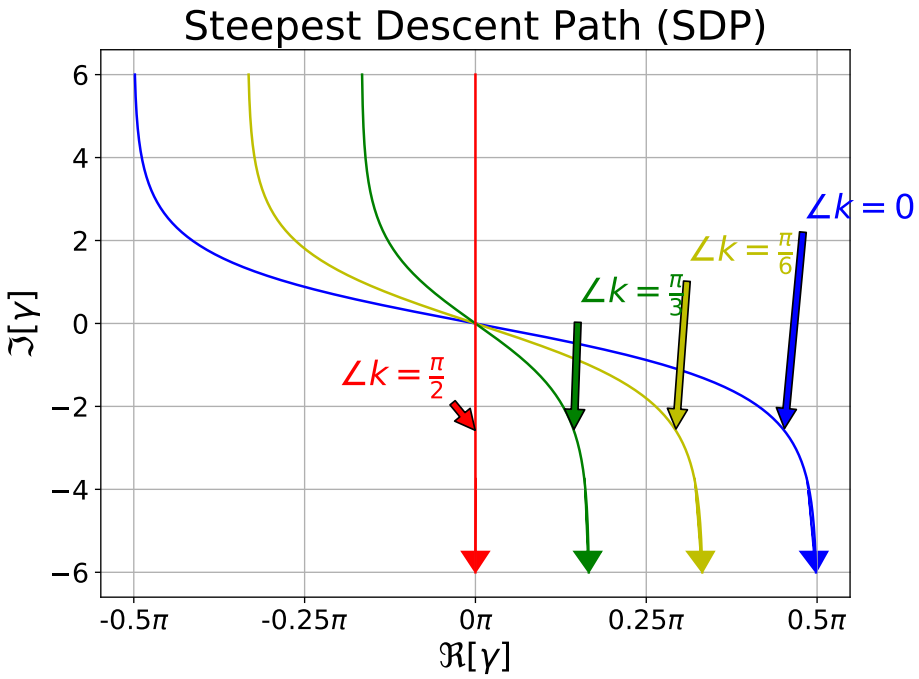

Figure 4.2: The SDPs for different angles of k with fixed amplitude $|k|$ and $\gamma_0 = \frac{\pi}{4}$.

According to (4.21) - (4.23), the SDPs for a general complex k can be found as in Figure 4.2. When $k_R \neq 0$ and $k_I = 0$, the SDP satisfies:

$$\cos(\gamma_R - \gamma_0) \cosh\gamma_I = 1 \tag{4.24}$$

When $k_R = 0$ and $k_I \neq 0$, the SDP satisfies:

$$\sin(\gamma_R - \gamma_0) \sinh \gamma_I = 0 \tag{4.25}$$

Along the path $\gamma_R = \gamma_0$,

$$\Re\left[h(\gamma) - h(\gamma_0)\right] = k_I(1 - \cosh \gamma_I) \leq 0 \tag{4.26}$$

which gives the SDP. Along the path $\gamma_I = 0$,

$$\Re\left[h(\gamma) - h(\gamma_0)\right] = k_I(1 - \cos(\gamma_R - \gamma_0)) \geq 0 \tag{4.27}$$

which gives the exponential growth path away from γ_0.

In order to convert the integral along SIP into an integral partially along the SDP, we change the integration path from the SDP to the modified-SDP (m-SDP) by adding the path along the real axis from 0 to γ_0 and taking the lower half of the SDP, as shown in Figure 4.3.

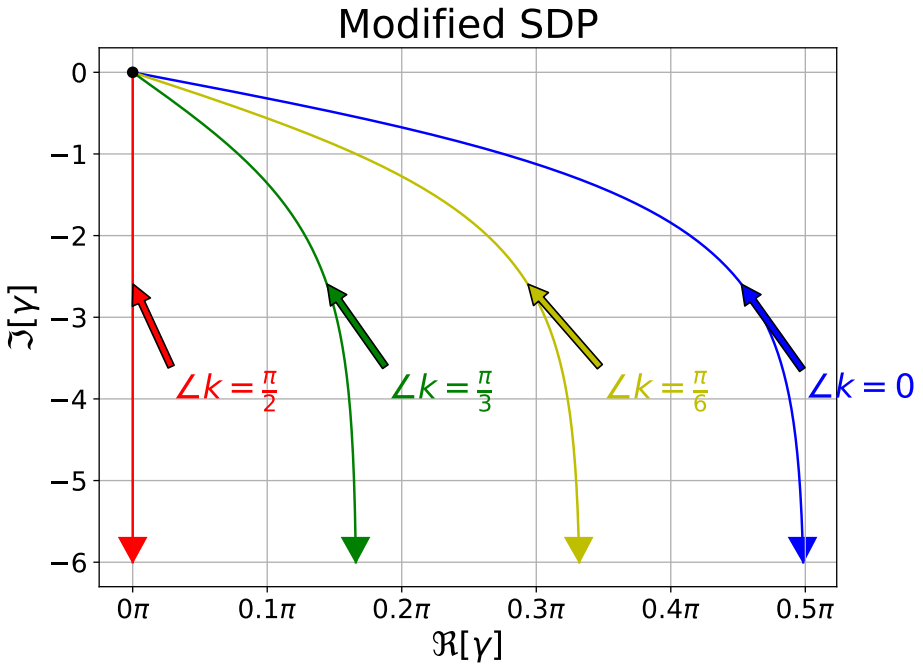

Figure 4.3: The modified SDPs (m-SDPs) for different angles of k with fixed amplitude $|k|$ and $\gamma_0 = 0$.

Then:

$$\int_{\text{SIP}} = \int_{\text{m-SDP}} \tag{4.28}$$

where

$$\text{m-SDP} = \Gamma_1 \bigcup \Gamma_2, \quad \Gamma_1 = [0, \gamma_0], \quad \Gamma_2 = [\gamma_0 - i0, \gamma_0 - i\infty] \tag{4.29}$$

The Green's function expansion becomes:

$$\frac{e^{-k_I r}}{r} = \frac{-k_I}{2\pi} \int_0^{2\pi} d\phi \int_{\text{m-SDP}} d\gamma \sin\gamma e^{h(\gamma)} \tag{4.30}$$

$$= \frac{-k_I}{2\pi} \int_0^{2\pi} d\phi I(\phi) \tag{4.31}$$

and

$$I(\phi) = I_1(\phi) + I_2(\phi) = \int_{\Gamma_1+\Gamma_2} d\gamma \sin\gamma e^{h(\gamma)} \tag{4.32}$$

where $h(\gamma) = -k_I A \cos(\gamma - \gamma_0)$ and

$$I_1(\phi) = \int_{\Gamma_1} \sin\gamma e^{h(\gamma)} = \int_0^{\gamma_0} d\gamma \sin\gamma e^{-k_I A \cos(\gamma - \gamma_0)} \tag{4.33}$$

$I_1(\phi)$ gives a real number.

$$I_2(\phi) = \int_{\Gamma_2} d\gamma \sin\gamma e^{h(\gamma)} \tag{4.34}$$

$$= -i \int_0^{+\infty} d\gamma_I \sin(\gamma_0 - i\gamma_I) e^{-k_I A \cosh\gamma_I} \tag{4.35}$$

$$= -\cos\gamma_0 \int_0^{\infty} d\gamma_I \sinh\gamma_I e^{-k_I A \cosh\gamma_I} \tag{4.36}$$

$$-i \sin\gamma_0 \int_0^{\infty} d\gamma_I \cosh\gamma_I e^{-k_I A \cosh\gamma_I} \tag{4.37}$$

One trick can be used for imaginary wave number: since the left-hand side of (4.31) is purely real, the right-hand side of (4.31) should be purely real. Therefore, the imaginary part of the ϕ integral of $I_2(\phi)$ should vanish, i.e.

$$\int_0^{2\pi} d\pi \sin\gamma_0 \int_0^{\infty} d\gamma_i \cosh\gamma_i e^{-k_I A \cosh\gamma_I} = 0 \tag{4.38}$$

Then

$$\int_0^{2\pi} d\phi \left(I_1(\phi) + I_2(\phi)\right) = \int_0^{2\pi} d\phi \left(I_1(\phi) + I_3(\phi)\right) \tag{4.39}$$

where

$$I_3(\phi) = \cos\gamma_0 \int_0^\infty d\gamma_I \sinh\gamma_I e^{-k_I A\cosh\gamma_I} = \cos\gamma_0 \int_0^\infty d\cosh\gamma_I e^{-k_I A\cosh\gamma_I} \tag{4.40}$$

Observing that the integrand of I_1 decays exponentially with a decay rate of $-k_I\cos(\gamma-\gamma_0)$, the evanescent depth is of the same order of $\frac{2\pi}{k_I}$. We call it the shallow evanescent wave. For I_2 and I_3, the decay rate is $-k_I\cosh\gamma_I$, which is much faster than that of I_1. We can call it the deep evanescent wave.

The numerical evaluation of I_1 is usually not a problem. However, I_3 is problematic for numerically evaluations: the infinite integral from $0\to\infty$ can be truncated to $0\to\gamma_t$ such that the remainder is small.

Since the remainder is:

$$\int_{\gamma_t}^\infty d\cosh\gamma_I e^{-k_I A\cosh\gamma_I} = \frac{e^{-k_I A\cosh t}}{k_I A} \tag{4.41}$$

Assuming $k_I A\sim k_I a$, γ_t can be determined with a given tolerance ϵ:

$$\gamma_t = \cosh^{-1}\left(-\frac{\log(k_I a)+\log\epsilon}{k_I a}\right) \tag{4.42}$$

when $k_I a$ is small, γ_t needs to be chosen large, while when $k_I a$ is large, γ_t may not even be required since the I_3 integral is smaller than ϵ.

Therefore the deep evanescent wave is difficult to evaluate for low-frequency problems. The unit-less parameter a is a function of the transition distance and the wavelength. In a typical FMM oct-tree structure, the value of a in a level will be doubled in its parent level. Therefore, the quadrature point of γ_I in (4.40) is difficult to choose.

The difficulties of choosing the quadrature points of γ is due to that the integrand in (4.14) is nonlinear function of γ.

Recall that in (4.11):

$$J_0(k\rho\sin\gamma) = \frac{1}{2\pi}\int_0^{2\pi} d\phi e^{ik\rho\sin\gamma\cos(\phi-\beta)} \tag{4.43}$$

where the angle β is arbitrary and can even be a function of γ. We can

change the variables, such that:

$$\beta = \phi_r + \beta' \tag{4.44}$$

With β' defined as:

$$\cos\beta' = \frac{1}{\sin\gamma} \qquad \sin\beta' = \frac{i\cos\gamma}{\sin\gamma} \tag{4.45}$$

Now β' is a complex number function of γ.

$$\sin\gamma\cos(\phi-\beta) = \cos(\phi-\phi_r) + i\sin(\phi-\beta)\cos\gamma \tag{4.46}$$

And (4.43) becomes:

$$J_0(k\rho\sin\gamma) = \frac{1}{2\pi}\int_0^{2\pi} d\phi e^{ik\rho\cos(\phi-\phi_r)-k\rho\sin(\phi-\phi_r)\cos\gamma} \tag{4.47}$$

With this new expression of $J_0(k\rho\sin\gamma)$, the Green's function can then be written as:

$$\frac{e^{ikr}}{r} = \frac{ik}{2\pi}\int_\Gamma d\gamma\sin\gamma\int_0^{2\pi} d\phi e^{ik\rho\cos(\phi-\phi_r)-k\rho\sin(\phi-\phi_r)\cos\gamma+ikz\cos\gamma} \tag{4.48}$$

We can define the ordinary vectors in Cartesian coordinate as:

$$\mathbf{k}_c = \begin{bmatrix} k\cos\phi \\ k\sin\phi \\ 0 \end{bmatrix} \qquad \boldsymbol{\rho}_c = \begin{bmatrix} \rho\cos\phi_r \\ \rho\sin\phi_r \\ 0 \end{bmatrix} \tag{4.49}$$

and

$$\mathbf{k}_e = \begin{bmatrix} ik\sin\phi \\ -ik\cos\phi \\ k \end{bmatrix} \qquad \mathbf{r} = \begin{bmatrix} \rho\cos\phi_r \\ \rho\sin\phi_r \\ z \end{bmatrix} \tag{4.50}$$

The expansion of the Green's function then becomes:

$$\frac{e^{ikr}}{r} = \frac{ik}{2\pi}\int_\Gamma d\gamma\sin\gamma\int_0^{2\pi} d\phi e^{i\mathbf{k_c}\cdot\boldsymbol{\rho}_c} e^{i\mathbf{k}_e\cdot\mathbf{r}\cos\gamma} \tag{4.51}$$

4.2.3 Formulation of the Hybrid FMA

From the discussions in Sections 4.2.1.1 and 4.2.1.2, it is clear that the diagonal plane wave expansion of FMA failed to capture the high-order harmonics at low frequencies and the dense multipole expansion is inefficient as the frequency increases. We proposed a novel hybrid scheme such that the low-order harmonics are factorized with the plane wave and the high-order harmonics are factorized with the multipole. By splitting the order l into two parts, the Green's function is then written as:

$$\frac{e^{ikr_{ij}}}{r_{ij}} \approx ik \sum_{l=0}^{L_0} I_l^{\text{pw}} + ik \sum_{l=L_0+1}^{L_m} I_l^{\text{mp}} \tag{4.52}$$

where "pw" stands for plane wave and "mp" stands for multipole. The plane wave contributions to the Green's function can be written in the same manner of (4.3):

$$\sum_{l=0}^{L_0} I_l^{\text{pw}} = ik \int d^2\hat{k} e^{i\mathbf{k}\cdot\mathbf{r}_{im}} \cdot \alpha(L_0, \mathbf{r}_{mn}) \cdot e^{i\mathbf{k}\cdot\mathbf{r}_{nj}} \tag{4.53}$$

The maximum order L_0 for the plane waves needs to be carefully determined so that the algorithm does not breakdown at low frequencies. The second term in (4.52) includes higher-order contributions up to the order L_m, which should be determined to bound the error.

The higher-order contributions can be represented by the multipole expansion. The multipole representations can be derived by studying the connections between (4.1) and (4.5). In the addition theorem (4.1), high-order contributions are:

$$\sum_{l=L_0+1}^{L_m} (-1)^l (2l+1) j_l(kd) h_l^{(1)}(kr_{mn}) P_l(\hat{d} \cdot \hat{r}_{mn}) \tag{4.54}$$

Applying the addition theorem for the Legendre polynomials:

$$P_l(\hat{d} \cdot \hat{r}_{mn}) = \frac{4\pi}{2l+1} \sum_{m=-l}^{l} Y_{lm}(\theta_d, \phi_d) \cdot Y_{lm}^*(\theta_{mn}, \phi_{mn}) \tag{4.55}$$

Equation (4.54) becomes:

$$\sum_{l=L_0+1}^{L_m} I_l^{\mathrm{mp}} = \sum_{l,m}^{L_0<l\leq L_m} 4\pi(-1)^l j_l(kd)Y_{lm}(\theta_d,\phi_d) \cdot h_l^{(1)}(kD)Y_{lm}^*(\theta_{mn},\phi_{mn}) \tag{4.56}$$

Letting $\mathbf{d} = \mathbf{r}_{im} + \mathbf{r}_{nj}$, we have [33, pp. 594]:

$$j_l(kd)Y_{lm}(\theta_d,\phi_d) = \sum_{l'm'} Y_{l'm'}(\theta_{im},\phi_{im})j_{l'}(kr_{im})\cdot \sum_{l''} 4\pi i^{l'+l''-l}Y_{l'',m-m'}(\theta_{nj},\phi_{nj})j_{l''}(kr_{nj})\mathcal{A}_{L,L',L''} \tag{4.57}$$

By changing of variables $m'' = m' - m$, the summation of m is transformed into the summation of m''. Changing the orders of the summations and applying the conjugate relation of the spherical harmonics:

$$Y_{lm}^*(\theta,\phi) = (-1)^m Y_{l,-m}(\theta,\phi) \tag{4.58}$$

Equations (4.56) can be written as follows in (4.59).

$$\sum_{l=L_0+1}^{L_m} I_l^{\mathrm{mp}} = \sum_{l'm'}\sum_{l''m''} \underbrace{2\sqrt{\pi}Y_{l'm'}(\theta_{im},\phi_{im})j_{l'}(kr_{im})}_{\text{receiving pattern element}}\cdot \underbrace{2\sqrt{\pi}(-1)^{l''}Y_{l''m''}^*(\theta_{nj},\phi_{nj})j_{l''}(kr_{nj})}_{\text{radiation pattern element}}\cdot \underbrace{\sum_{l=L_0+1}^{L_m} 4\pi i^{l'+l-l''}Y_{l,m''-m'}(\theta_{mn},\phi_{mn})h_l^{(1)}(kr_{mn})(-1)^{m'}\mathcal{A}_{L,L',L''}}_{\text{translation element}} \tag{4.59}$$

In (4.59), the first two brackets are the elements of the receiving pattern and the radiation pattern as defined in (4.6). Also noticing that:

$$\mathcal{A}_{L'',L',L} = (-1)^{m'}\mathcal{A}_{L,L',L''} \tag{4.60}$$

the third bracket is similar to the element of the translation matrix defined in (4.7). Therefore, we can write the high-order contributions in terms of the

multipole expansion as:

$$\sum_{l=L_0+1}^{L} I_l^{\text{mp}} = \boldsymbol{\beta}(\mathbf{r}_{im}) \cdot \tilde{\overline{\boldsymbol{\alpha}}}(L_0^+, \mathbf{r}_{mn}) \cdot \boldsymbol{\beta}(\mathbf{r}_{nj}) \tag{4.61}$$

Since l is bounded within $[L_0{+}1, L_m]$, the matrix element of $\tilde{\overline{\boldsymbol{\alpha}}}(\mathbf{r}_{mn})$ is slightly modified from (4.7) as:

$$\begin{aligned}\tilde{\alpha}_{L',L}(L_0^+, \mathbf{r}'') = \sum_{l''=L_0+1}^{L_m} 4\pi i^{(l'+l''-l)} \mathcal{A}_{L,L',L''} \cdot \\ Y_{l'',m-m'}(\theta'', \phi'') h_{l''}^{(1)}(kr'')\end{aligned} \tag{4.62}$$

The matrix elements of $\boldsymbol{\beta}$ are the same as defined in (4.6).

Two ways can now be used to determine the size of $\overline{\boldsymbol{\beta}}$ by comparing the upper bounds of the summation in (4.7) and (4.62). The more accurate approach is to let L_β, the maximum harmonic order of $\overline{\boldsymbol{\beta}}$, be L_m. Another more efficient approach is by letting $L_\beta = \lceil L_m/2 \rceil$, where $\lceil \cdot \rceil$ denotes the ceiling function. Then the order of $\overline{\boldsymbol{\beta}}$ is reduced by half and the size of the matrices $\overline{\boldsymbol{\beta}}$ is significantly reduced compared to the first approach.

$$\begin{aligned}\frac{e^{ikr_{ij}}}{r_{ij}} \approx \underbrace{ik \int d^2\hat{k} e^{i\mathbf{k}\cdot\mathbf{r}_{im}} \cdot \alpha(L_0^-, \mathbf{r}_{mn}) \cdot e^{i\mathbf{k}\cdot\mathbf{r}_{nj}}}_{\text{plane wave expansion}} \\ + \underbrace{ik\Big(\boldsymbol{\beta}(\mathbf{r}_{im}) \cdot \tilde{\overline{\boldsymbol{\alpha}}}(L_0^+, \mathbf{r}_{mn}) \cdot \boldsymbol{\beta}(\mathbf{r}_{nj})\Big)}_{\text{multipole expansion}}\end{aligned} \tag{4.63}$$

$$\epsilon(L_0) = \left| 1 - \frac{\int d^2\hat{k} e^{i\mathbf{k}\cdot\mathbf{r}_{im}} \cdot \alpha(L_0^-, \mathbf{r}_{mn}) \cdot e^{i\mathbf{k}\cdot\mathbf{r}_{nj}}}{\sum_{l=0}^{L_0} (-1)^l (2l+1) j_l(kd) h_l^{(1)}(kr_{mn}) P_l(\hat{d} \cdot \hat{r}_{mn})} \right| \tag{4.64}$$

where $\mathbf{d} = \mathbf{r}_{im} + \mathbf{r}_{nj}$.

With (4.52), (4.53) and (4.61), the hybrid FMA can be formulated as in (4.63). It can be easily generalized to multilevel by further factorizing the plane wave in the plane wave expansion term and leveraging (4.8) and (4.9) in the multipole expansion term. The radiation pattern, receiving pattern, aggregation and disaggregation are still the same as the conventional diagonal and dense FMA. The order splitting appears only in the translations α, which

facilitates the implementations with an existing FMA code. The splitting boundary L_0 and the truncated order L_m are then to be determined to achieve a target accuracy.

4.2.4 Determining L_0 and L_m

The splitting boundary L_0 is used to avoid the low-frequency breakdown of the plane wave expansion such that the numerical error defined in (4.64) is bounded. As k becomes smaller, the error becomes increasingly large for a large L_0. The numerical reasons for this are due to the small values of j_l and large values of $h_l^{(1)}$, as discussed in Section 4.2.1.1. One way to determine L_0 is to avoid the amplitude of the left-hand side in (4.2) from dropping below the numerical noise $\mathcal{N}$. The reason that L_0 is not determined the by the value of $h_l^{(1)}$ is because the argument of j_l is smaller than the argument of $h_l^{(1)}$. Therefore j_l decays faster than h_l growth with respect to l. The numerical stability (4.2) becomes more significant.

Since $|P_l(\hat{d} \cdot \hat{D})| \sim O(1)$, we can let:

$$L_0 = \max\{l : |j_l(ka)| > \mathcal{N}\} \tag{4.65}$$

where k is the wave number and a is the oct-tree box size. For double-precision floating numbers, $\mathcal{N}$ can be as low as 2.2×10^{-16}. However, the aggregation and disaggregation distance can be small compared to a, which makes it difficult to estimate the numerical error analytically at this stage. Instead, we performed a numerical test for a proper choice of $\mathcal{N}$. Five hundred points are randomly drawn from two z-axis aligned boxes (the box length $a = 1$ m and center-to-center distance $r_{mn} = 2$ m) respectively. These 500×500 combinations of points are used as the source and field points to validate the results. The summation at the right-hand side of (4.64) is calculated analytically and the integral is computed with the numerical integration. The value of ka is swept from 10^{-6} to 10^{-1} for different values of $\mathcal{N}$. The statistical mean relative errors are plotted in Figure 4.4 for $\mathcal{N} = 10^{-10}$. We can see that the maximum mean error is 1.12×10^{-5}. Then the bounded relative errors are collected for different values of $\mathcal{N}$ and are plotted in Figure 4.5.

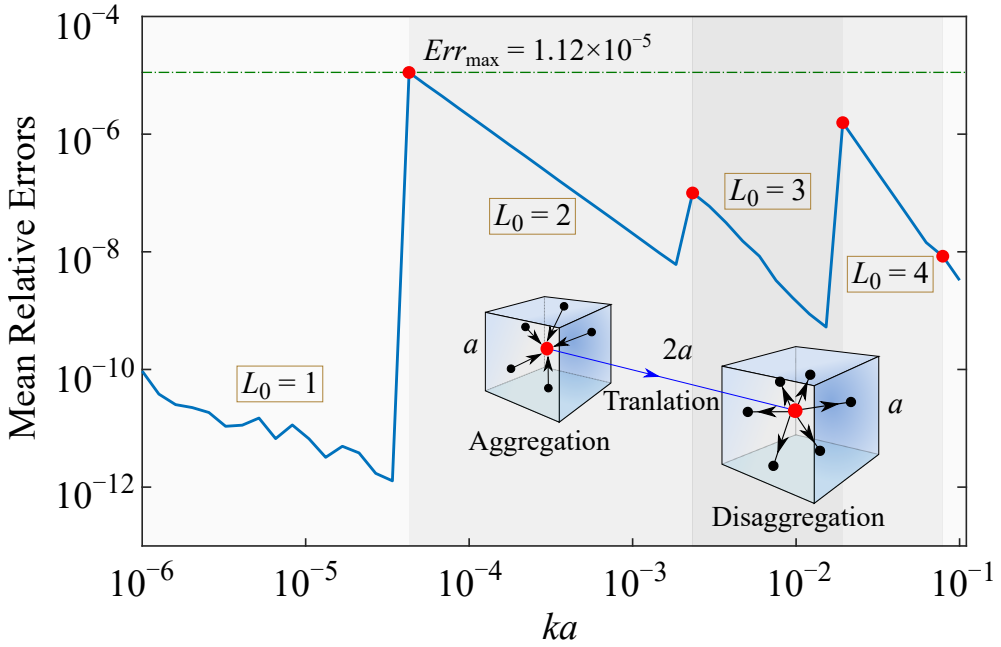

Figure 4.4: The mean relative error versus ka at the low-frequency regime with L_0 determined by (4.65) for points randomly chosen from the two boxes. The numerical noise $\mathcal{N} = 10^{-10}$.

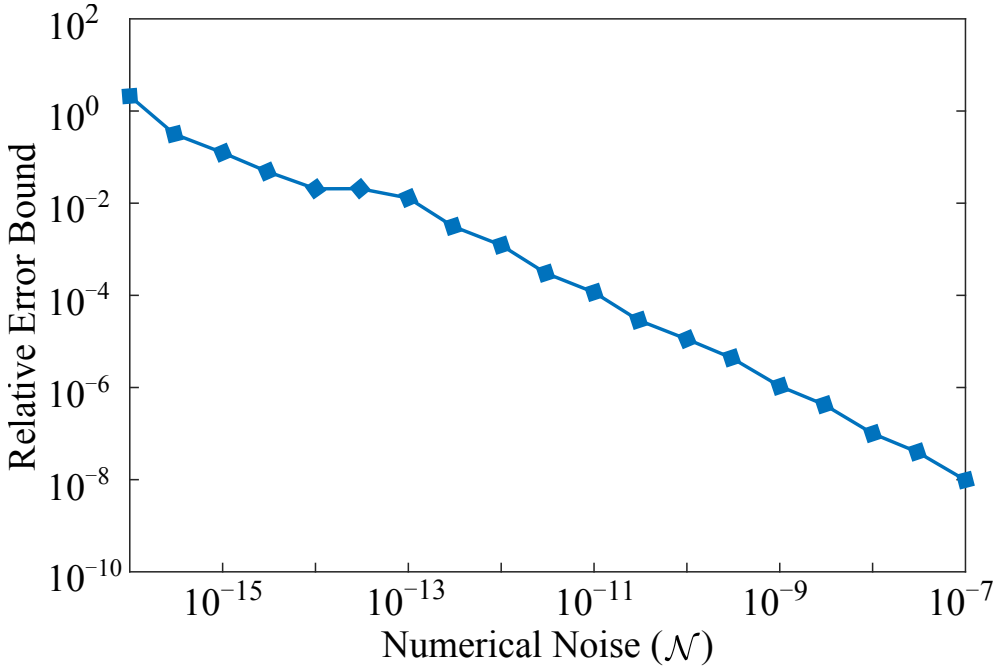

Figure 4.5: The maximum errors defined in (4.64) of the random source-field points versus the numerical noise $\mathcal{N}$. The integral on the Ewald sphere is evaluated using $n_\theta = L_0 + 2$ quadrature point in θ direction and $n_\phi = 2(n_\theta + 1)$ in ϕ direction.

Apparently $\mathcal{N}$ should be chosen larger than 10^{-13} to achieve an estimable error, since the error decreases linearly with $\mathcal{N}$ in the log-space. Figure 4.5 can then be used to determine $\mathcal{N}$ for a given accuracy level ϵ:

$$\mathcal{N} \approx \frac{C}{\epsilon} \tag{4.66}$$

where C is a small constant, which highly depends on the samplings of the quadrature points in the integral in (4.64). In our case, $C = 10^{-15}$. Together with (4.65) and (4.66), L_0 can be found.

The truncate number L_m is determined to bound the error of the approximation in the Green's function in (4.63). Since the error of the plane wave expansion can be bounded by the determination of L_0, and the multipole expansion is proven equivalent to the addition theorem in (4.59), the problem reduces to the determination of truncation number in the addition theorem in (4.1). The relative error can be estimated as [81]:

$$\epsilon \approx nka(2L_m + 3) \left| j_{L_m+1}(kd) h^{(1)}_{L_m+1}(nka) \right| \tag{4.67}$$

where $N = n - 1$ is the number of buffer boxes. In the worse case scenario, $d = \sqrt{3}a$. It should be noted that (4.67) provides a loose bound of the error since the Legendre polynomial is dropped from the addition theorem in (4.1) and the cancellations of the higher-order terms are not considered.

At low frequencies ($ka < 1$), (4.67) reduces to the static approximation equation [63, 32]:

$$L_m = \frac{d_0}{\log(na/d)} - 1 \tag{4.68}$$

where $d_0 = \log(1/\epsilon)$ and L_m becomes a constant of ka.

At higher frequencies ($ka \gg 1$), (4.67) reduces to the excess bandwidth equation [57, Ch. 3, pp. 86-88]:

$$L_m = kd + 1.8 d_0^{\frac{2}{3}} (kd)^{\frac{1}{3}} \tag{4.69}$$

Therefore, with (4.67) to (4.69), the truncate number L_m can be determined given a target accuracy ϵ.

4.2.5 Multilevel and Multi-Scale Considerations

For a multi-scale problem, ka covers a wide range at different levels of the oct-tree. As ka increases, more plane wave modes will be used in the factorization of the Green's function. At the low-frequency regime, L_m keeps a constant of ka and it increases in higher-frequency regimes.

Given a target accuracy ϵ, one can use (4.65) and (4.66) to find L_0 and use (4.67)-(4.69) to find L_m for all ka. We can find a box size a_T, at which $L_0 = L_m$. This is the transition box between the hybrid FMA and the conventional plane wave FMA. A hybridization of the multipole and plane wave expansions are used for $a < a_T$, while only the plane wave expansion is used for $a > a_T$.

In Table 4.1, some values of ka_T are shown for different accuracy levels and different numbers of buffer boxes. In this case, L_m is determined with $d = a$. Although it is not the worst case, it suffices to control the errors for engineering applications without increasing the computational costs significantly, as will be shown in Section 4.3.2 and Table 4.3.

Table 4.1: A table of the transition box sizes (ka_T), the number of modes (L_m and L_0) and the number of harmonics of $\overline{\boldsymbol{\beta}}$ ($L_\beta = \lceil L_m/2 \rceil$).

Accuracy ϵ	N	ka_T	L_m & L_0	L_β
1e-3	1	0.90	11	6
	2	0.15	7	4
1e-4	1	2.21	14	7
	2	0.57	9	5
1e-5	1	5.23	19	10
	2	1.37	11	6
1e-6	1	10.59	26	13
	2	3.61	15	8

4.2.6 Rotation for Multipole Expansions

It is apparent that, in order to achieve a high accuracy, many multipole harmonics are needed, especially at low frequencies when L_0 is small. A rotation technique can be applied to reduce the number of operations from L_m^4 to L_m^3 [79].

In this technique, the translation matrices $\overline{\boldsymbol{\alpha}}$ and $\overline{\boldsymbol{\beta}}$ are factorized using the sparse rotation matrices $\overline{\mathbf{D}}^T$ and $\overline{\mathbf{D}}$, such that:

$$\overline{\boldsymbol{\tau}}(\mathbf{r}) = \overline{\mathbf{D}}^T(\theta, \phi) \cdot \overline{\boldsymbol{\tau}}(\hat{z}r_z) \cdot \overline{\mathbf{D}}(\theta, \phi) \tag{4.70}$$

where $\overline{\boldsymbol{\tau}}$ can be $\overline{\boldsymbol{\beta}}$ or $\tilde{\overline{\boldsymbol{\alpha}}}$. As a result, the matrices for z direction translation become block-diagonal and the computational cost is reduced. This technique is incorporated in the proposed method. More details can be found in [57, Ch. 5, pp. 184-189].

4.3 Numerical Results

In this section, we first demonstrate the accuracy of the proposed method using point-to-point testing for the single-level worse case and some multi-level application cases. Then this method is applied to the A-EFIE formulation to solve electromagnetic scattering problems.

4.3.1 Single-Level Worst Case

When the field and source points are located at the corners to the cube boxes, as shown in Figure 4.6, the error is maximized. The distance D is related to the number of buffer boxes. The worse simulation errors of these source-field points are found for a range of frequencies, from $ka = 10^{-6}$ (very low frequency) to $ka = 1$ (middle frequency). In this case, the truncate number L_m is determined with $d = \sqrt{3}a$ together with the number of buffer boxes N.

In Figure 4.7, the worst relative errors with one buffer box, $D = 2a$, are plotted for accuracy levels from $10^{-4.5}$ to 10^{-3}. The simulation errors are very closed to the target accuracies. In Figure 4.8, the results with two buffer boxes, $D = 3a$, are plotted for accuracy levels from 10^{-8} to 10^{-5}.

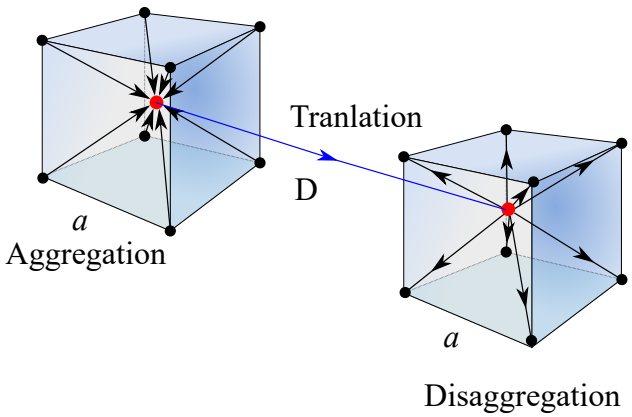

Figure 4.6: The worst case for single-level FMA calculations.

Compared to the case of the two buffer boxes, it requires a large L_m to achieve a high accuracy when there is only one buffer box. Therefore, it is more practical to set the target accuracy lower when only one buffer box is in use. Both simulation results demonstrate that the accuracies can be well controlled using the proposed method.

4.3.2 Multilevel Application Cases

We further apply the method to multilevel simulations. One of the $85,000$ nodes on a sphere surface (radius = 1 m) is used as the source point and others are used as the field points. The exact scalar Green's functions are compared with the simulated Green's function using the proposed multilevel hybrid FMA.

Since this setup does not necessarily include the worse case, we use $d = \sqrt{2}a$ and $d = a$ to determine the truncating number L_m respectively. In these two cases, the maximum and the mean relative errors are tabulated in Table 4.2 and Table 4.3.

Table 4.2 shows that with $d = \sqrt{2}a$ and the target accuracy level of $\epsilon = 10^{-8}$, even the maximum relative error is bounded near ϵ, and the mean error is well below it. In Table 4.3, a lower accuracy $\epsilon = 10^{-5}$ and $d = a$ are applied in the simulations. Although the maximum error is larger than ϵ, the mean error is bounded below the target, which makes it applicable for most engineering applications. From Tables 4.2 and 4.3, the simulation results demonstrate that the errors are stable and well-controlled in the multilevel simulations.

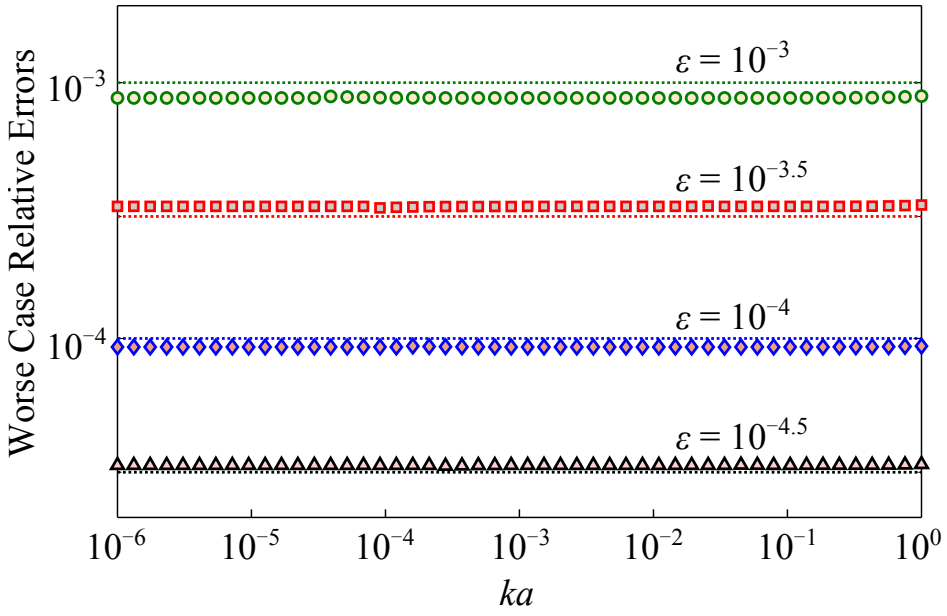

Figure 4.7: The simulated worst-case relative errors with one buffer box ($D = 2a$) and the target accuracies of $10^{-3}, 10^{-3.5}, 10^{-4}$, and $10^{-4.5}$.

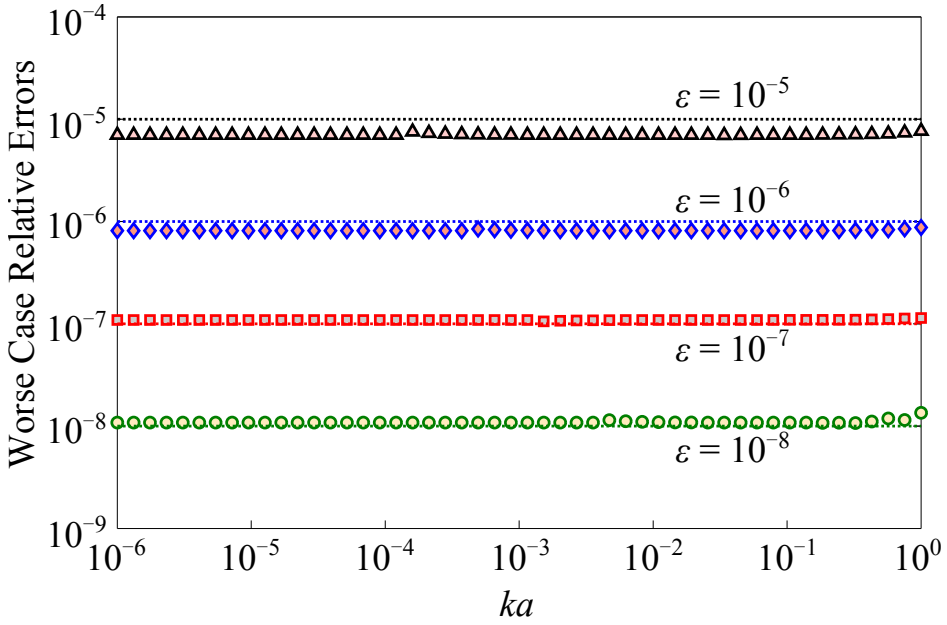

Figure 4.8: The simulated worst-case relative errors with two buffer boxes ($D = 3a$) and the target accuracies of $10^{-5}, 10^{-6}, 10^{-7}$, and 10^{-8}.

It should be noted that the choice of d depends on the simulated structures and the oct-tree structures. However, from the numerical experiments, a choice of $d = \sqrt{2}a$ mostly suffices to bound the error closed to the target accuracy.

Table 4.2: Multilevel simulation errors using $d = \sqrt{2}a$ at $kr = 10^{-3}$ with the target accuracy $\epsilon = 10^{-8}$.

ϵ	Levels	Maximum Error	Mean Error
1e-8	1	1.22012543e-08	8.97415766e-12
	2	1.60838463e-08	9.54411259e-12
	3	1.60838259e-08	9.55155468e-12
	4	1.60838271e-08	9.62308788e-12
	5	1.60838198e-08	9.60763710e-12

Table 4.3: Multilevel simulation errors using $d = a$ at $kr = 10^{-3}$ with the target accuracy $\epsilon = 10^{-5}$.

ϵ	Levels	Maximum Error	Mean Error
1e-5	1	3.65159596e-4	8.55934601e-06
	2	6.26361657e-4	8.16650990e-06
	3	6.26361306e-4	8.36854264e-06
	4	6.26361948e-4	8.40962606e-06
	5	6.26361887e-4	8.41638564e-06

4.3.3 Spherical Scattering Validations

We further integrate the hybrid FMM into the augmented electric field integral equation solver [14], a surface integral equation solver suitable for low-frequency applications. Sphere ($r = 1$ m) scattering problems are solved with plane wave excitations. There are over 8,400 triangle panels and 12,000 edges on the surface of the sphere. The oct-tree level is set to be 4 and there is one buffer box. The maximum number of harmonics is determined with $d = \sqrt{2}a$. The GMRES solver is used as the iterative solver and the tolerance is set to be equal to the accuracy level of the FMA solver.

Figure 4.9 shows the RCS simulations, the Mie series solutions and the surface current distribution at 1 kHz with an accuracy level of $\epsilon = 10^{-6}$. The currents are solved accurately and the RCS simulations match well with the Mie series at very low frequencies. Figure 4.10 shows the matched RCS simulations and the surface current distribution at 0.6 GHz with an accuracy level of $\epsilon = 10^{-4}$. These results show that the scattering problems can be

solved accurately using the proposed hybrid FMA.

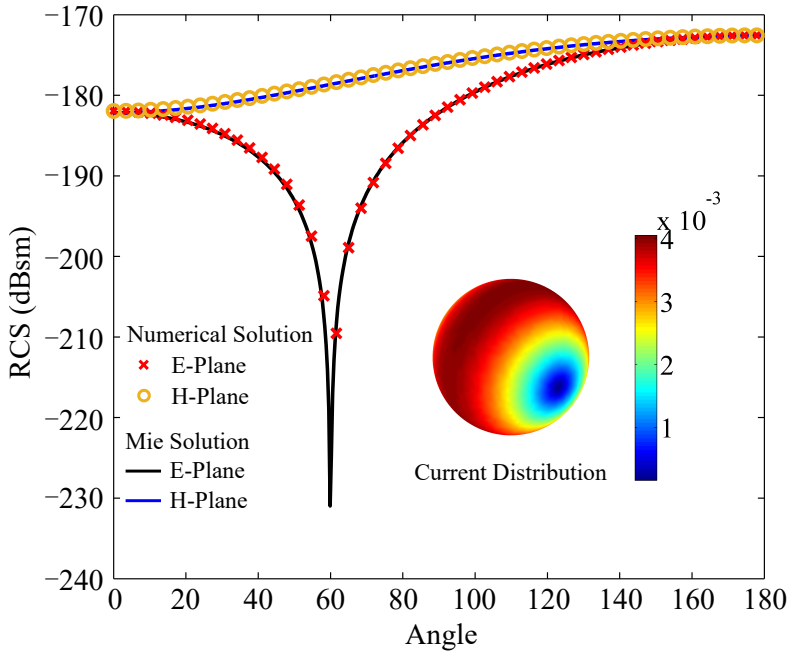

Figure 4.9: The simulated RCS compared with the Mie series solutions and the surface current distribution at 1 kHz for a 1 m sphere.

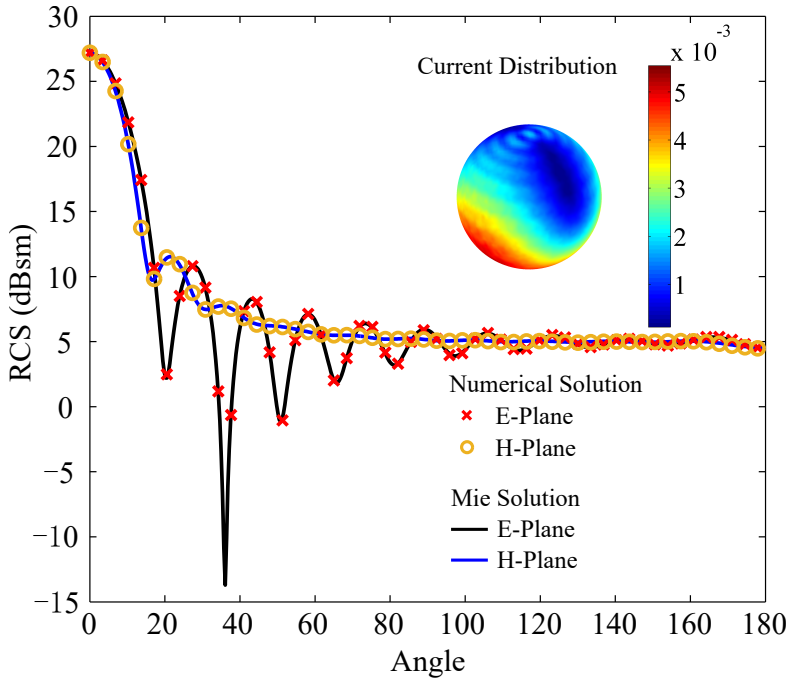

Figure 4.10: The simulated RCS compared with the Mie series solutions and the surface current distribution at 0.6 GHz for a 1 m sphere.

4.4 Conclusions

In this chapter, we propose a novel hybrid FMA for broadband electromagnetic simulations. The method takes advantage of the developments in dense and diagonal FMA. Both the multipole and plane wave expansions are used in multi-scale problems. The accuracy can be well controlled and very high accuracy can be achieved. Numerical results are used to validate the accuracy of the method.

Chapter 5

Efficient Calculations of the Casimir Force Using the Surface Integral Equation

5.1 Introduction

The Casimir force is an attractive force between two neutral perfect conducting plates, derived by Casimir in 1948 [17]:

$$F = -\frac{\pi^2 \hbar c}{240 d^4} \tag{5.1}$$

The relation in (5.1) between the attractive force F and the distance d was derived by considering the zero-point electromagnetic energy between the two plates. Then this energy is compared to the electromagnetic energy of free space. Finally the variations of the energy give rise to the attractive force. This can be interpretated as due to the electromagnetic fluctuation of vaccum at zero temperature. The fluctuation induces the polarizations on neutral particals, and therefore induces the force between the particals.

As opposed to the predictions of zero force between neutral particles in classical electromagnetics, this weak attractive force arises as a result of the zero-point energy in vacuum:

$$\sum_{\omega} \frac{1}{2} \hbar \omega \tag{5.2}$$

Casimir was first motivated by the calculations of the retarded van der Waals force [83]. One kind of the van der Waals force arises between two polarized particles. The force is attractive because two aligned dipoles of opposite polarity have minimum energy. This interaction is also known as the Keesom interaction. Another kind of van der Waals interaction, known as the Debye interaction, appears when a polarized particle induces the dipole moment on another neutral, non-polarized particle. A more general consideration of the van der Waals interaction is the interaction between two non-

polarized particles. London in 1930 [84] introduced a quantum-mechanical derivation of the interaction energy between two identical non-polarized particles as:

$$V(d) \propto d^{-6} \tag{5.3}$$

Casimir's colleagues (see [83]) suggested, from the results of the experiments, that London's consideration of the force does not consider the retardation effects. The interacting energy should fall more rapidly than d^{-6} by considering the retardation effects. Then in [83], Casimir and Polder calculated the interaction energy between two particles by using the perturbation theory and considering the finite speed of light. They found the retarded van der Waals energy to be:

$$V(d) = \frac{23\hbar c}{4\pi d^7}\alpha^2 \tag{5.4}$$

where α is the polarizability of the particles.

A major problem of generalizing the above equation to macroscopic structures is that the retarded van der Waals force is non-additive. This difficulty led Casimir to calculate the force between macroscopic structures by considering the zero-point energy of the electromagnetic energy, as introduced earlier.

Lifshitz in 1956 [21] introduced a more general theory of the van der Waals force for dielectric materials at finite temperature. Lifshitz considered two dielectric half spaces separated by vacuum. The electromagnetic fluctuations in the three regions are generated by the Lagevin-like sources, namely fluctuating electric and magnetic polarizations. The polarizations are correlated locally in $\mathbf{r}$ and the correlations are determined by the imaginary part of ϵ_r. This is the result of the fluctuation-dissipation theorem [22, 23]. With this relation, one can use the Maxwell stress tensor to calculate the force. Since the fluctuating field is confined by the boundary condition, the force in turn is related to the imaginary part of the dyadic Green's function. Finally Lifshitz arrived at the same equation as Casimir's results at the perfect electric conductor limit.

Recent progress in the experiments [15, 16] of Casimir force measurement has stimulated the calculations of Casimir force for arbitrary structures beyond the proximity force approximation (PFA) (see Appendix B for some simple examples of PFA). Since PFA is only valid for very narrow gaps, more general methods to calculate the Casimir force is needed for arbitrary

structures. By considering the EM interaction between compact objects, a scattering approach was proposed [18] and as a result, the Casimir energy can be expressed in terms of scattering matrices. Another similar approach was taken using the path integral [20] and the source of the Casimir force can be interpreted as due to the fluctuation surface currents. Both of the above two approaches arrive at the same equation that we will derived in Section 5.2.

5.2 Methods

The Casimir force can be derived in various ways. The two major starting points are using the Maxwell stress tensor and the calculation of the variations of the zero-point energy of the system. We will follow the procedure of the second approach. Then we can take the derivative to get the Casimir force.

5.2.1 Derivations of the Casimir Energy and Force

If we are interested in the zero-point energy of a two-object system $\mathcal{S}_d$, with a distance d between the objects. The zero-point energy of the system, as a function of d is:

$$E(d) = \frac{1}{2}\sum_{\omega_d} \hbar\omega_d \tag{5.5}$$

where ω_d is the angular frequency of the resonance modes of the system. These ω_d of physical interests lie on the real half-plane.

Apparently the energy defined in (5.5) diverges since there is no high frequency cutoff. We can regularized the energy by subtracting it with $E(\infty)$, which is the zero-point energy of the system $\mathcal{S}_\infty$ when the two objects are infinitely far apart. Then the regulated Casimir energy is:

$$E = \frac{\hbar}{2}\left(\sum_{\omega_d}\omega_d - \sum_{\omega_\infty}\omega_\infty\right) \tag{5.6}$$

The resonance frequencies ω_d and ω_∞ can be calculated using classical electromagnetics. Instead of calculating each ω_d or ω_∞, which is very difficult, one can convert the summation into an integral on complex plane using

the argument principle, first introduced in [19], and extensively studied in [85, 86, 87]. We briefly outline the procedures here.

According to the argument principle, for an analytic function $f(\omega)$, if $f(\omega_0)$ gives zero and $f(\omega_p)$ gives poles, then

$$\frac{1}{2\pi i}\oint_C d\omega\phi(\omega)\frac{d}{d\omega}\log f(\omega) = \sum_{\text{zeros}}\phi(\omega_0) - \sum_{\text{poles}}\phi(\omega_p) \tag{5.7}$$

Let $\phi(\omega) = \omega$ and use integration by parts for the integral, we have:

$$\frac{i}{2\pi}\oint_C d\omega\log f(\omega) = \sum_{\text{zeros}}\omega_0 - \sum_{\text{poles}}\omega_p \tag{5.8}$$

Then it becomes natural to use the impedance matrix to construct $f(\omega)$. Notice that the determinant of the impedance matrix of the system $\mathcal{S}_d$ is zero at the resonance frequencies, due to the rank deficiency of the matrix, i.e.

$$\det\overline{\mathbf{M}}_d(\omega_d) = 0 \tag{5.9}$$

The inverse of the determinant of the impedance matrix of the system $\mathcal{S}_\infty$ gives poles at its resonance frequencies, i.e.

$$\frac{1}{\det\overline{\mathbf{M}}_\infty(\omega_\infty)} \to \text{pole} \tag{5.10}$$

One constructs $f(\omega)$ as:

$$f(\omega) = \frac{\det\overline{\mathbf{M}}_d(\omega)}{\det\overline{\mathbf{M}}_\infty(\omega)} \tag{5.11}$$

Plugging (5.9), (5.10) and (5.11) into (5.8), the expression of the Casimir energy is:

$$E = \frac{\hbar}{2}\left(\sum_{\omega_d}\omega_d - \sum_{\omega_\infty}\omega_\infty\right) = \frac{i\hbar}{4\pi}\oint_C d\omega\log\frac{\det\overline{\mathbf{M}}_d(\omega)}{\det\overline{\mathbf{M}}_\infty(\omega)} \tag{5.12}$$

We then need to choose the contour of C to simplify the expression in (5.12). Notice that the resonance frequencies of interests are on the right half-plane. Furthermore due to causality, the poles of the dyadic Green's function lie in the lower half-plane. If the contour C is chosen as in Figure 5.1, all the zeros

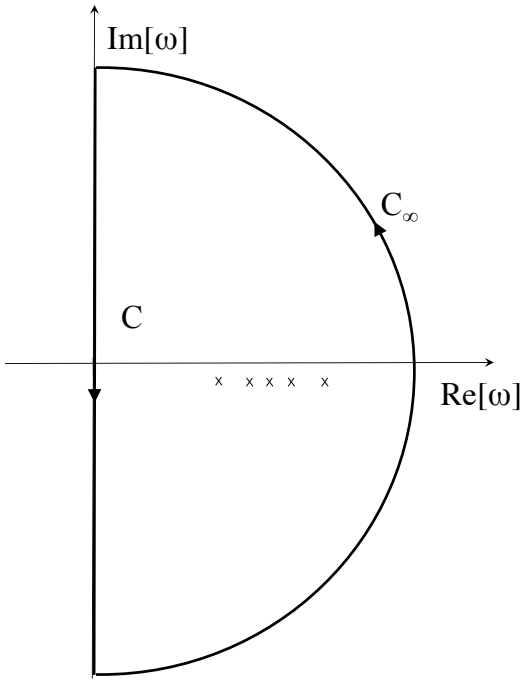

Figure 5.1: The integration contour C.

and poles of $f(\omega)$ in (5.11) are captured.

The integral along C_∞ does not contribute to the Casimir force. One way to argue that is to use Jordan's lemma, although it is not obvious that $\log f(\omega)$ is of the form of $g(\omega)e^{ia\omega}$. However, when $\omega \to \infty$, $\overline{\mathbf{M}}_d(\omega)$ no longer depend on d. Therefore, the integral along C_∞ will give rise to a constant contribution to the energy, which is meaningless and irrelevant to the force. Therefore, the contour integral in (5.12) is reduced to the integral along the path C in Figure 5.1. By changing of variable $\omega = ic\xi$, the Casimir energy can be written as:

$$E = \frac{\hbar c}{4\pi}\int_{-\infty}^{\infty} d\xi \log \frac{\det \overline{\mathbf{M}}_d(ic\xi)}{\det \overline{\mathbf{M}}_\infty(ic\xi)} \tag{5.13}$$

$$= \frac{\hbar c}{2\pi}\int_{0}^{\infty} d\xi \log \frac{\det \overline{\mathbf{M}}_d(ic\xi)}{\det \overline{\mathbf{M}}_\infty(ic\xi)} \tag{5.14}$$

Finally the expression of the Casimir energy is given in (5.14), the equation of the Casimir force $F = -\frac{\partial}{\partial r}E(d)$ is:

$$F = -\frac{\hbar c}{2\pi}\int_{0}^{\infty} d\xi \mathrm{tr}\left(\overline{\mathbf{M}}_d^{-1}(ic\xi)\cdot\frac{\partial}{\partial \mathbf{d}}\overline{\mathbf{M}}_d(ic\xi)\right) \tag{5.15}$$

5.2.2 The Casimir Energy and Force Representations Using the Surface Integral Equation

In the calculations of the Casimir energy and force, the matrices $\overline{\mathbf{M}}_d$ and $\overline{\mathbf{M}}_\infty$ need to satisfy:

$$\det \overline{\mathbf{M}}_d(\omega_d) = 0 \tag{5.16}$$

$$\frac{1}{\det \overline{\mathbf{M}}_\infty(\omega_\infty)} \rightarrow \text{pole} \tag{5.17}$$

where ω_d and ω_∞ lie on the right-lower complex plane of ω. Equations (5.16) and (5.17) imply that ω_d and ω_∞ are the resonance frequencies of the system $\mathcal{S}_d$ and $\mathcal{S}_\infty$ respectively. Therefore, we can use the impedance matrices in the surface integral equation (SIE) of the systems $\mathcal{S}_d$ and $\mathcal{S}_\infty$ for $\overline{\mathbf{M}}_d$ and $\overline{\mathbf{M}}_\infty$. The impedance matrix maps the surface equivalent currents on the surfaces to cancel the incident fields. For perfect electric conductors (PEC):

$$\overline{\mathbf{M}} \cdot \mathbf{J} = \mathbf{E}_{inc} \tag{5.18}$$

where $\overline{\mathbf{M}}$ can be $\overline{\mathbf{M}}_d$ or $\overline{\mathbf{M}}_\infty$. The impedance matrix in the electric field integral equation (EFIE) formulation can be used for $\overline{\mathbf{M}}_d$ and $\overline{\mathbf{M}}_\infty$.

For dielectrics:

$$\overline{\mathbf{M}}_d \cdot \begin{bmatrix} \mathbf{J} \\ \mathbf{M} \end{bmatrix} = \begin{bmatrix} \mathbf{E}_{inc} \\ \mathbf{H}_{inc} \end{bmatrix} \tag{5.19}$$

The impedance matrix of in the Poggio-Miller-Chang-Harrington-Wu-Tsai (PMCHWT) formulation can be used.

For a two-object system, the impedance matrix can be written in a general 2×2 form as:

$$\overline{\mathbf{M}}_d(ic\xi) = \begin{bmatrix} \mathcal{O}_{11}(ic\xi) & \mathcal{O}_{12}(ic\xi) \\ \mathcal{O}_{12}^T(ic\xi) & \mathcal{O}_{22}(ic\xi) \end{bmatrix} \tag{5.20}$$

where $\mathcal{O}_{ij}(ic\xi)$ is the interaction matrix between objects i and j evaluated at the imaginary frequency $ic\xi$, and we have used the symmetry property of $\mathcal{O}_{12}$ and $\mathcal{O}_{21}$. Using the Kramers-Kronig relationship, one can find the permittivity ϵ to be real at imaginary frequencies:

$$\epsilon(i\xi) - \epsilon(\infty) = \frac{2}{\pi} \int_0^\infty d\omega' \frac{\omega' \Im[\epsilon(\omega') - \epsilon(\infty)]}{\omega'^2 + \xi^2} \tag{5.21}$$

Therefore, the matrix elements of $\mathcal{O}_{ij}(ic\xi)$ are also real.

In (5.15), the derivative is taken with respect to the relative distance of the two objects, i.e.

$$\frac{\partial}{\partial \mathbf{d}}\overline{\mathbf{M}}_d(ic\xi) = \begin{bmatrix} \overline{\mathbf{0}} & \frac{\partial}{\partial \mathbf{d}}\mathcal{O}_{12}(ic\xi) \\ \frac{\partial}{\partial \mathbf{d}}\mathcal{O}_{12}^T(ic\xi) & \overline{\mathbf{0}} \end{bmatrix} \tag{5.22}$$

The expressions of the Casimir energy and force in (5.14) and (5.15) are then represented by the impedance matrices in the SIE.

5.2.3 Numerical Implementations

The calculations of the Casimir energy involve evaluations of the log determinants of the matrices at imaginary frequencies and the calculations of the Casimir force involve evaluations of the traces. The expressions are:

$$E = \frac{\hbar c}{2\pi}\int_0^\infty d\xi \left(\log\det \overline{\mathbf{M}}_d(ic\xi) - \log\det \overline{\mathbf{M}}_\infty(ic\xi)\right) \tag{5.23}$$

and

$$F = -\frac{\hbar c}{2\pi}\int_0^\infty d\xi \mathrm{tr}\left(\overline{\mathbf{M}}_d^{-1}(ic\xi)\cdot\frac{\partial}{\partial \mathbf{d}}\overline{\mathbf{M}}_d(ic\xi)\right) \tag{5.24}$$

which are identical to the equations in (5.14) and (5.15) but the matrices $\overline{\mathbf{M}}_d$ and $\overline{\mathbf{M}}_\infty$ are now constructed using the SIE.

First from the definition that $\omega = ic\xi$, ξ has the same unit of the wave number. The important contributions to the Casmir energy and force are from those $\xi \in (0, \tau)$, where τ depends on the size of the structure l due to that the Green's function at imaginary frequencies decays as $\frac{e^{-\xi l}}{l}$. We first normalize ξ by letting $\xi = \frac{2\pi}{l}\tilde{\xi}$, where c is the speed of light, l is the approximate size of the structure and $\tilde{\xi}$ is a unit-less parameter. The integrals then becomes:

$$I = \frac{\hbar c}{2\pi}\int_0^\infty d\xi f(ic\xi) = \frac{\hbar c}{l}\int_0^\infty d\tilde{\xi} f(i\frac{2\pi c}{l}\tilde{\xi}) \tag{5.25}$$

where $f(ic\xi)$ can be the kernel of the Casimir energy of Casimir force in (5.23) and (5.24).

Then we can convert the integral from $\tilde{\xi} \in (0, \infty)$ to $t \in (0, 1)$ by change

of variables:

$$\tilde{\xi} = \frac{t}{1-t} \qquad \text{or} \qquad t = \frac{\tilde{\xi}}{1+\tilde{\xi}} \tag{5.26}$$

Hence $d\tilde{\xi} = dt\frac{1}{(1-t)^2}$, the integral (5.25) becomes:

$$I = \frac{\hbar c}{l}\int_0^1 dt \frac{1}{(1-t)^2} f\left(i\frac{2\pi ct}{l(1-t)}\right) \tag{5.27}$$

Finally the integrals can be evaluated numerically using the Gauss-Legendre quadrature, such that:

$$I = \frac{\hbar c}{l}\sum_{j=1}^{N} \frac{w_j}{(1-t_j)^2} f\left(i\frac{2\pi ct_j}{l(1-t_j)}\right) = \frac{\hbar c}{l}\sum_{j=1}^{N} \tilde{w}_j f(i\tilde{t}_j) \tag{5.28}$$

where the integral is converted to a finite summation with the quadrature points t_j and the corresponding weighting w_j. The rest of the problem is to evaluate the kernel function $f(i\tilde{t}_j)$, which can be represented as the log determinants or the traces of the SIE matrices. For small matrices, they can be computed efficiently using the direct methods. However, As the matrix size becomes larger, the evaluation using direct methods becomes very inefficient. We will propose a fast computing scheme to calculate the Casimir force.

5.2.4 A Fast Computing Scheme

To calculate the Casimir force using (5.15), one needs to perform a matrix inverse of an $N \times N$ matrix $\overline{\mathbf{M}}^{-1}$, which is of $O(N^3)$ CPU complexity and $O(N^2)$ memory usage. As N gets large, such numerical costs are no longer reasonable. In this section, we will use the randomized SVD to reduce the size of the right matrix and then use the fast multipole algorithm to effectively perform the "inverse" of the left matrix.

When the two objects are farther apart from each other, the matrix at the right-hand side of (5.15), $\frac{\partial}{\partial \mathbf{d}}\overline{\mathbf{M}}_d$, is rank deficient. This is because the Green's function is a low-pass filter. When the distance between the two objects is sufficiently large, some evanescent waves from one object will vanish before reaching the other object. Therefore the far-field representation of the Green's function matrices can be largely compressed.

We can use the randomized SVD [88] to find a low-rank approximation for

$\frac{\partial}{\partial \mathbf{d}}\overline{\mathbf{M}}_d$, i.e.

$$\underbrace{\frac{\partial}{\partial \mathbf{d}}\overline{\mathbf{M}}_d}_{N\times N} \approx \underbrace{\overline{\mathbf{U}}}_{N\times k} \cdot \underbrace{\overline{\mathbf{\Sigma}}}_{k\times k} \cdot \underbrace{\overline{\mathbf{V}}^T}_{k\times N} \tag{5.29}$$

where the sizes of $\overline{\mathbf{U}}, \overline{\mathbf{\Sigma}}$ and $\overline{\mathbf{V}}^T$ are $N \times k$, $k \times k$ and $k \times N$ respectively, and the singular value matrix $\overline{\mathbf{\Sigma}}$ is diagonal. In the randomized SVD algorithm [88], the dominant computational cost is from the product of the matrix $\frac{\partial}{\partial \mathbf{d}}\overline{\mathbf{M}}_d$ and a random matrix (size: $N \times k$). The total computational cost of the randomized SVD is $O(4kT + 2k^2N)$, where T is the flops count of a matrix vector product.

Therefore, in order to calculate:

$$\overline{\mathbf{M}}_d^{-1} \cdot \frac{\partial}{\partial \mathbf{d}}\overline{\mathbf{M}}_d \tag{5.30}$$

we propose the following procedures:

1. Compute the randomized SVD of $\frac{\partial}{\partial \mathbf{d}}\overline{\mathbf{M}}_d$:

$$\frac{\partial}{\partial \mathbf{d}}\overline{\mathbf{M}}_d \approx \overline{\mathbf{U}} \cdot \overline{\mathbf{\Sigma}} \cdot \overline{\mathbf{V}}^T \tag{5.31}$$

   Assuming that the matrix vector product $\frac{\partial}{\partial \mathbf{d}}\overline{\mathbf{M}}_d \cdot \mathbf{v}$, where $\mathbf{v}$ is a vector, is performed using FMA with a cost of $O(N \log N)$, the leading order computational complexity is $O(kN \log N + k^2N)$.

2. Solving matrix equation with multiple right-hand sides:

$$\overline{\mathbf{X}} = \overline{\mathbf{M}}_d^{-1} \cdot \mathbf{U} \qquad \rightarrow \qquad \overline{\mathbf{M}}_d \cdot \overline{\mathbf{X}} = \mathbf{U} \tag{5.32}$$

   This requires solving $\overline{\mathbf{M}}_d \cdot \mathbf{x} = \mathbf{u}$ for k times. The computational complexity of this procedure can be reduced to $O(kN \log(N))$ if the fast multipole algorithm is used.

3. Compute dense-diagonal matrix products:

$$\overline{\mathbf{Y}} = \overline{\mathbf{X}} \cdot \overline{\mathbf{\Sigma}} \tag{5.33}$$

   This procedure is $O(kN)$ complexity since $\overline{\mathbf{\Sigma}}$ is diagonal.

4. Compute the trace:

$$\mathrm{tr}\left[\overline{\mathbf{Y}}\cdot\overline{\mathbf{V}}^{T}\right]=\sum_{i}^{N}\sum_{j}^{k}y_{ij}\cdot v_{ij} \tag{5.34}$$

This procedure is $O(kN)$ complexity.

Therefore, the leading order total computational complexity is determined by the procedures 1 and 2, with the total complexities of $O(kN\log(N))$. Large-scale computations of Casimir force using the above scheme can be achieved if a broadband FMA can be generalized to imaginary frequencies.

5.2.5 Imaginary Hybrid Fast Multipole Algorithm

We can extend the hybrid FMA in Chapter 4 from real frequencies to imaginary frequencies to meet the requirements of efficient evaluations of the matrix-vector products in the calculations of the Casimir force. Another reason for choosing the hybrid FMA is that a broadband stability is required in this problem, since in (5.15), an integral over frequencies from 0 to ∞ is required.

The conventional dense and diagonal FMA suffer from the efficiency problem and the accuracy problem at low frequencies and high frequencies respectively. The mixed form FMA [32] and the approximated diagonal FMA can be used [82], however, the methods are less accurate than the hybrid FMA. We will then generalize the FMA from real frequencies to purely imaginary frequencies, which is effectively changing the wave number k to $i\kappa$, where κ is a real number.

5.2.5.1 Generalization of the diagonal FMA

The diagonal FMA ultilizes the addition theorem (same as (4.1) in Chapter 4):

$$\frac{e^{ikr_{ij}}}{r_{ij}}=ik\sum_{l=0}^{\infty}(-1)^{l}(2l+1)j_{l}(kd)h_{l}^{(1)}(kr_{mn})P_{l}(\hat{d}\cdot\hat{r}_{mn}) \tag{5.35}$$

and the plane wave representation of the spherical Bessel function (same as (4.2) in Chapter 4):

$$j_l(kd)P_l(\hat{d}\cdot\hat{r}_{mn}) = \frac{1}{4\pi i^l}\int d^2\hat{k}e^{i\mathbf{k}\cdot\mathbf{d}}P_l(\hat{k}\cdot\hat{r}_{mn}) \tag{5.36}$$

At imaginary frequencies, when $k = i\kappa$, we change the spherical Bessel function j_l into the modified spherical Bessel function of the first kind i_l, with the relation:

$$j_l(kx) = i^l i_l(\kappa x) \tag{5.37}$$

and change the spherical Hankel function of the first kind $h_l^{(1)}$ to the modified spherical Bessel function of the second kind k_l, with the relation:

$$h_n^{(1)}(kx) = -i^{-l}k_l(\kappa x) \tag{5.38}$$

Therefore, (5.35) becomes:

$$\frac{e^{-\kappa r_{ij}}}{r_{ij}} = \kappa\sum_{l=0}^{\infty}(-1)^l(2l+1)i_l(\kappa d)k_l(\kappa r_{mn})P_l(\hat{d}\cdot\hat{r}_{mn}) \tag{5.39}$$

and (5.36) becomes:

$$i_l(\kappa d)P_l(\hat{d}\cdot\hat{r}_{mn}) = \frac{1}{4\pi}(-1)^l\int d^2\hat{\kappa}e^{-\boldsymbol{\kappa}\cdot\mathbf{d}}P_l(\hat{\kappa}\cdot\hat{r}_{mn}) \tag{5.40}$$

From (5.39) and (5.40), we have the plane wave representation of the Green's function:

$$\frac{e^{-\kappa r_{ij}}}{r_{ij}} = \int d^2\hat{\kappa}e^{-\boldsymbol{\kappa}\cdot\mathbf{r}_{im}}\cdot\alpha(L,\boldsymbol{\kappa},\mathbf{r}_{mn})\cdot e^{-\boldsymbol{\kappa}\cdot\mathbf{r}_{nj}} \tag{5.41}$$

where

$$\alpha(L,\boldsymbol{\kappa},\mathbf{r}_{mn}) = \frac{\kappa}{4\pi}\sum_{l=0}^{L}(2l+1)k_l(\kappa r_{mn})P_l(\hat{\kappa}\cdot\mathbf{r}_{mn}) \tag{5.42}$$

The equations (5.41) and (5.42) provide the plane wave expansions of the Green's function in FMA for large κ. As κ becomes extremely large, the Green's function decays and vanishes, it is not necessary to calculate the matrix elements.

5.2.5.2 Generalization of the dense FMA

The building blocks of the dense FMA at real frequencies can be found in [33, pp. 594]. The spherical waves are defined as:

$$\Psi_{lm}(k, \mathbf{r}) \equiv Y_{lm}(\theta, \phi) j_l(kr) \tag{5.43}$$

$$\Phi_{lm}(k, \mathbf{r}) \equiv Y_{lm}(\theta, \phi) h_l^{(1)}(kr) \tag{5.44}$$

The spherical waves can be represented by a summation of the spherical waves at a different location using the following equations:

$$\Phi_{lm}(k, \mathbf{r}) = \sum_{l'm'} \Phi_{l'm'}(k, \mathbf{r}') \cdot \beta_{l'm',lm}(k, \mathbf{r}''), \quad r' > r'' \tag{5.45}$$

$$\Phi_{lm}(k, \mathbf{r}) = \sum_{l'm'} \Psi_{l'm'}(k, \mathbf{r}') \cdot \alpha_{l'm',lm}(k, \mathbf{r}''), \quad r' < r'' \tag{5.46}$$

$$\Psi_{lm}(k, \mathbf{r}) = \sum_{l'm'} \Psi_{l'm'}(k, \mathbf{r}') \cdot \beta_{l'm',lm}(k, \mathbf{r}''), \quad \forall\, r', r'' \tag{5.47}$$

where $\mathbf{r}' + \mathbf{r}'' = \mathbf{r}$ and expressions for β and α are:

$$\beta_{l'm',lm}(k, \mathbf{r}'') = \sum_{l''} 4\pi i^{(l'+l''-l)} \Psi_{l'',m-m'}(k, \mathbf{r}'') \mathcal{A}_{L,L',L''} \tag{5.48}$$

$$\alpha_{l'm',lm}(k, \mathbf{r}'') = \sum_{l''} 4\pi i^{(l'+l''-l)} \Phi_{l'',m-m'}(k, \mathbf{r}'') \mathcal{A}_{L,L',L''} \tag{5.49}$$

where $\mathcal{A}_{L,L',L''}$ is the Gaunt coefficient, and it is nonzero only when $l + l' + l''$ is even. We then can proceed to generalize the wave number k to be an imaginary number.

With (5.37) and (5.38), we can re-define the spherical waves at the imaginary wave numbers in (5.43) and (5.44) as:

$$\tilde{\Psi}_{lm}(\kappa, \mathbf{r}) \equiv Y_{lm}(\theta, \phi) i_l(\kappa r) = i^{-l} \Psi_{lm}(k, \mathbf{r}) \tag{5.50}$$

$$\tilde{\Phi}_{lm}(\kappa, \mathbf{r}) \equiv (-1)^l Y_{lm}(\theta, \phi) k_l(\kappa r) = -i^{-l} \Phi_{lm}(k, \mathbf{r}) \tag{5.51}$$

Therefore, by plugging (5.50) and (5.51) into (5.45) (5.46) and (5.47), we have the spherical wave addition theorem in compact forms:

$$\tilde{\Phi}_{lm}(\kappa, \mathbf{r}) = \sum_{l'm'} \tilde{\Phi}_{l'm'}(\kappa, \mathbf{r}') \cdot \beta_{l'm',lm}(\kappa, \mathbf{r}''), \qquad r' > r'' \tag{5.52}$$

$$\tilde{\Phi}_{lm}(\kappa,\mathbf{r}) = \sum_{l'm'} \tilde{\Psi}_{l'm'}(\kappa,\mathbf{r}') \cdot \alpha_{l'm',lm}(\kappa,\mathbf{r}''), \qquad r' < r'' \tag{5.53}$$

$$\tilde{\Psi}_{lm}(\kappa,\mathbf{r}) = \sum_{l'm'} \tilde{\Psi}_{l'm'}(\kappa,\mathbf{r}') \cdot \beta_{l'm',lm}(\kappa,\mathbf{r}''), \qquad \forall\, r', r'' \tag{5.54}$$

where the translation matrix elements are re-defined as (note that they are different from the definitions of β and α at real frequencies):

$$\beta_{l'm',lm}(\kappa,\mathbf{r}'') = \sum_{l''} 4\pi(-1)^{l'+l''-l} \tilde{\Psi}_{l'',m-m'}(\kappa,\mathbf{r}'') \mathcal{A}_{L,L',L''} \tag{5.55}$$

$$\alpha_{l'm',lm}(\kappa,\mathbf{r}'') = \sum_{l''} 4\pi(-1)^{l'+l''-l} \tilde{\Phi}_{l'',m-m'}(\kappa,\mathbf{r}'') \mathcal{A}_{L,L',L''} \tag{5.56}$$

As a result, the Green's function can be written in the multipole expansion in the same way for the real frequencies, as:

$$\frac{e^{ikr_{ij}}}{r_{ij}} = \kappa \boldsymbol{\beta}(\kappa,\mathbf{r}_{im}) \cdot \overline{\boldsymbol{\alpha}}(\kappa,\mathbf{r}_{mn}) \cdot \boldsymbol{\beta}(\kappa,\mathbf{r}_{nj}) \tag{5.57}$$

By further factorizing the matrix $\overline{\boldsymbol{\alpha}}(\kappa,\mathbf{r}_{mn})$ as:

$$\overline{\boldsymbol{\alpha}}(\kappa,\mathbf{r}_{mn}) = \overline{\boldsymbol{\beta}}(\kappa,\mathbf{r}_{mp}) \cdot \overline{\boldsymbol{\alpha}}(\kappa,\mathbf{r}_{pq}) \cdot \overline{\boldsymbol{\beta}}(\kappa,\mathbf{r}_{qn}) \tag{5.58}$$

The Green's function is written in a form of multilevel FMA:

$$\frac{e^{ikr_{ij}}}{r_{ij}} = \kappa \boldsymbol{\beta}(\kappa,\mathbf{r}_{im}) \cdot \overline{\boldsymbol{\beta}}(\kappa,\mathbf{r}_{mp}) \cdot \overline{\boldsymbol{\alpha}}(\kappa,\mathbf{r}_{pq}) \cdot \overline{\boldsymbol{\beta}}(\kappa,\mathbf{r}_{qn}) \cdot \boldsymbol{\beta}(\kappa,\mathbf{r}_{nj}) \tag{5.59}$$

5.2.5.3 Hybrid FMA

Using the plane wave and multipole expansions of the Green's function, the hybrid FMA can be obtained easily by using the discussions in Chapter 4:

$$\begin{aligned} \frac{e^{-\kappa r_{ij}}}{r_{ij}} \approx & \underbrace{\kappa \int d^2\hat{\kappa} e^{-\boldsymbol{\kappa}\cdot\mathbf{r}_{im}} \cdot \alpha(l_0,\boldsymbol{\kappa},\mathbf{r}_{mn}) \cdot e^{-\boldsymbol{\kappa}\cdot\mathbf{r}_{nj}}}_{\text{plane wave expansion}} \\ & + \underbrace{\kappa \left(\boldsymbol{\beta}(\kappa,\mathbf{r}_{im}) \cdot \tilde{\overline{\boldsymbol{\alpha}}}(l_0,l_m,\kappa,\mathbf{r}_{mn}) \cdot \boldsymbol{\beta}(\kappa,\mathbf{r}_{nj}) \right)}_{\text{multipole expansion}} \end{aligned} \tag{5.60}$$

where $\alpha(L_0, \boldsymbol{\kappa}, \mathbf{r}_{mn})$ is defined as:

$$\alpha(L_0, \boldsymbol{\kappa}, \mathbf{r}_{mn}) = \frac{\kappa}{4\pi} \sum_{l=0}^{L_0} (2l+1) k_l(\kappa r_{mn}) P_l(\hat{\kappa} \cdot \mathbf{r}_{mn}) \tag{5.61}$$

The matrix elements of $\overline{\boldsymbol{\beta}}(\kappa, \mathbf{r})$ are defined in (5.55) and the matrix elements of $\overline{\boldsymbol{\alpha}}(L_0, L_m, \kappa, \mathbf{r})$ is defined similar to (5.56) as:

$$\tilde{\alpha}_{l'm',lm}(L_0, L_m, \kappa, \mathbf{r}) = \sum_{l''=L_0+1}^{L_m} 4\pi(-1)^{l'+l''-l} \tilde{\Phi}_{l'',m-m'}(\kappa, \mathbf{r}) \mathcal{A}_{L,L',L''} \tag{5.62}$$

All the discussions in Chapter 4 apply in the hybrid FMA in the imaginary frequencies. Then we can use this hybrid FMA to accelerate the matrix vector product in the calculations of the Casimir force.

5.3 Numerical Results

In this section, we validate the method in a few steps. First we investigate the Casimir force contributions at different imaginary frequencies for PEC and dielectric structures. Second, the attractive Casimir force between the PEC structures is calculated using the direct method. The simulation results are compared with the reference publication [89] for the validations. Third, the randomized SVD is integrated to compress the matrix $\frac{\partial}{\partial r}\overline{\mathbf{M}}_d$. In this step, the inverse in (5.15) is still computed using the direct method. With the randomized SVD, both the attractive and repulsive Casimir force between dielectric objects are studied in the numerical examples. Then we validate the accuracy of the hybrid FMA at imaginary frequencies in the worst case. Finally, the complete fast computing scheme, with the randomized SVD and the hybrid FMA, is used to calculate the Casimir force for problems with various sizes.

5.3.1 Casimir Force at Imaginary Frequencies

From the discussion in Section 5.2.3, the integral form of the Casimir force equation (5.24) is approximated as a finite summation:

$$F = -\frac{\hbar c}{l}\sum_i \tilde{w}_i \mathrm{tr}\left(\overline{\mathbf{M}}_d^{-1}(ck_i)\frac{\partial}{\partial \mathbf{d}}\overline{\mathbf{M}}_d(ck_i)\right) \tag{5.63}$$

where k_i is the imaginary wave number.

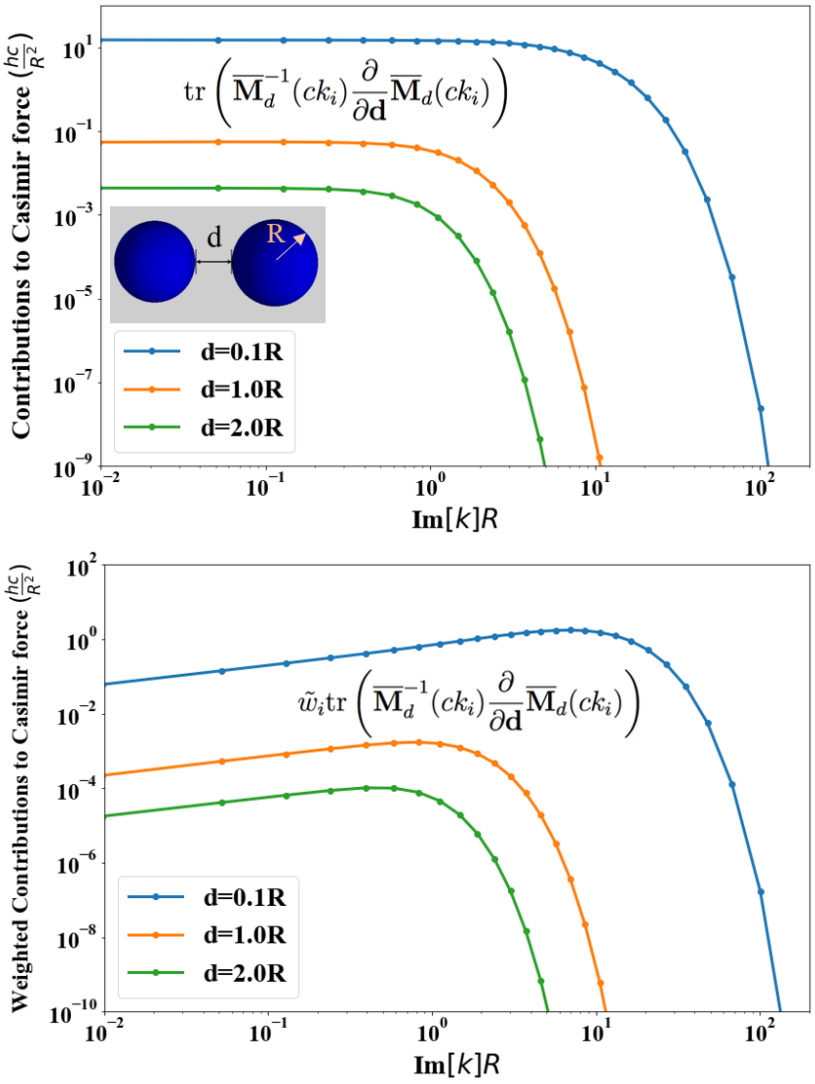

Figure 5.2: The contributions of the Casimir force at imaginary frequencies for two identical PEC spheres with radius $R = 1$ nm. Top: the trace evaluated at the imaginary wave numbers k. Bottom: the weighted contributions to the Casimir force.

The simulation results of a simple two-sphere structure are shown in Figure 5.2. The integrand in the Casimir force expression and the weighted contributions to the Casimir force at imaginary frequencies are shown. It can be seen that the contributions are mostly from the lower imaginary wave number $\Im[k]$. Also as the distance d decreases, the Casimir force increases.

A similar plot can be found in Figure 5.3 for dielectric spheres with $\epsilon(i\xi) = 2.0$. The same conclusion can be drawn that most of the contributions are from the lower imaginary wave number $\Im[k]$ for dielectrics.

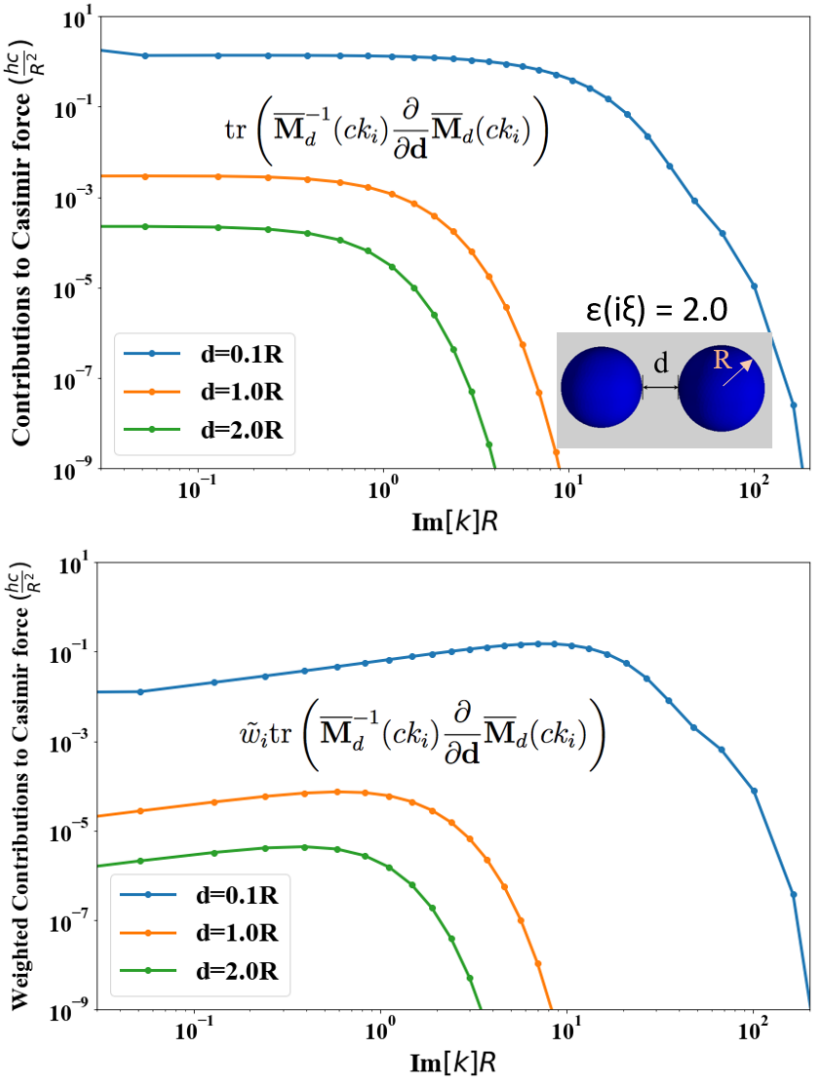

Figure 5.3: The contributions of the Casimir force at imaginary frequencies for two identical dielectric spheres ($R = 1$ nm, $\epsilon(i\xi) = 2.0$). Top: the trace evaluated at the imaginary wave numbers k. Bottom: the weighted contributions to the Casimir force.

5.3.2 Casimir Force Between PEC Objects

It is well known that the Casimir force between two PEC objects is attractive. A previous work [89, pp. 112] reported the Casimir energy between two spheres, two parallel capsules and two perpendicular capsules. We reproduce the Casimir energy calculations using our solver for the same structures for validations. Then the Casimir force equation is used, which is then compared to the finite difference results of the Casimir energy:

$$F = -\frac{d}{dr}E \tag{5.64}$$

The Casimir energy and the Casimir force are calculated for different displaced distances for these structures. The comparisons are shown in Figures 5.4-5.9.

Figures 5.4, 5.6 and 5.8 show the simulation results of the Casimir energy compared to the reference [89, p. 112]. Figures 5.5, 5.7 and 5.9 show the simulation results of the Casimir force compared to the finite difference of the data in Figures 5.4, 5.6 and 5.8. The signs of the force are chosen to be positive if the force is attractive. All the results of the Casimir energy and the force show good matches with the reference. Therefore, our numerical solver is validated for PEC structures.

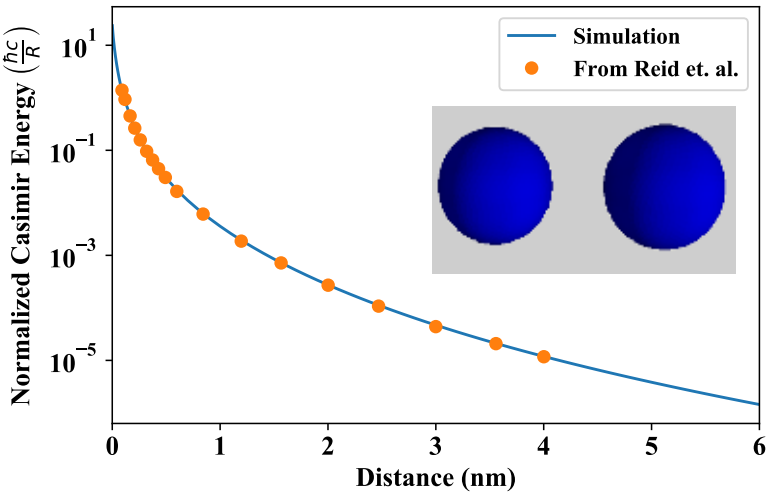

Figure 5.4: Casimir energy between two PEC spheres (radius $R = 1$ nm) compared to the reference.

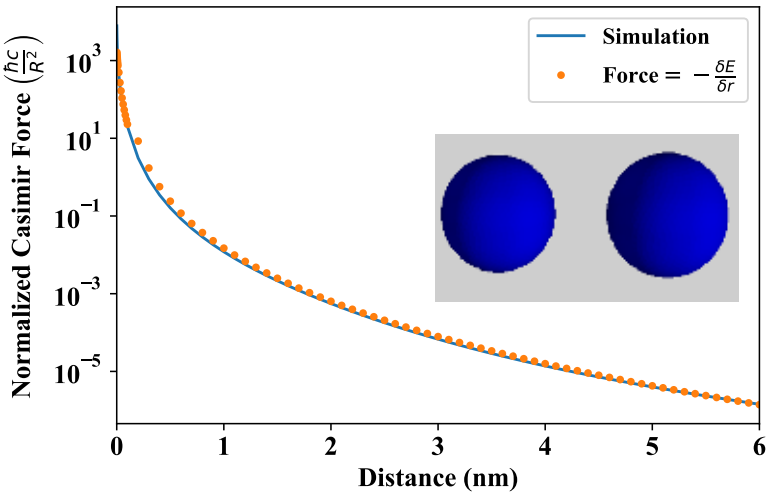

Figure 5.5: Casimir force between two PEC spheres (radius $R = 1$ nm) compared to the finite difference results.

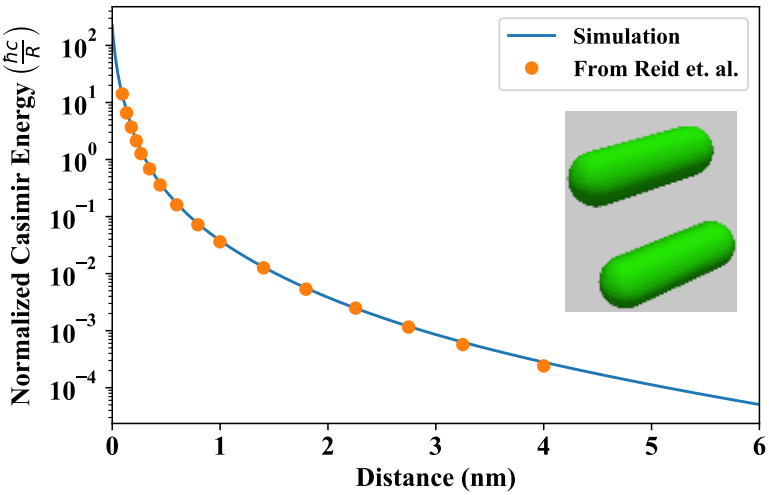

Figure 5.6: Casimir energy between two parallel PEC capsules compared to the reference.

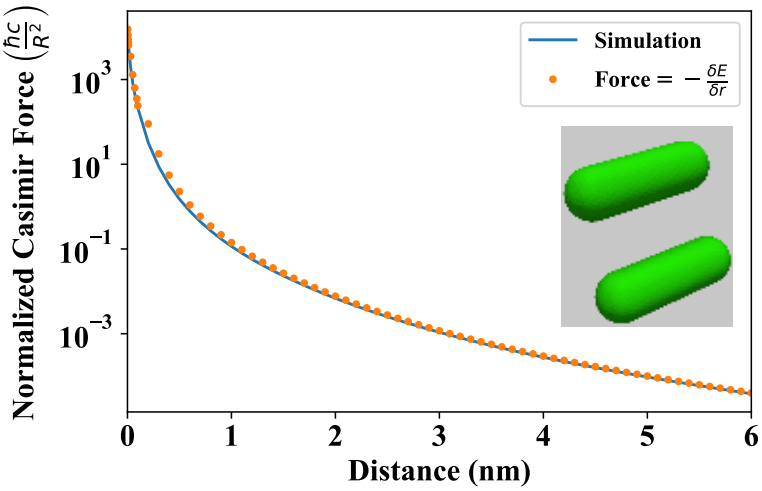

Figure 5.7: Casimir force between two parallel PEC capsules compared to the finite difference results.

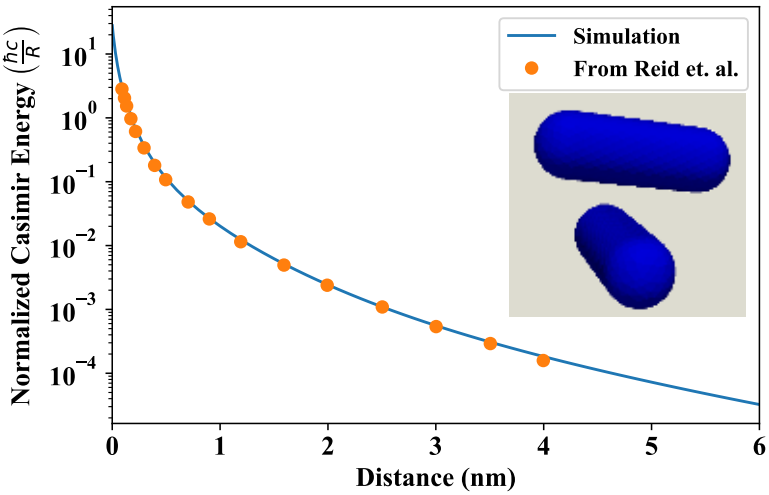

Figure 5.8: Casimir energy between two perpendicular PEC capsules compared to the reference.

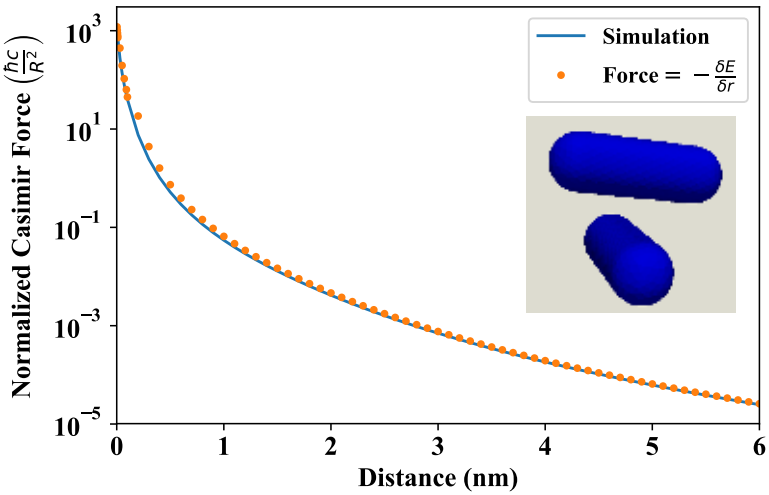

Figure 5.9: Casimir force between two perpendicular PEC capsules compared to the finite difference results.

5.3.3 Casimir Force Between Dielectric Objects and the Randomized SVD

We further present the calculation results of the Casimir force between dielectric objects and compare with the finite difference results. First, only the direct inverse method is used. Figure 5.10 shows the results of the Casimir

force of two dielectric spheres with $\epsilon_r(i\xi) = 2.0$. Our simulation results match well with the finite difference of the Casimir energy results using the direct method.

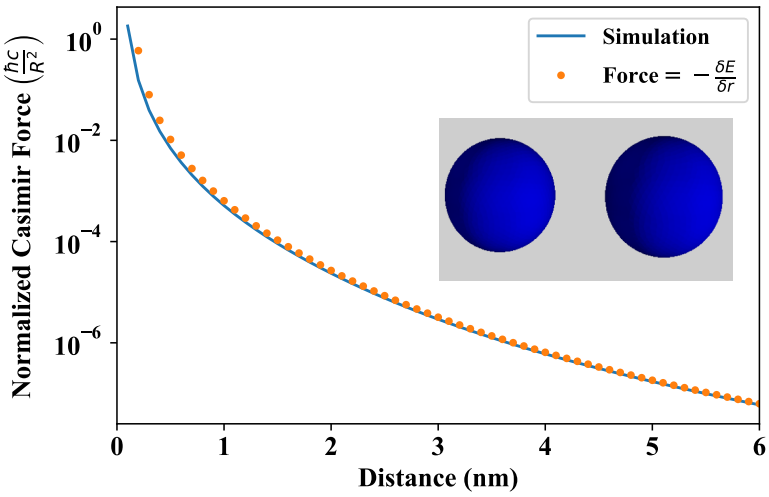

Figure 5.10: The the Casimir force compared to the finite difference of energy.

Then we apply the randomized SVD to compress the matrix $\frac{\partial}{\partial \mathbf{d}}\overline{\mathbf{M}}_d$. The example of the parallel capsules with more unknowns is simulated and the results are also compared to the finite differences of the Casimir energy. Figure 5.11 shows the calculations of attractive force between two parallel capsules using the randomized SVD. Both results show good agreements with finite differences of the Casimir energy. We further use the randomized SVD technique to investigate the attractive and repulsive force between two dielectric objects emerged in different background. Lifshitz's theory suggests that when the two objects are submerged in the fluid and the permittivity of the two objects and the fluid satisfies:

$$\epsilon_1(i\xi) < \epsilon_{\text{fluid}}(i\xi) < \epsilon_2(i\xi) \tag{5.65}$$

the force between the objects will be repulsive for large separations.

The next example validates this theory for two spheres. The relative permittivity of the two spheres at the imaginary frequencies are 1.5 and 6.5 respectively. The fluid permittivity is changed from 1 to 7. The force is

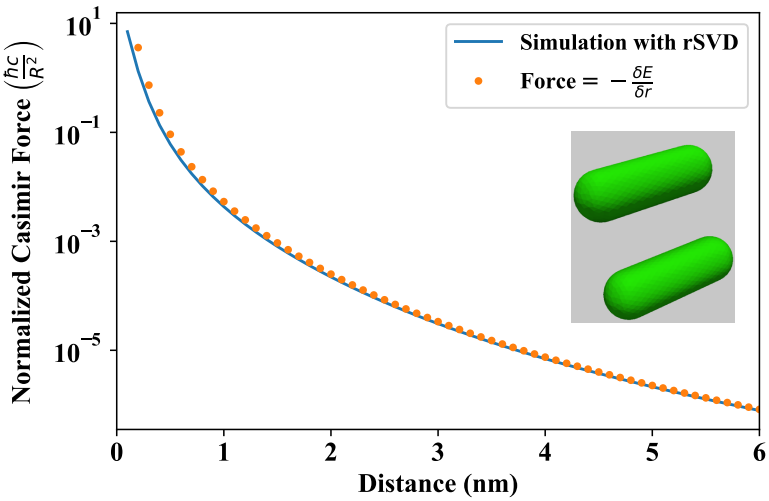

Figure 5.11: The randomized SVD calculations of the Casimir force compared to the finite difference of energy.

normalized by the PFA predictions for two spheres (see Appendix B):

$$F_{\text{PFA}} = \frac{\pi^3 \hbar c R}{720 d^3} \tag{5.66}$$

We can see from the results in Figure 5.12 that at reasonable far regime, the force is repulsive when (5.65) is satisfied.

5.3.4 Hybrid FMA at Imaginary Frequencies

The hybrid FMA can be used to accelerate the matrix vector products in the calculations. We validate the hybrid FMA at imaginary frequencies using (5.60) for the worst case of FMA, which is the same setup as in Figure 4.6. Figure 5.13 shows the worst-case errors for one buffer box with the target accuracies from 10^{-3} to $10^{-4.5}$, and Figure 5.14 shows the errors for two buffer boxes with the target accuracies from 10^{-5} to 10^{-8}. Both figures demonstrate that the error can be well bounded near the target accuracies.

With the hybrid FMA successfully adapted to the imaginary frequencies, we can then use the randomized SVD and the FMA to efficiently calculate the Casimir force.

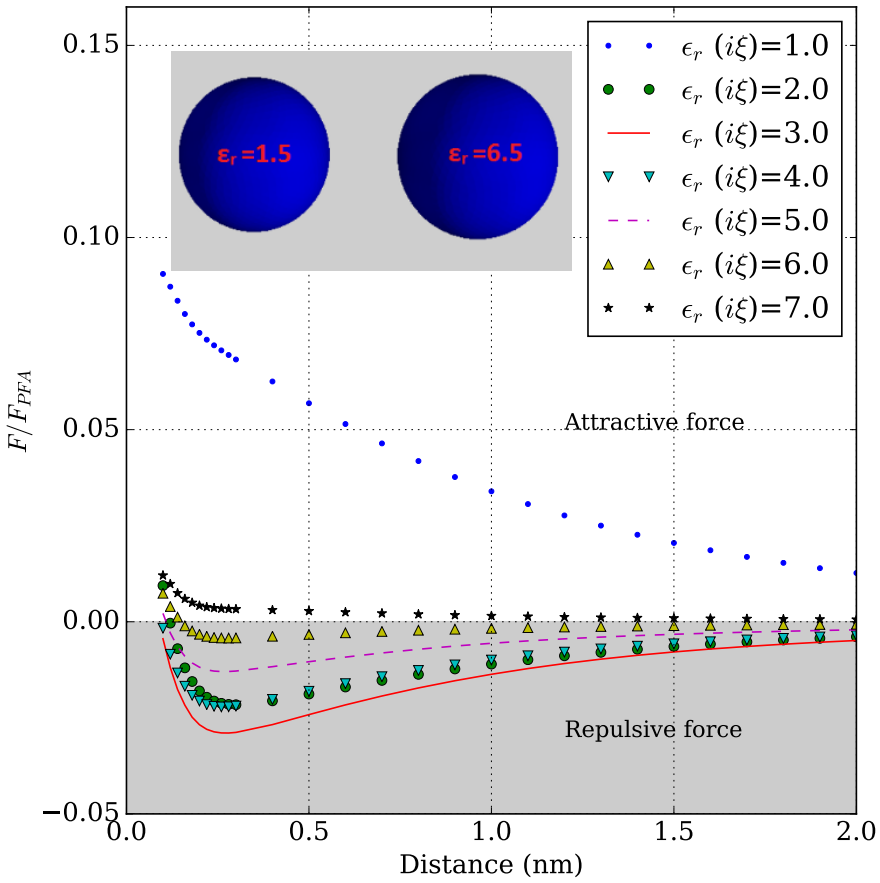

Figure 5.12: The attractive and repulsive Casimir force between two spheres for different background permittivity.

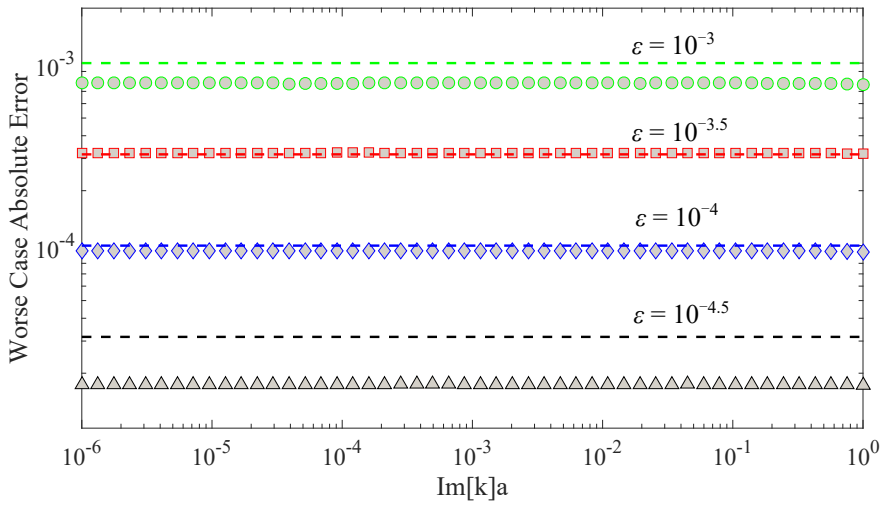

Figure 5.13: The worst-case absolute errors with one buffer box at different $\Im[k]a$, where a is the size of the box.

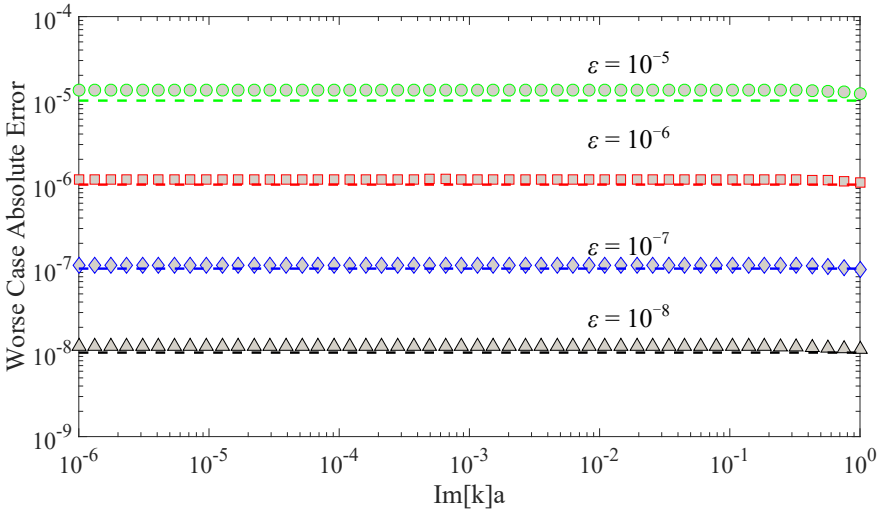

Figure 5.14: The worst-case absolute errors with two buffer boxes at different $\Im[k]a$.

5.3.5 Hybrid FMA and Randomized SVD for Large-Scale Problems

With the numerical validations of the randomized SVD (rSVD) in Section 5.3.3 and the validations of the hybrid FMA for imaginary frequencies in Section 5.3.4, we can apply the fast scheme using hybrid FMA and rSVD. Sphere pairs with different numbers of unknowns and different displaced distances are simulated and compared with the previous simulations result using the direct method as in Figures 5.2, 5.3, 5.5 and 5.10.

Table 5.1 lists the number of unknowns of the mesh sets in the simulations. When the spheres are dielectric, the numbers of unknowns are twice the numbers of unknowns in the PEC simulations. We will simulate two spheres with small distance ($d = 0.1R$), intermediate distance ($d = 1R$) and large distance ($d = 2R$), where R is the radius of the spheres and $R = 1$ nm.

Figures 5.15, 5.16 and 5.17 show the simulated traces evaluated at different imaginary frequencies of two PEC spheres with the distances $d = 2R$, $d = R$ and $d = 0.1R$ respectively. These results are compared with the direct method in the top figure of Figure 5.2. The weight contribution curves from the bottom figure of Figure 5.2 are used to represent the significance of the contributions of the data points.

Table 5.1: Numbers of unknowns in the PEC and dielectric simulations.

Mesh Set	# of Unknowns (PEC)	# of Unknowns (Dielectrics)
A	1,908	3,816
B	3612	7,224
C	25,266	50,532

The results in Figures 5.15, 5.16 and 5.17 show that as the distance between the two objects decreases, more errors are found in the simulation results using the fast scheme in the wide range of imaginary frequencies. This is as expected since the mutual interaction matrix $\frac{\partial}{\partial \mathbf{d}}\overline{\mathbf{M}}_d$ is no longer very low rank and the rSVD approximation becomes inaccurate.

From the data in Figures 5.15, 5.16, and 5.17, we can calculate the Casimir force and the errors compared to the direct method results from Figure 5.2. The Casimir force and the errors at different d for the three mesh sets are shown in Figure 5.18.

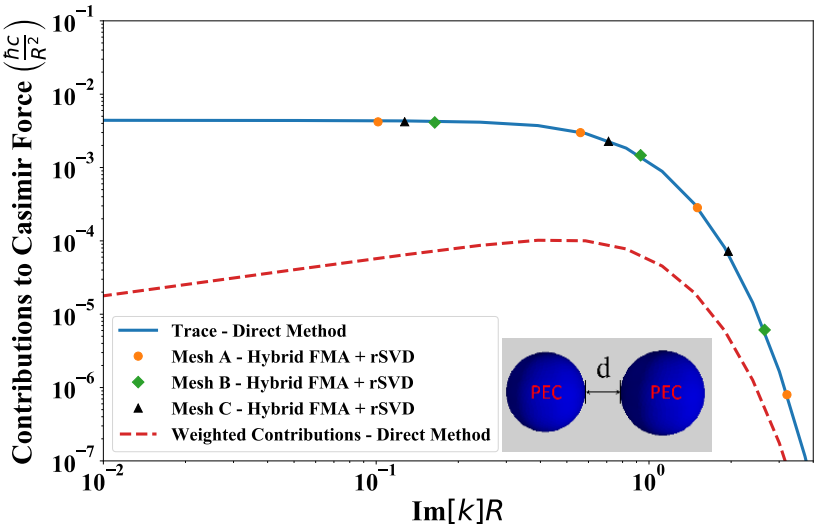

Figure 5.15: The simulation results of the three PEC sphere pairs of the mesh sets with $d = 2R$ using the hybrid FMA and rSVD.

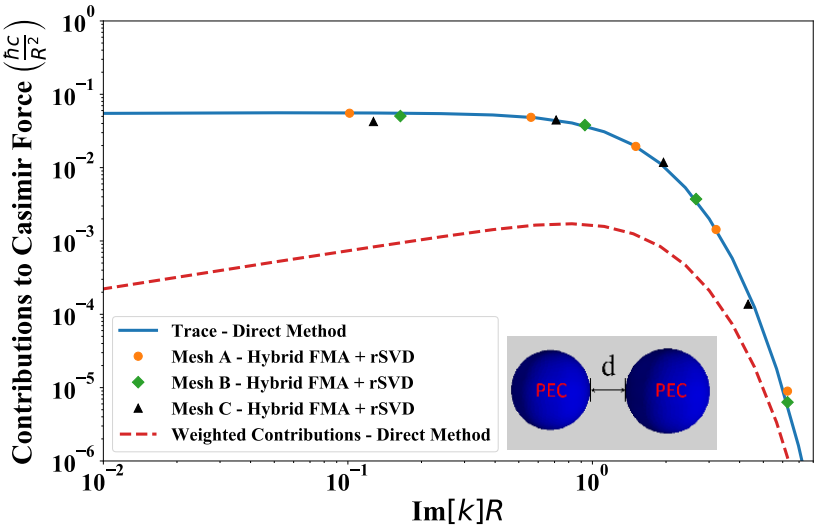

Figure 5.16: The simulation results of the three PEC sphere pairs of the mesh sets with $d = R$ using the hybrid FMA and rSVD.

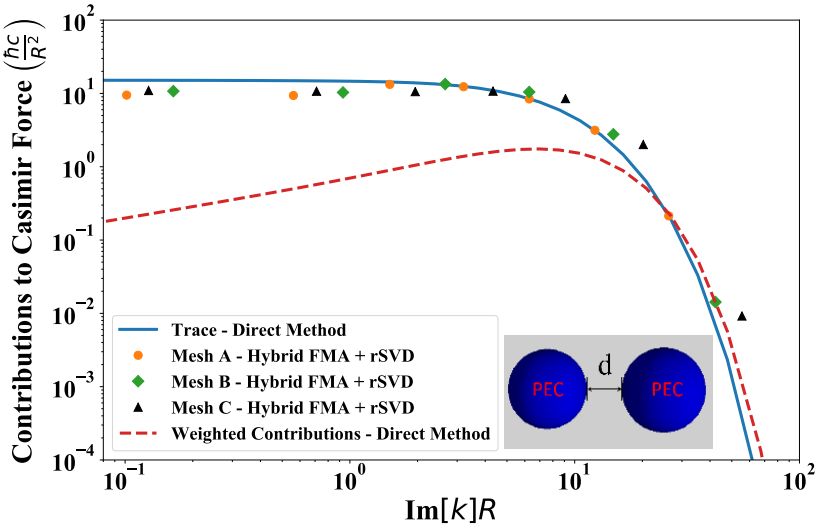

Figure 5.17: The simulation results of the three PEC sphere pairs of the mesh sets with $d = 0.1R$ using the hybrid FMA and rSVD.

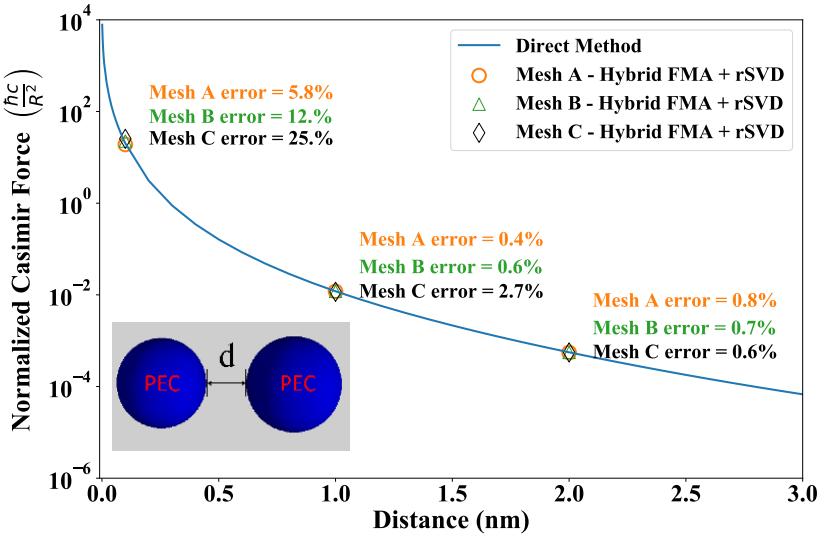

Figure 5.18: The Casimir force of the three PEC sphere pairs of the mesh sets using the hybrid FMA and rSVD.

The three mesh sets and the three choices of the distance d are used for the simulations of the dielectric sphere pair. The permittivity of the spheres $\epsilon_r = 2$. Similarly, the results at the imaginary frequencies are shown in Figures 5.19, 5.20 and 5.21 and are compared to the results using the direct method. The Casimir force between the two spheres at $d = 2R$, $d = R$ and $d = 0.1R$ are shown in Figure 5.22. We can also see that, for two closed objects the simulation errors increase.

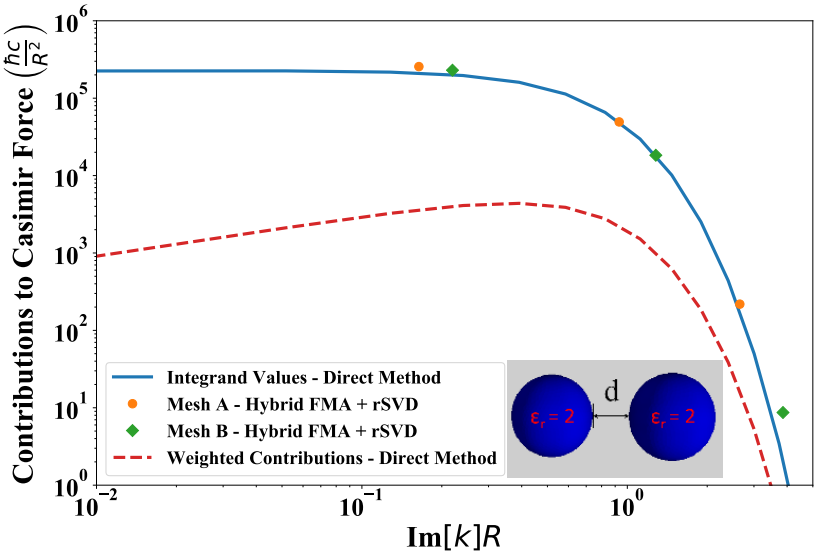

Figure 5.19: The simulation results of the three dielectric ($\epsilon_r = 2$) sphere pairs of the mesh sets with $d = 2R$ using the hybrid FMA and rSVD.

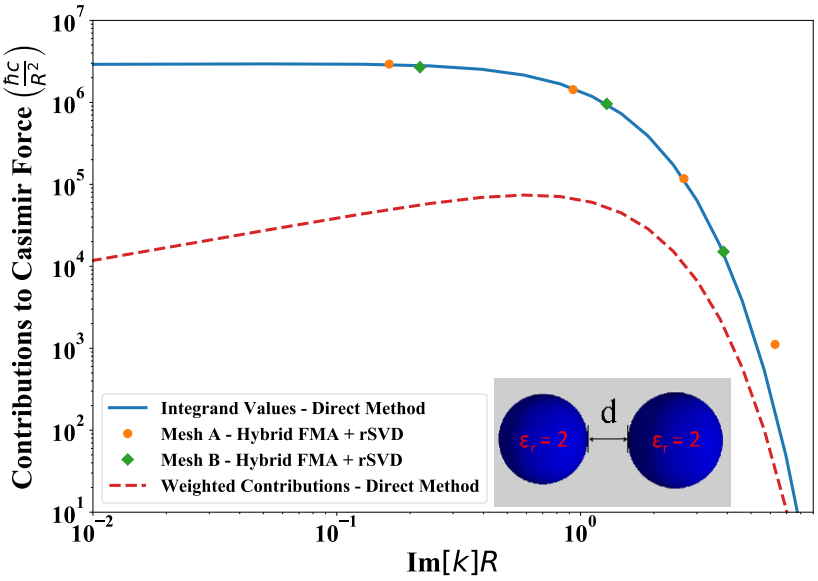

Figure 5.20: The simulation results of the three dielectric ($\epsilon_r = 2$) sphere pairs of the mesh sets with $d = R$ using the hybrid FMA and rSVD.

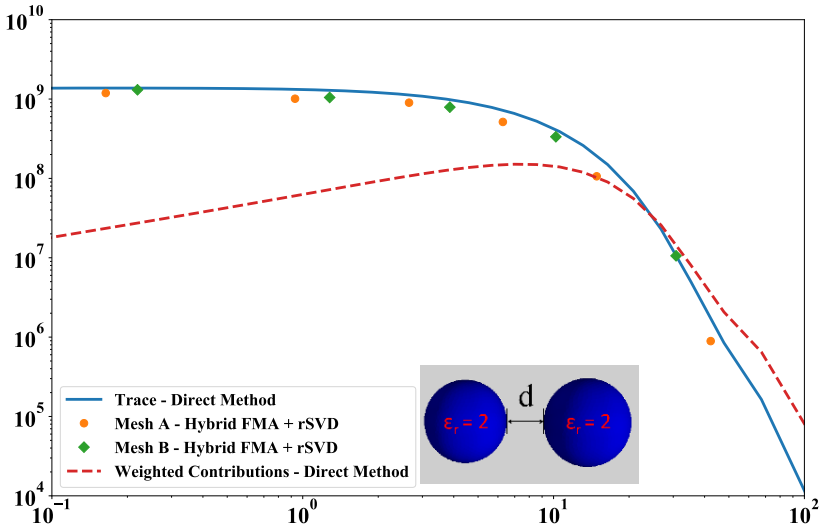

Figure 5.21: The simulation results of the three dielectric ($\epsilon_r = 2$) sphere pairs of the mesh sets with $d = 0.1R$ using the hybrid FMA and rSVD.

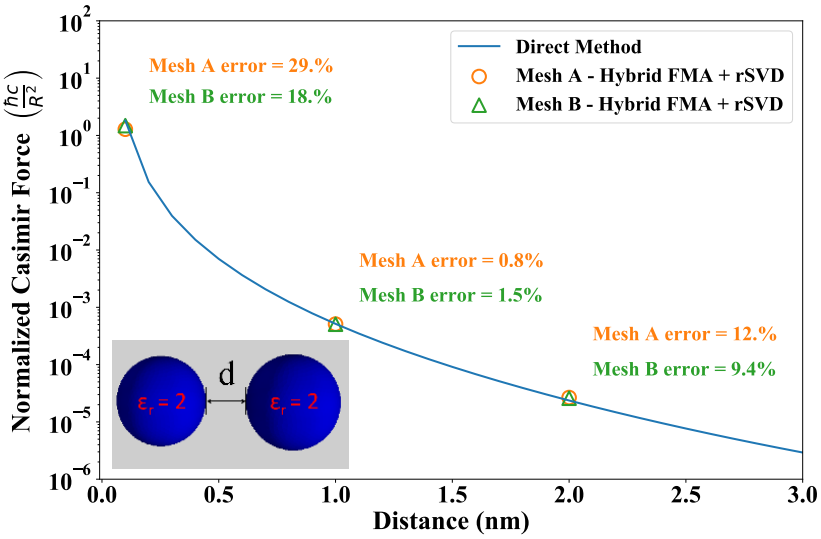

Figure 5.22: The Casimir force of the three dielectric ($\epsilon_r = 2$) sphere pairs of the mesh sets using the hybrid FMA and rSVD.

5.4 Numerical Issues

There exist some numerical issues that can be improved in the future for the proposed fast scheme.

First, the method becomes less accurate when the two objects are close to each other. This is due to the inaccurate low-rank approximation of the matrix using the rSVD. It can be improved by increasing the number of the singular values in rSVD. Therefore, it further requires more efficient implementation of the solver.

Second, the EFIE for PEC, and PMCHWT for dielectrics become ill-conditioned at low imaginary frequencies, for example $\Im[k]R < 0.01$ (this is very similar to the low-frequency breakdown at the real frequencies). This gives rise to large iteration numbers to solve (5.32) using the iterative solver. As a result, the computational time is increased or even inaccurate results are produced due to failures of convergences. An introduction of the low-frequency stable formulations can be useful to reduce to computational cost and improved the accuracy.

Third, the computational time is not significantly reduced using the proposed method. This is because of the large number of the matrix vector product needed in order to solve (5.32) in the procedure 2, especially for

small $\Im[k]R$. A parallel implementation of the FMA can be particularly useful.

5.5 Conclusions

In this chapter, we review some background of the Casimir force. The expression of the Casimir force between two objects is re-derived using the argument principle and it can be expressed in terms of matrices in the surface integral equation for homogeneous bodies. A fast computing scheme is proposed and validated to calculate the Casimir force for large-scale problems. The numerical issues are briefly discussed for future improvements of the proposed method.

Chapter 6

Conclusions

In this dissertation, we successfully establish an enhanced augmented electric field integral equation for dielectrics. Then this method is extended to the simulations of conductors. Some real-world structures are simulated to demonstrate the capabilities of the method. Then we further study the fast algorithm in the integral equation. We propose a broadband multilevel fast multipole algorithm using a hybridization of the multipole and plane wave expansions. High accuracy can be achieved using this method the error and can be well controlled. Finally we apply the hybrid fast mulitpole algorithm and the randomized singular value decomposition in the surface integral equation to calculate the Casimir force.

A fast computing scheme is proposed for large-scale computing of the Casimir force. The computational time can be further improved by using mixed integral equation formulations at low and high frequencies, parallelling the FMA at imaginary frequencies or applying the direct inverse method. This can be the future work to further accelerate the solver of the Casimir force calculations.

Appendix A

Derivations of the Integrals Using the Modified Integral Method

The integrals of interest are:

$$I_1 = \int_{S'} d\mathbf{r}' \frac{e^{ikR}}{R} \tag{A.1}$$

$$\mathbf{I}_\beta = \int_{S'} d\mathbf{r}' \frac{e^{ikR}}{R} \boldsymbol{\rho}(\mathbf{r}') \tag{A.2}$$

$$\mathbf{I}_\perp = \mathbf{d} \int_{S'} d\mathbf{r}' \frac{ikR - 1}{R^3} e^{ikR} \tag{A.3}$$

$$\mathbf{I}_\parallel = \int_{S'} d\mathbf{r}' \frac{ikR - 1}{R^3} e^{ikR} \boldsymbol{\rho}(\mathbf{r}') \tag{A.4}$$

In order to evaluate these integrals over a triangle, we can project the observation point onto the source triangle. Then the surface integral can be written as a summation of three surface integrals on the sub-triangles, as in Figure A.1. Then each integral can be converted into cylindrical coordinates by:

$$\int_{S'} d\mathbf{r}' = \sum_{i=1, h_i \neq 0}^{3} \int_{S'_i} d\mathbf{r}' = \sum_{i=1, h_i \neq 0}^{3} \int_{\theta_i^-}^{\theta_i^+} d\theta \int_0^{\rho_i(\theta)} \rho d\rho \tag{A.5}$$

where $\rho_i(\theta) = \frac{h_i}{\cos\theta}$. For (A.1) and (A.3), using

$$\rho d\rho = R dR \tag{A.6}$$

the expressions in (A.1) and (A.3) can be simplified as:

$$I_1 = \sum_{i=1, h_i \neq 0}^{3} \int_{\theta_i^-}^{\theta_i^+} d\theta \frac{1}{ik} \left(e^{ikR(\theta)} - e^{ikd} \right) \tag{A.7}$$

$$\mathbf{I}_\perp = \hat{d} \sum_{i=1, h_i \neq 0}^{3} \int_{\theta_i^-}^{\theta_i^+} d\theta \left(\frac{d}{R(\theta)} e^{ikR(\theta)} - e^{ikd} \right) \tag{A.8}$$

where $R(\theta) = \sqrt{d^2 + h_i^2/\cos^2\theta}$. The above method is the same as in [50] except that the singularities are removed.

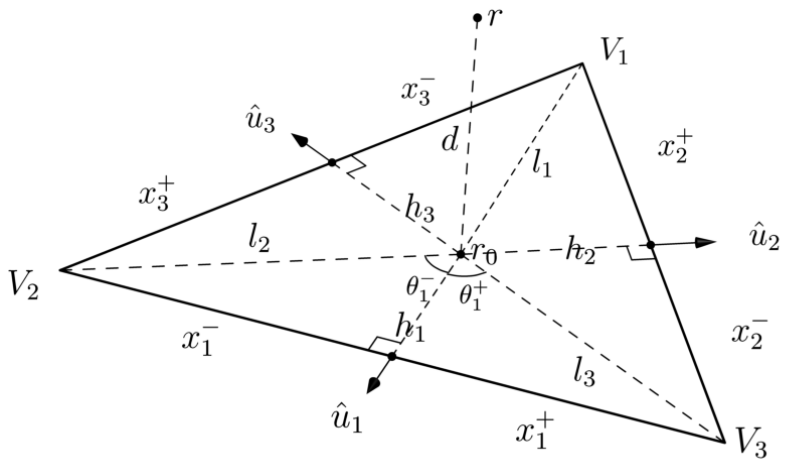

Figure A.1: Dividing the surface integral into three sub-triangle integrals.

For (A.2) and (A.4), using (A.5) will not simplify the integrals because the inner integrals over ρ do not have analytical forms. One can use the derivations in [50] to derive an equation of $\hat{u}_i$. But when r_0 is on the triangle edges, $\hat{u}_i$ is undefined. Alternatively, we propose another way to evaluate (A.2) and (A.4) to avoid this issue using an equation similar to (A.5):

$$\int_{S'} d\mathbf{r}' = \sum_{i=1,h_i\neq 0}^{3} \int_{S_i'} d\mathbf{r}' = \sum_{i=1,h_i\neq 0}^{3} \int_{l_i^-}^{l_i^+} \rho d\rho \int_{\alpha(\theta)}^{\beta(\theta)} d\theta \tag{A.9}$$

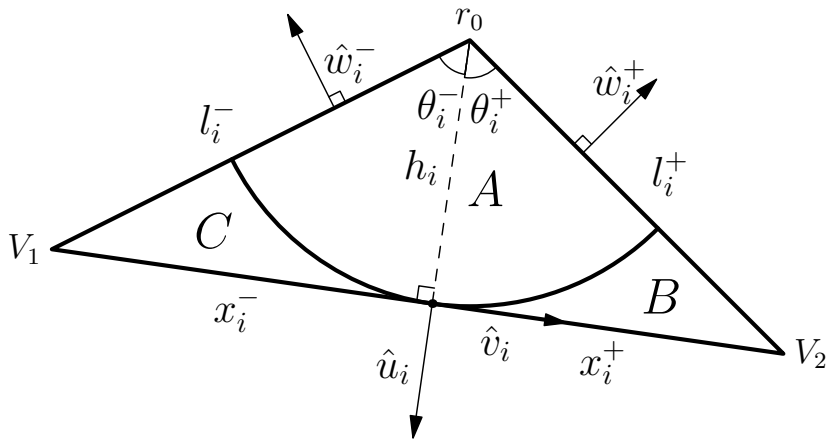

Figure A.2: Dividing one sub-triangle into A, B, C parts. Part A is enclosed by the boundary of the sub-triangle and the arc. Parts B, C are the remaining two regions.

To do this, we need to further divide each sub-triangle into three parts: A, B and C, as in Figure A.2. In general, for an arbitrary function $f(R)$,

$$\begin{aligned}&\int_A d\mathbf{r}' f(R)\boldsymbol{\rho}(\mathbf{r}')\\&= \int_0^{h_i} \rho^2 d\rho f(\rho) \begin{pmatrix} \sin\theta_i^+ - \sin\theta_i^- \\ \cos\theta_i^- - \cos\theta_i^+ \end{pmatrix}_i\end{aligned} \tag{A.10}$$

$$\begin{aligned}&\int_B d\mathbf{r}' f(R)\boldsymbol{\rho}(\mathbf{r}')\\&= \int_{h_i}^{l_i^+} \rho d\rho f(\rho) \begin{pmatrix} \rho\sin\theta_i^+ - s_i^+\sqrt{\rho^2 - h_i^2} \\ h_i - \rho\cos\theta_i^+ \end{pmatrix}_i\end{aligned} \tag{A.11}$$

$$\begin{aligned}&\int_C d\mathbf{r}' f(R)\boldsymbol{\rho}(\mathbf{r}')\\&= \int_{h_i}^{l_i^-} \rho d\rho f(\rho) \begin{pmatrix} s_i^-\sqrt{\rho^2 - h_i^2} - \rho\sin\theta_i^- \\ \rho\cos\theta_i^- - h_i \end{pmatrix}_i\end{aligned} \tag{A.12}$$

where

$$\begin{pmatrix} a \\ b \end{pmatrix}_i = a\hat{u}_i + b\hat{v}_i \tag{A.13}$$

and

$$s_i^\pm = \frac{\theta_i^\pm}{|\theta_i^\pm|} \tag{A.14}$$

Summing over the integrals in A, B and C, we have:

$$\begin{aligned}
&\int_{S'} d\mathbf{r}' f(R)\boldsymbol{\rho}(\mathbf{r}') = \\
&\sum_{i=1,h_i\neq 0}^{3} \begin{pmatrix} \sin\theta_i^+ \\ -\cos\theta_i^+ \end{pmatrix}_i \int_0^{l_i^+} \rho^2 d\rho f(\rho) + \\
&\sum_{i=1,h_i\neq 0}^{3} \begin{pmatrix} -\sin\theta_i^- \\ \cos\theta_i^- \end{pmatrix}_i \int_0^{l_i^-} \rho^2 d\rho f(\rho) + \\
&\sum_{i=1,h_i\neq 0}^{3} \begin{pmatrix} \left(-s_i^+ \int_h^{l_i^+} + s_i^- \int_h^{l_i^-}\right) \rho d\rho f(R)\sqrt{\rho^2 - h_i^2} \\ h_i \left(\int_{h_i}^{l_i^+} - \int_{h_i}^{l_i^-}\right) \rho d\rho f(R) \end{pmatrix}_i
\end{aligned} \tag{A.15}$$

It turns out that the first and the second terms on the right-hand side of (A.15) cancel out. The first term is a vector pointing in the $-\hat{w}_i^+$ direction, as in Figure A.2, with the amplitude given by the integral. The second term points to $-\hat{w}_i^-$ and the amplitude is given by the integral from 0 to l_i^-. Noticing that each l_i^- is also l_j^+ for the other sub-triangle, then the two terms cancel out when summing up the contributions from the three triangles. For the last term, the component in $\hat{u}_i$ requires numerical integration. The component in the $\hat{v}_i$ can be integrated analytically using (A.6). In (A.2), $f(R) = \frac{e^{ikR}}{R}$,

$$\int \rho d\rho f(R) = \frac{1}{ik} e^{ikR} \tag{A.16}$$

By letting $R_i^{\pm} = \sqrt{d^2 + (l_i^{\pm})^2}$,

$$\mathbf{I}_\beta = \sum_{i=1,h_i\neq 0}^{3} \begin{pmatrix} -\int_{x_i^-}^{x_i^+} \frac{x^2}{R(x)} e^{ikR(x)} dx \\ \frac{h_i}{ik}\left(e^{ikR_i^+} - e^{ikR_i^-}\right) \end{pmatrix} \tag{A.17}$$

In (A.4), $f(R) = \frac{e^{ikR}}{R^3}(ikR - 1)$,

$$\int \rho d\rho f(R) = \frac{e^{ikR}}{R} \tag{A.18}$$

$$\mathbf{I}_\parallel = \sum_{i=1,h_i\neq 0}^{3} \begin{pmatrix} -\int_{x_i^-}^{x_i^+} \frac{x^2}{R^3(x)} (ikR(x) - 1) e^{ikR(x)} dx \\ h_i \left(\frac{e^{ikR_i^+}}{R_i^+} - \frac{e^{ikR_i^-}}{R_i^-}\right) \end{pmatrix} \tag{A.19}$$

Appendix B

Proximity Force Approximation of Casimir Energy and Force for Simple Structures

The proximity force approximation (PFA) can be used to calculate the Casimir energy and force between two objects closed to each other. This approximation is based on the equations of the Casimir energy and force between two parallel plates from Casimir's 1948 famous paper [17]. The energy per unit area is:

$$E(a) = -\frac{\pi^2 \hbar c}{720 a^3} \tag{B.1}$$

and the force per unit area:

$$F(a) = \frac{\pi^2 \hbar c}{240 a^4} \tag{B.2}$$

where a is the distance between the two plates.

B.1 Two Identical Spheres

For a two-sphere setup, if the two spheres are very close to each other, i.e. $H \ll R$, where H is the distance between the two spheres and R is the radius of the spheres, the energy and the force can be calculated by integrating the above equations in (B.1) and (B.2).

By substituting $a = H + R(1 - \cos\theta)$ in the polar coordinate:

$$\begin{aligned} E_{\text{spheres}}(H) &= -\frac{\pi^2 \hbar c}{720} \int_S dS \frac{1}{a^3} \\ &= -\frac{\pi^2 \hbar c}{720} 2R^2 \int_0^{\pi/2} d\theta \frac{\sin\theta}{(H + 2R(1 - \cos\theta))^3} \end{aligned} \tag{B.3}$$

Letting $b = \frac{H}{R}$, and assuming $b \to 0$, we have:

$$\begin{aligned} E_{\text{spheres}}(H) &= \frac{\pi^2 \hbar c}{360R} \int_1^0 dx \frac{1}{(b+2-2x)^3} \\ &= \frac{\pi^2 \hbar c}{360R} \left(\frac{1}{4(b+2)^2} - \frac{1}{4b^2} \right) \approx -\frac{\pi^2 \hbar c}{1440 R b^2} \end{aligned} \tag{B.4}$$

Therefore the Casimir energy is:

$$E_{\text{spheres}}(H) = -\frac{\pi^2 \hbar c R}{1440 H^2} \tag{B.5}$$

Taking the derivative of the energy with respect to H, the Casimir force is:

$$F_{\text{spheres}}(H) = -\frac{\pi^2 \hbar c R}{720 H^3} \tag{B.6}$$

B.2 A Sphere and a Plate

If one of the sphere is replaced by the plate, the derivation is similar, by only removing a factor of 2 in the expression of a:

$$\begin{aligned} E_{\text{sphere-slab}}(H) &= -\frac{\pi^2 \hbar c}{720} \int_S dS \frac{1}{a^3} \\ &= -\frac{\pi^2 \hbar c}{720} 2R^2 \int_0^{\pi/2} d\theta \frac{\sin\theta}{(H + R(1-\cos\theta))^3} \end{aligned} \tag{B.7}$$

Therefore:

$$E_{\text{sphere-slab}}(H) = -\frac{\pi^2 \hbar c R}{720 H^2} \tag{B.8}$$

The Casimir force is then

$$F_{\text{sphere-slab}}(H) = -\frac{\pi^2 \hbar c R}{360 H^3} \tag{B.9}$$

References

[1] K. Yee, "Numerical solution of initial boundary value problems involving Maxwell's equations in isotropic media," *IEEE Trans. Antennas Propag.*, vol. 14, pp. 302–307, May 1966.

[2] J. Jin, *The Finite Element Method in Electromagnetics*. New York, NY: Wiley-IEEE Press, 2002.

[3] W. C. Chew, M. S. Tong, and B. Hu, *Integral Equation Methods for Electromagnetic and Elastic Waves*. New York, NY: Morgan and Claypool, 2007.

[4] S. M. Rao, D. R. Wilton, and A. W. Glisson, "Electromagnetic scattering by surfaces of arbitrary shape," *IEEE Trans. Antennas Propag.*, vol. 30, no. 3, pp. 409–418, 1982.

[5] Q. L. Chen and D. R. Wilton, "Electromagnetic scattering by three-dimensional arbitrary complex material/conducting bodies," in *Proc. IEEE Antennas Propag. Soc. Int. Symp.*, Dallas, TX, 1982, pp. 590–593.

[6] A. Buffa and S. Christiansen, "A dual finite element complex on the barycentric refinement," *Math. Comput.*, vol. 76, no. 9, pp. 2995–3004, 2007.

[7] D. R. Wilton and A. W. Glisson, "On improving the electric field integral equation at low frequencies," in *Proc. URSI Radio Sci. Meet. Dig.*, Los Angeles, CA, June 1981, p. 24.

[8] J. R. Mautz and R. F. Harrington, "An E-field solution for a conducting surface small or comparable to the wavelength," *IEEE Trans. Antennas Propag.*, vol. 32, pp. 330–339, Apr. 1984.

[9] X. Q. Sheng, J. M. Jin, J. M. Song, W. C. Chew, and C. C. Lu, "Solution of combined-field integral equation using multilevel fast multipole algorithm for scattering by homogeneous bodies," *IEEE Trans. Antennas Propag.*, vol. 46, pp. 1718–1726, Nov. 1998.

[10] T. K. Wu and L. L. Tsai, "Scattering from arbitrarily-shaped lossy dielectric bodies of revolution," *Radio Sci.*, vol. 12, pp. 709–718, 1977.

[11] Y. Chang and R. F. Harrington, "A surface formulation for characteristic modes of material bodies," *IEEE Trans. Antennas Propag.*, vol. 25, pp. 789–795, 1977.

[12] C. Müller, *Foundations of the Mathematical Theory of Electromagnetic Waves*. Berlin, Germany: Springer, 1969.

[13] J. S. Zhao and W. C. Chew, "Three-dimensional multilevel fast multipole algorithm from static to electrodynamic," *Microw. Opt. Technol. Lett.*, vol. 26, no. 1, pp. 43–48, July 2000.

[14] Z. G. Qian and W. C. Chew, "Fast full-wave surface integral equation solver for multiscale structure modeling," *IEEE Trans. Antennas Propag.*, vol. 50, pp. 3594–3601, Nov. 2009.

[15] S. K. Lamoreaux, "Demonstration of the Casimir force in the 0.7 to 6 μm range," *Phys. Rev. Lett.*, vol. 78, no. 1, pp. 5–8, Jan. 1997.

[16] R. S. Decca, D. López, E. Fischbach, G. L. Klimchitskaya, D. E. Krause, and V. M. Mostepanenko, "Tests of new physics from precise measurements of the Casimir pressure between two gold-coated plates," *Phys. Rev. D - Part. Fields, Gravit. Cosmol.*, vol. 75, no. 7, p. 077101, Apr. 2007.

[17] H. Casimir, "On the attraction between two perfectly conducting plates," *Proc. K. Ned. Akad.*, vol. 360, no. April, pp. 793–795, 1948.

[18] S. J. Rahi, T. Emig, N. Graham, R. L. Jaffe, and M. Kardar, "Scattering theory approach to electrodynamic Casimir forces," *Phys. Rev. D - Part. Fields, Gravit. Cosmol.*, vol. 80, no. 8, p. 085021, Oct. 2009.

[19] N. Van Kampen, B. Nijboer, and K. Schram, "On the macroscopic theory of Van der Waals forces," *Phys. Lett. A*, vol. 26, no. 7, pp. 307–308, Feb. 1968.

[20] M. T. H. Reid, J. White, and S. G. Johnson, "Fluctuating surface currents: An algorithm for efficient prediction of Casimir interactions among arbitrary materials in arbitrary geometries," *Phys. Rev. A - At. Mol. Opt. Phys.*, vol. 88, no. 2, p. 022514, Aug. 2013.

[21] E. M. Lifshitz, "The theory of molecular attractive forces between solids," *Sov. Phys.*, vol. 2, no. 1, pp. 73–83, 1956.

[22] H. Nyquist, "Thermal agitation of electric charge in conductors," *Phys. Rev.*, vol. 32, no. 1, pp. 110–113, July 1928.

[23] J. Weber, "Fluctuation dissipation theorem," *Phys. Rev.*, vol. 101, no. 6, pp. 1620–1626, Mar. 1956.

[24] J. S. Zhao and W. C. Chew, "Integral equation solution of Maxwell's equations from zero frequency to microwave frequencies," *IEEE Trans. Antennas Propag.*, vol. 48, no. 10, pp. 1635–1645, 2000.

[25] S. H. Lee and J. M. Jin, "Application of the tree-cotree splitting for improving matrix conditioning in the full-wave finite-element analysis of high-speed circuits," *Microw. Opt. Technol. Lett.*, vol. 50, no. 6, pp. 1476–1481, 2008.

[26] Z. G. Qian, "Augmented surface integral equation method for low-frequency electromagnetic analysis," Ph.D. dissertation, University of Illinois at Urbana-Champaign, 2009.

[27] Y. Zhang, T. Cui, W. C. Chew, and J. S. Zhao, "Magnetic field integral equation at very low frequencies," *IEEE Trans. Antennas Propag.*, vol. 51, p. 1864–1871, Aug. 2003.

[28] Z. G. Qian and W. C. Chew, "Enhanced A-EFIE with perturbation method," *IEEE Trans. Antennas Propag.*, vol. 58, no. 10, pp. 3256–3264, Oct. 2010.

[29] M. Taskinen and P. Ylä-Oijala, "Current and charge integral equation formulation," *IEEE Trans. Antennas Propag.*, vol. 54, pp. 58–67, Jan. 2006.

[30] M. S. Tong, W. C. Chew, B. J. Rubin, J. D. Morsey, and L. Jiang, "On the dual basis for solving electromagnetic surface integral equations," *IEEE Trans. Antennas Propag.*, vol. 57, no. 10, pp. 3136–3146, Oct. 2009.

[31] F. P. Andriulli, K. Cools, F. Olyslager, A. Buffa, S. Christiansen, and E. Michielssen, "A multiplicative Calderon preconditioner for the electric field integral equation," *IEEE Trans. Antennas Propag.*, vol. 56, no. 8, pp. 2398–2412, Aug. 2008.

[32] L. J. Jiang and W. C. Chew, "A mixed-form fast multipole algorithm," *IEEE Trans. Antennas Propag.*, vol. 53, no. 12, pp. 4145–4156, Dec. 2005.

[33] W. C. Chew, *Waves and Fields in Inhomogenous Media*. New York: Wiley-IEEE Press, 1995.

[34] G. C. Hsiao and R. E. Kleinman, "Mathematical foundations for error estimation in numerical solutions of integral equations in electromagnetics," *IEEE Trans. Antennas Propag.*, vol. 45, no. 3, pp. 316–328, 1997.

[35] S. Yan, J. M. Jin, and Z. Nie, "Improving the accuracy of the second-kind Fredholm integral equations by using the Buffa-Christiansen functions," *IEEE Trans. Antennas Propag.*, vol. 59, pp. 1299–1310, Apr. 2011.

[36] M. Benzi, G. H. Golub, and J. Liesen, "Numerical solution of saddle point problems," *Acta Numerica*, vol. 14, pp. 1–137, 2005.

[37] Z. G. Qian and W. C. Chew, "An augmented electric field integral equation for high-speed interconnect analysis," *Micro. Opt. Technol. Lett.*, vol. 50, no. 10, pp. 2658–2662, Oct. 2008.

[38] Y. Saad and M. Schultz, "GMRES: A generalized minimal residual algorithm for solving nonsymmetric linear systems," *SIAM J. on Scientific and Statistical Comp.*, vol. 7, pp. 856–869, 1986.

[39] H. A. V. der Vorst, "Bi-CGSTAB: A fast and smoothly converging variant of Bi-CG for the solution of nonsymmetric linear systems," *SIAM J. on Scientific and Statistical Comp.*, vol. 13, pp. 631–644, 1992.

[40] J. Guan, S. Yan, and J. M. Jin, "An accurate and efficient finite element-boundary integral method with GPU acceleration for 3-D electromagnetic analysis," *IEEE Trans. Antennas Propag.*, vol. 62, pp. 6325–6336, Dec. 2014.

[41] S. Chakraborty and V. Jandhyala, "Evaluation of Green's function integrals in conducting media," *IEEE Trans. Antennas Propag.*, vol. 52, no. 12, pp. 3357–3363, 2004.

[42] L. Tsang, J. A. Kong, and K. H. Ding, *Scattering of Electromagnetic Waves: Theories and Applications*. Wiley-Interscience, 2000.

[43] M. A. Leontovich, *Investigations of Propagation of Radiowaves, Part II*. Moscow, 1948.

[44] T. B. A. Senior, "Impedance boundary conditions for imperfectly conducting surfaces," *Appl. Sci. Res*, vol. 8, pp. 418–436, 1960.

[45] L. N. Medgyesi-Mitschang and J. M. Putnam, "Integral equation formulations for imperfectly conducting scatterers," *IEEE Trans. Antennas Propag.*, vol. 33, pp. 206–214, Feb. 1985.

[46] P. Ylä-Oijala, S. P. Kiminki, and S. Javenpää, "Solving IBC-CFIE with dual basis functions," *IEEE Trans. Antennas Propag.*, vol. 58, no. 12, pp. 3997–4004, 2010.

[47] S. Yan and J. M. Jin, "Self-dual integral equations for electromagnetic scattering from IBC objects," *IEEE Trans. Antennas Propag.*, vol. 61, pp. 206–214, Nov. 2013.

[48] S. Yan, J. M. Jin, and Z. Nie, "Calderon preconditioner: From EFIE and MFIE to N-Müller equations," *IEEE Trans. Antennas Propag.*, vol. 58, pp. 4105–4110, Dec. 2010.

[49] K. M. Coperich, A. E. Ruehli, and A. Cangellaris, "Enhanced skin effect for partial-element equivalent circuit (PEEC) models," vol. 48, no. 9, pp. 1435–1442, 2000.

[50] Z. G. Qian, W. C. Chew, and R. Suaya, "Generalized impedance boundary condition for conductor modeling in surface integral equation," *IEEE Trans. Antennas Propag.*, vol. 55, no. 11, pp. 2354–2364, 2007.

[51] M. B. Stephanson and J. F. Lee, "Preconditioned electric field integral equation using Calderon identities and dual loop/star basis functions," *IEEE Trans. Antennas Propag.*, vol. 57, pp. 1274–1279, Apr. 2009.

[52] T. Xia, H. Gan, M. Wei, W. C. Chew, H. Braunisch, Z. Qian, K. Aygün, and A. Aydiner, "An enhanced augmented electric field integral equation formulation for dielectric objects," *IEEE Trans. Antennas Propag.*, vol. 64, pp. 2339–2347, June 2016.

[53] T. Xia, H. Gan, M. Wei, W. C. Chew, H. Braunisch, Z. Qian, K. Aygün, and A. Aydiner, "An augmented electric field integral equation formulation for dielectrics and conductors at low frequencies," in *IEEE Symp. on Electromagnetic Compatibility Signal Integrity (EMCSI)*, Santa Clara, CA, Mar. 2015, pp. 209–214.

[54] R. D. Graglia, "On the numerical integration of the linear shape functions times the 3-D Green's function or its gradient on a plane triangle," *IEEE Trans. Antennas Propag.*, vol. 41, no. 10, pp. 1448–1455, 1993.

[55] P. Ylä-Oijala and M. Taskinen, "Calculation of CFIE impedance matrix elements with RWG and $n\times$RWG functions," *IEEE Trans. Antennas Propag.*, vol. 51, no. 8, pp. 1837–1846, 2003.

[56] S. Q. He, W. E. I. Sha, L. J. Jiang, W. C. H. Choy, W. C. Chew, and Z. P. Nie, "Finite-element-based generalized impedance boundary condition for modeling plasmonic nanostructures," *IEEE Trans. Nanotech.*, vol. 11, pp. 336–345, 2012.

[57] W. C. Chew, J. M. Jin, E. Michielssen, and J. M. Song, *Fast and Efficient Algorithms in Computational Electromagnetics*. Boston: Artech House, 2001.

[58] N. Engheta, W. D. Murphy, V. Rokhlin, and M. S. Vassiliou, "The fast multipole method (FMM) for electromagnetic scattering problems," *IEEE Trans. Antennas Propag.*, vol. 40, no. 6, pp. 634–641, June 1992.

[59] J. M. Song, C. C. Lu, and W. C. Chew, "Multilevel fast multipole algorithm for electromagnetic scattering by large complex objects," *IEEE Trans. Antennas Propag.*, vol. 45, no. 10, pp. 1488–1493, Oct. 1997.

[60] J. Guan, S. Yan, and J. M. Jin, "An OpenMP-CUDA implementation of multilevel fast multipole algorithm for electromagnetic simulation on multi-GPU computing systems," *IEEE Trans. Antennas Propag.*, vol. 61, no. 7, pp. 3607–3616, July 2013.

[61] B. Karaosmanoğlu, A. Yılmaz, U. M. Gür, and Ö. Ergül, "Solutions of plasmonic structures using the multilevel fast multipole algorithm," *Int. J. RF Microw. Comput. Eng.*, vol. 26, no. 4, pp. 335–341, May 2016.

[62] V. Rokhlin, "Rapid solution of integral equations of classical potential theory," *J. Comput. Phys.*, vol. 60, no. 2, pp. 187–207, Sep. 1985.

[63] L. F. Greengard, "The rapid evaluation of potential fields in particle systems," Ph.D. dissertation, 1987.

[64] V. Rokhlin, "Diagonal forms of translation operators for the Helmholtz equation in three dimensions," *Appl. Comput. Harmon. Anal.*, vol. 1, no. 1, pp. 82–93, Dec. 1993.

[65] L. Hamilton, P. Macdonald, M. Stalzer, R. Turley, J. Visher, and S. Wandzura, "3D method of moments scattering computations using the fast multipole method," in *Proc. IEEE Antennas Propag. Soc. Int. Symp. URSI Natl. Radio Sci. Meet.*, vol. 1. IEEE, 1994, pp. 435–438.

[66] J. M. Song and W. C. Chew, "Fast multipole method solution using parametric geometry," *Microw. Opt. Technol. Lett.*, vol. 7, no. 16, pp. 760–765, 1994.

[67] B. Dembart and E. Yip, "A 3D fast multipole method for electromagnetics with multiple levels," *11th Ann. Rev. Prog. Appl. Comput. Electromag.*, vol. 1, pp. 621–628, 1995.

[68] J. M. Song and W. C. Chew, "Multilevel fast-multipole algorithm for solving combined field integral equations of electromagnetic scattering," *Microw. Opt. Technol. Lett.*, vol. 10, no. 1, pp. 14–19, Sep. 1995.

[69] W. C. Chew, S. Koc, J. M. Song, C. C. Lu, and E. Michielssen, "A succinct way to diagonalize the translation matrix in three dimensions," *Microw. Opt. Technol. Lett.*, vol. 15, no. 3, pp. 144–147, June 1997.

[70] J. Song and W. C. Chew, "Interpolation of translation matrix in MLFMA," *Microw. Opt. Technol. Lett.*, vol. 30, no. 2, pp. 109–114, July 2001.

[71] J. Sarvas, "Performing interpolation and anterpolation entirely by fast Fourier transform in the 3-D multilevel fast multipole algorithm," *SIAM J. Numer. Anal.*, vol. 41, no. 6, pp. 2180–2196, 2003.

[72] E. Darve and P. Have, "A fast multipole method for Maxwell equations stable at all frequencies," *Philos. Trans. R. Soc. A Math. Phys. Eng. Sci.*, vol. 362, no. 1816, pp. 603–628, 2004.

[73] B. Hu, W. C. Chew, and S. Velamparambil, "Fast inhomogeneous plane wave algorithm for the analysis of electromagnetic scattering," *Radio Sci.*, vol. 36, no. 6, pp. 1327–1340, Nov. 2001.

[74] E. Darve, "Efficient fast multipole method for low frequency scattering," *Cent. Turbul. Res. Annu. Res. Briefs*, 2001.

[75] L. J. Jiang and W. C. Chew, "Low-frequency fast inhomogeneous plane-wave algorithm (LF-FIPWA)," *Microw. Opt. Technol. Lett.*, vol. 40, no. 2, pp. 117–122, 2004.

[76] M. Vikram, H. Huang, B. Shanker, and T. Van, "A novel wideband FMM for fast integral equation solution of multiscale problems in electromagnetics," *IEEE Trans. Antennas Propag.*, vol. 57, no. 7, pp. 2094–2104, July 2009.

[77] M. Takrimi, O. Ergul, and V. B. Erturk, "A novel broadband multi-level fast multipole algorithm with incomplete-leaf tree structures for multiscale electromagnetic problems," *IEEE Trans. Antennas Propag.*, vol. 64, no. 6, pp. 2445–2456, 2016.

[78] T. Xia, H. Gan, M. Wei, W. C. Chew, H. Braunisch, Z. Qian, K. Aygun, and A. Aydiner, "An integral equation modeling of lossy conductors with the enhanced augmented electric field integral equation," *IEEE Trans. Antennas Propag.*, vol. 65, no. 8, pp. 4181–4190, Aug. 2017.

[79] L. L. Meng, X. Y. Z. Xiong, T. Xia, and L. J. Jiang, "The error control of mixed-form fast multipole algorithm based on the high-order multipole rotation," *IEEE Antennas Wirel. Propag. Lett.*, vol. 16, pp. 1655–1658, 2017.

[80] H. Cheng, W. Y. Crutchfield, Z. Gimbutas, L. F. Greengard, J. F. Ethridge, J. Huang, V. Rokhlin, N. Yarvin, and J. Zhao, "A wideband fast multipole method for the Helmholtz equation in three dimensions," *J. Comput. Phys.*, vol. 216, no. 1, pp. 300–325, July 2006.

[81] I. Bogaert, J. Peeters, and F. Olyslager, "A nondirective plane wave MLFMA stable at low frequencies," *IEEE Trans. Antennas Propag.*, vol. 56, no. 12, pp. 3752–3767, Dec. 2008.

[82] O. Ergul and B. Karaosmanoglu, "Broadband multilevel fast multipole algorithm based on an approximate diagonalization of the Green's function," *IEEE Trans. Antennas Propag.*, vol. 63, no. 7, pp. 3035–3041, July 2015.

[83] H. B. G. Casimir and D. Polder, "The influence of retardation on the London-van der Waals forces," *Phys. Rev.*, vol. 73, no. 4, pp. 360–372, Feb. 1948.

[84] F. London, "The general theory of molecular forces," *Trans. Faraday Soc.*, vol. 33, no. 1, p. 8, Jan. 1937.

[85] P. W. Milonni and C. Eberlein, "The quantum vacuum: An introduction to quantum electrodynamics," *Am. J. Phys.*, vol. 62, no. 12, p. 1154, Dec. 1994.

[86] S. K. Lamoreaux, "The Casimir force: Background, experiments, and applications," *Reports Prog. Phys.*, vol. 68, no. 1, pp. 201–236, Jan. 2005.

[87] P. R. Atkins, "A study on computational electromagnetics problems with applications to Casimir force calculations," Ph.D. dissertation, University of Illinois at Urbana-Champaign, 2013.

[88] N. Halko, P. G. Martinsson, and J. A. Tropp, "Finding structure with randomness: Probabilistic algorithms for constructing approximate matrix decompositions," *SIAM Rev.*, vol. 53, no. 2, pp. 217–288, Sep. 2009.

[89] H. Reid, "Fluctuating surface currents: A new algorithm for efficient prediction of Casimir interactions among arbitrary materials in arbitrary geometries," Ph.D. dissertation, Massachusetts Institute of Technology, 2011.